Core Annular Flow Theory as Applied to the Adiabatic Section of Heat Pipe

by

Aishwarya Rath

A thesis submitted in partial fulfillment of the requirements for the degree of

Master of Science

Department of Mechanical Engineering

University of Alberta

Abstract

The core annular flow (CAF) theory is used to model the parallel flow of fluids of different phases. CAF theory has been applied to a lot of industrial applications from bitumen hydro transport to sub-aqueous drag reduction. Here we consider the extension of core annular flow theory to the study of the adiabatic section of heat pipes as heat pipes deal with the two-phase flow of fluids in parallel, flowing in opposite direction. We aim to develop a first-principles estimate of the conditions necessary to maximize the (counter) flow of liquid and vapor and, which by extension, maximizes the axial flow of heat. This work investigates a model of the heat pipe in both planar geometry and cylindrical geometry. Moreover, both the geometries considered the heat pipes either containing or devoid of a wick. In these two respective cases, the peripheral return flow of liquid is driven by capillarity and by gravity. Our model can predict velocity profiles and the appropriate pressure gradient ratio (vapor-to-liquid). We further obtain estimates for the optimum thickness of the liquid layer which is required to obtain the maximum mass flow rate. In the case of wick based heat pipe when the liquid flow occurs via capillary pumping, there is a minimum surface tension below which the wick cannot supply a sufficient flow of liquid. We have characterized this critical point in terms of e.g. the viscosity ratio, the density ratio, and the wick depth, porosity, and permeability. We have compared the pressure gradient ratio (vapor-to-liquid) obtained from our model to experimental data from Shafahi et al. (2010). One inconsistency that our model contains is that the interface is assumed to be flat insofar as using the shear-stress boundary condition but curved insofar as supporting the capillary pressure required by the heat pipe to drive the flow of liquid. We have explored this discrepancy addressed in chapter 2 by using the perturbation theory in chapter 3. Chapter 3 considers two-phase flow in a porous medium extending infinitely and

curved meniscus at the liquid-vapor interface. Using such a model we have preserved the essential features required to study the effect of a curved interface. Chapter 3 shows the effect of using a deflected interface in the porous medium on the velocity profiles. Finally, we characterize the magnitude of the effect of using a curved interface for liquid vapor parallel flow in the porous medium when compared against the model considering a flat interface.

Keywords: Core-annular flow, Capillary pumping, Perturbation theory

Preface

The theoretical analysis presented in this thesis is conducted by me with the help of Prof Morris R. Flynn. Chapter 1 presents the introduction. Chapter 2 is published as an article in a journal: "Core annular flow theory as applied to the adiabatic section of heat pipes", Physics of Fluids 32, 083607 (2020), Aishwarya Rath and M. R. Flynn. M. R. Flynn was the supervisory author and helped with the identification, concept and reviewing of the problem. The performance of the various parts of the research and solving the problem in the journal article was done by me. Part of chapter 2 was also presented in the 72nd Annual Meeting of the American Physical Society-Division of Fluid Dynamics (APS Physics) conference, on November 23-26, 2019 held in Seattle, WA. The work presented in chapter 3 is my original work. Chapter 4 presents the summary and conclusion.

Dedicated to my father Late. Mahant kumar Rath and mother Pushpanjali Rath.

Acknowledgements

I would like to express my appreciation to Prof Morris R. Flynn for his valuable and constructive suggestions during the planning and development of this research work. His willingness to give his time so generously has been very much appreciated.

This study was carried out by the financial support generously provided by Engineered Air by NSERC through its CRD program.

I would like to thank my sister Shikha Rath, my brother Janmejay Rath, and Saurabh Dixit for his immense support and motivation during my masters, extending my gratitude to two very special people Dr. J P. Das and Gita Das for being a crucial part of my life during my master thesis and always motivating me whenever I was in stress and low mood. I would also like to express my gratitude to my colleague Muhammad Rizwanur Rahman for providing an informative environment in our office where most of the thinking has been carried out. Last but not least I would like to thank my friends Alireza Gharahi and Soumya Sahoo for their support.

Table of Contents

List of Tables

List of Figures

Chapter 1

Introduction

Core annular flows are internal flows where a core of viscous liquid is surrounded by a sheathing layer of lower viscosity, be it liquid or gas, e.g. air (Ooms et al. 2007). Ooms et al. (2007) used theoretical methods to show that if there is a significant pressure difference over a horizontal pipe, then there is a balance between the buoyancy force and hydrodynamics force on the core. The balance of these forces makes the core annular flow possible (Ooms et al. 2007). The same study showed that when there is a decrease in the pressure difference and an increase of buoyancy, the eccentricity of the core increases. In core annular flow, when the viscous liquid does not make direct contact with the boundaries of the confining geometry (e.g. the inner surface of a pipeline), drag is reduced.

Advances in core annular flow theory have encouraged many in the scientific and engineering communities to develop numerous technologies for industrial and engineering applications. For example, core annular flow theory is used in lubricated flows as the pumping pressures are balanced by wall shear stresses in the water on the periphery.

Water-lubricated technology helps in the transportation of heavy viscous oils. Oil companies have been using water as a lubricant for the transportation of oil since 1904 (Isaacs & Speed 1904 in US Patent No. 759374). Lubricated flows are effective if the oil to be transported has high viscosity, and this is the reason why pipeline companies used the emulsification of oil to increase its viscosity (Dos et al. 2007, Joseph et al. 1995, Joseph et al. 1997, Gruncell et al. 2013) but emulsification also led to higher energy requirement for the pumping operation. Core annular flow theory is also used in the transportation of bitumen froth. The bitumen is extracted from mined oilsands. A hot water extraction process is used to separate bitumen as froth from sand, and the extracted bitumen froth self-lubricates in a pipe flow. A detailed study was done by Syncrude Canada Ltd. (Sanders et al. 2004) on the lubricated transport of bitumen froth.

In a similar study, Busse et al. (2013) presents an investigation considering two immiscible fluids for a variety of steady, laminar internal flows (i.e. Couette flow, symmetric channel flow, pressure-driven channel flow and pipe flow). In this work, the fluid with lower dynamic viscosity

forms an infinite layer of constant thickness, and acts as a lubricant for the second liquid flowing over the first liquid. If the air layer is too thin, then it plays a modest role in reducing the overall shear stress. Busse et al. (2013) considered the first fluid to be gas and considered two different assumptions. In the Couette flow cases, a constant shear rate developed in the gas layer. In the pressure-driven cases, it was assumed that the pressure gradient in gas and liquid was equal. As a consequence, in Couette flow and pressure-driven cases, the net mass flow rate of gas was more than zero which, begs the question of how a constant mass flow rate in gas is maintained. The second assumption was that the mass flow rate in the gas layer is zero. However, in both cases, Busse et al. (2013) considered an optimal superhydrophobic surface to achieve a trapped air layer.

The investigation by Busse et al. (2013) compares the zero mass flow rate in the gas layer with the conventional assumptions of equal pressure gradients in gas and liquid. They derived analytic solutions to the velocity profiles for all the cases. With the results in hand, it was found that in the Couette flow cases, the presence of a gas layer reduces the shear rate, and thus the velocity of the liquid layer is much higher. Whereas, the mass flow rate of the gas layer is zero, then the shear rate in the liquid reduces for high viscosity contrasts of liquid and air and increases for lower viscosity contrasts. In addition, counter-current flow develops in the part of the gas layer that is closer to the wall. In the pressure-driven cases, it was found that the velocity profile of the gas layer takes the same form as it would if the whole channel or pipe were filled with gas. Busse et al. (2013) also focused on presenting upper limits to drag reduction, bearing in mind that the main reason to discuss the flow of liquid over gas is to reduce drag.

Busse et al. (2013) showed that in the Couette flow cases, even with a thin layer of gas in the zero-mass flow rate case, the drag reduction is less compared to the case of constant shear rate. In the pressure-driven cases for constant gas, layer thickness leads to the blockage of the cross-sectional area of the pipe or channel which results in drag-increasing effects. However, in pressure-driven cases with even a thick gas layer leading to blockage of the cross-sectional area of the pipe, a high drag reduction can be achieved with a high viscosity contrast between liquid and gas. There is a limit of the gas layer thickness after which the drag keeps increasing. The gas layer thickness limit is higher in the channel flow with equal pressure gradients than the other flow cases considered by Busse et al. (2013), as the lubrication effects of the gas are substantial. Since, there is an upper limit to gas layer thickness, there is also a lower limit to how thin a gas layer can be. In the Couette flow and pressure driven case, the drag reduction under a zero-mass flow rate in the gas layer is higher than the case in which an equal pressure gradient in liquid and gas is maintained. The two effects of the gas layers are that the gas layer provides lubrication for the liquid layer in some cases and leads to blockage in other cases. Therefore, Busse et al. (2013) also studied the optimum gas layer thickness required for achieving a higher mass flow rate.

Busse et al. (2013) also investigated the slip length of a laminar flow of a liquid over an air

layer (i.e. two immiscible liquids) where the air layer has a zero mass flow rate downstream (i.e. stationary). They found that if the profile of the velocity can be measured theoretically, the slip length at the wall can also be computed. Two approaches were considered. The first one considered the bottom of the roughness and the second considered the top of the roughness, which is the liquid−gas interface. The second approach gave misleading results, and there were two concerns regarding this approach: first, that the presence of surface roughness would give a positive slip length as there was a positive mean stream-wise velocity near the top of the roughness, and second, that the coating of superhydrophobic surfaces has the drawback of decreasing the cross-sectional area of the channel. Therefore, to find and compare the apparent slip length, the wall must be smooth, and the bottom of the gas layer must be the wall.

The assumptions made by Busse et al. (2013) showed that, in the channel flow, the air layer is either immobile or flows downstream along with the liquid. The gas layer flows because a constant shear is applied along its upper surface. The latter assumption is the more reasonable one, but from a practical point of view, it remains to address of how the air layer was held in place, as the authors considered a "perfect" hydrophobic surface when micro-roughness is not required. They also pointed out that the gas layer flows with the liquid but never discussed replenishing the gas layer.

Drag reduction is no less important in the context of external (vs. internal) flow. In considering such a scenario and the possibility of a liquid flowing over an air-encapsulated solid object (e.g. a sphere), the mechanism for drag reduction is the same as before, i.e. the momentum transfer across the air-water interface, which generates an internal circulation of air within the plastron (McHale et al. 2011). McHale et al. (2011) demonstrated an optimum air layer that reduces the drag on a compound object. They showed that if the air layer becomes too thin, then there is no momentum transfer at the air-water interface generating internal circulation in the plastron and the drag increases as it would if the solid object was in direct contact with water, whereas, if the air layer is too thick the drag is depressed by a greater proportion. There is a need to retain this air layer for drag reduction, and this can be achieved with the help of high surface roughness of the wall. Such surfaces are known as "superhydrophobic surfaces", and are structures which have a certain roughness and the potential to retain the air layer at the surface.

The air trapped within the microstructures of superhydrophobic surfaces is seen in many insects that can breathe underwater. The thin layer of air trapped in the microstructure which is in contact with the surrounding fluid corresponds to a three-phase configuration also known as "Cassie-Baxter state". When the object is submerged in water, the air can be displaced by the pressure fluctuations of the water, low dissolved gas concentrations, and shear stress. Therefore, it is essential to recover this air layer when the object is submerged in water (McHale et al. 2011).

There have been numerous studies exploring how the plastron layer can be replenished, which

we have divided into three categories. The first approach is to generate the gas/vapor in the original location by some chemical treatment. These chemical treatments include photoelectric water splitting, and film boiling and also by electrolysis Lee & Kim(2011) have demonstrated the recovery of plastron using electrolysis on Pt/Au-coated silicon pillars. The second approach is to supply gas/air continuously to the plastron. The continuous supply of air is done when the plastron is connected to an air reservoir or by injecting gas bubbles into the boundary layer of the flow. The third approach is to saturate the water with the dissolved gas, which achieves plastron recovery by diffusion through the liquid and mass transfer through the interface. Panchanathan et al. (2018) discussed a method of catalytic decomposition of hydrogen peroxide to replenish the air layer. Hydrogen peroxide decomposes into water and oxygen at room temperature, and the authors used textured surfaces to test plastron recovery. Another study about retaining the gas layer underwater was carried out by Forsberg et al. (2011). Water in contact with the rough surface is in two states: one where the surface is completely wet, and another where the surface is partially wet. Forsberg et al. (2011) investigated the effect of water pressure on the gas layer trapped by the superhydrophobic surfaces, because the gas layer gets washed away if the water pressure is too high. They used theoretical means and assumed a linear dependence between the volume of air and the water pressure to calculate the pressure required to collapse or wash the air entirely from the solid surface; they also performed an experiment to support their theory. Similarly, Ling et al. (2016) studied the mean velocity profiles of the boundary layers of the superhydrophobic surfaces.

The work presented in the current manuscript builds on the findings of Busse et al. (2013) in which we explore a case characterized by an equal and opposite counterflow of vapor and liquid. This counterflow is the first major difference with the Busse et al. (2013) study, made possible, respectively, by evaporation and condensation which occur at the opposite ends of a control volume. To this end, we will explore ideas from core annular flow theory, the flows that arise within the adiabatic section of heat pipes.

1.0.1 Heat pipes

heat pipes are passive devices that are used to transmit heat over several centimetres or metres depending upon the electronic equipment such as heat recovery in buildings, aerospace equipment, laptops, mobile etcetera. Of the different known heat transfer devices, heat pipes are the most effective *passive* device. One of the greatest advantages of using a heat pipe is that it can transport heat over a considerable distance through a small cross-sectional area without any external power supply. Furthermore, the design and manufacture of heat pipes is quite simple.

History of heat pipes

Perkin′s tube, invented in 1836, was the predecessor of heat pipes. The design was quite close to the heat pipe we use today, i.e. a closed tube containing a small quantity of water operating as a two-phase cycle. The heat pipe was introduced in 1944 by Gaugler, from the General Motor Corporation in the US (patent No. 2350348). The idea proposed by Gaugler was that liquid evaporates generating vapor, the vapor travels below the point of evaporation and that is the condenser. The condensate is returned to the evaporator by capillary pressure provided by the use of a sintered iron wick. In 1964, Grover started working on heat pipes in the Los Alamos National Laboratory in New Mexico. Two years later, Grover filed a patent on behalf of the US Atomic Energy Commission and established that heat pipes can be regarded as synergistic engineering structures having a thermal conductivity higher than any known material.

In 1965, Cotter published theoretical results and design tools recognizing heat pipes as a thermal device. heat pipes were used in space applications as they can operate in microgravitational fields. heat pipes and thermosyphons have also been used in energy saving applications, and therefore the industrial community is actively involved in their research, development, and commercialization (Dobran et al. 1989, Huang et al. 2017, Nguyen et al. 2000).

Heat pipe operations

A heat pipe can be of any size and shape but can be best understood by considering a cylindrical geometry. The main components of a heat pipe are the container, the wick structure and a small amount of working fluid. The working fluid could be water, acetone, methanol, ammonia, or sodium, and the heat pipe works on the operating temperature of the working fluid. Heat is applied externally to the evaporator section of the pipe where the vaporization of the fluid takes place; where the heat is conducted through the pipe wall and the wick structure. The vapor pressure that develops causes the vapor to flow to the condenser section where it condenses, releasing the latent heat of vaporization. Due to the presence of the wick, capillary pressure is created which pumps the liquid back to the evaporator section. The circulation of fluid between the condenser and the evaporator continues as long as there is capillary pressure inside the heat pipe.

The generation of capillary pressure inside a heat pipe takes place due to the wick structure. The menisci formed at the liquid-vapor interface are highly curved in the evaporator section and flat in the condenser section. The surface tension of the fluid and the curved structure of the interface gives rise to capillary pressure.

Types of heat pipes

There are different types of heat pipes. A given heat pipe can have multiple condensers, evaporators, and adiabatic sections. Gravitational, centrifugal, electrostatic, osmotic and cappilary forces can be used to return the liquid from the condenser to the evaporator. Simple heat pipes are generally made in the shape of circular cylinders.

One of the most common heat pipes is a thermosyphon, a simple, closed, wickless heat pipe assisted by gravity in which the condenser section is located above the evaporator section. The liquid travels with the help of gravity to the evaporator section. A thermosyphon is sensitive to the liquid fill volume. The more liquid volume, the better the heat transfer up to a specific limit. Sometimes a wick structure is used in a thermosyphon to postpone flooding and to improve the contact between the wall and the liquid.

Another common heat pipe is a conventional heat pipe also known as a capillary driven heat pipe. A capillary driven heat pipe consists of a sealed cylindrical container, working fluid and a wick. The purpose of the wick is to return the condensate to the evaporator. The wick creates a capillary force at the liquid-vapor interface which drives the liquid to the evaporator section where it changes into vapor and travels to the condenser section due to the high vapor pressure in the evaporator section. The latent heat of vaporization is removed from the condenser, which condenses the vapor back to liquid. One of the limitations of a capillary driven heat pipe is the capillary limit which occurs when the wick cannot return enough liquid to the evaporator to keep it saturated, and the evaporator wall experiences a sudden increase in temperature. Capillary driven heat pipes are used in notebooks, laptops, and other computers to dissipate heat from the processors. Many other heat pipes come in all shapes and sizes depending upon their usage, for example, annular heat pipes, vapor chambers, rotating, gas loaded, loop, capillary pumping loops, pulsating, micro and miniature, inverted meniscus, monogroove and non-conventional.

Effects of working fluids, container materials, and wick designs

The working fluid of a good heat pipe should have high thermal conductivity, high latent heat, and high surface tension. The temperature range, boiling point and melting point should also be considered when choosing the working fluid. Before choosing a container, the compatibility of the working fluid, container and wick should be considered. The longevity of a heat pipe depends upon the container which ensures the content material does not react chemically with the working fluid. The content material should also be able to withstand the operating temperature. Generally, containers are metallic cases which are made using materials such as copper, stainless steel and aluminium. However, lightweight heat pipes used in electronic devices or aircraft applications demand aluminium alloys; their heat pipe containers are therefore made from beryllium-based alloys,

epoxy-impregnated carbon fibers, etc (Dancy et al. 1978, Fries et al. 1991, Corman et al. 1977). Non-metallic heat pipes are made up of ceramic containers to increase the rigidity depending upon the requirements: Jones at al. (2003). The wick design is also an essential factor for generating capillary pressure. Small pores are required to generate large capillary pressure, while large pores are preferred to ease the flow of liquid. These are the reasons that led to the development of many different types of optimized wick designs. Simple construction, installation and cost are the major factors for wick design. In order to design a wick, three important properties should be kept in mind:

- Minimum capillary radius: When a large capillary pressure difference is required, this parameter should be small.

- Permeability: This parameter measures the resistance of a wick to the axial flow of fluid. A low permeability wick increases the thermal conductivity of wick region (Elnagger et al. 2013). But a small permeability may also impede the liquid flow along the length of the adiabatic section. Therefore a wick has to be selected which has a permeability that balances capillary action with viscous drag.

- Effective thermal conductivity: If the effective thermal conductivity of a heat pipe is large, there is a small temperature drop across the wick which enhaces the performance of a heat pipe (Hui et al. 1999, Ochs et al. 2008).

1.0.2 Limitations of heat pipes

heat pipes are steady operation devices. Therefore, the functioning of a heat pipe has several operating limits. These operating limits are defined by physical phenomena such as the entrainment limit, capillary limit, sonic limit, boiling limit, frozen limit and start up limit. Other physical phenomenas are vapor pressure and condenser effects.

The capillary limit affects the dry out limit and occurs when the evaporator section does not have enough liquid pumped into it. This limit occurs when the capillary pressure drops are less than the liquid and vapor pressure drops. Because gravity is the driving force in a thermosyphon, the capillary limit is never reached. The sonic limit occurs when the vapor velocity becomes more than the speed of sound. The boiling limit occurs when the wick in the evaporator section dries out due to extended boiling. When the droplets of liquid enter the vapor phase owing to interfacial shear, then the entrainment limit comes into the picture. If the entrainment limit is reached, the

evaporator will dry out. The flooding limit occurs in large thermosyphons and is dependent on the liquid fill ratio. Faghri. (2016) has presented all the different types of limits in detail.

1.0.3 Modelling the adiabatic section of heat pipes

With the above explanation of the application, operation, and limitations of the heat pipe in mind, we used core annular flow theory to model the adiabatic section of a heat pipe. Because we are only modelling the adiabatic section of a heat pipe, some of the limits mentioned above are not our concern. The previous research by Busse et al. (2013), McHale et al. (2011), and McHale et al. (2010), discussed the gas layer in contact with the solid layer. In a heat pipe, however, the liquid layer is in contact with the solid wall, and this orientation is a major difference in our study. Before beginning our discussion of the heat pipe model, it is necessary to understand some physical phenomena of a liquid-vapor interface:

- Surface tension: When there is contact between liquid and another liquid, a solid, or a gas, then there is a formation of a thin film at the boundaries between the different phases. When liquid molecules are surrounded by the same liquid molecules, they experience the same force of attraction on every side, resulting in the formation of the film. Nevertheless, when the liquid molecules are near the liquid-vapor interface, they experience a molecular attraction towards the liquid, and this molecular attraction is greater than the force of the vapor molecules. Therefore, the liquid tends to take the shape of the minimum area under tension. If there is an increase in the liquid's surface area, the liquid to liquid molecular forces is decreased. Surface tension is defined as the work required to increase the surface area of the liquid.

- Contact angle: After defining surface tensions for the three mediums at each interface, the contact angle is defined from the force balance of the surface tensions of the three phases at the boundary line. The value of the contact angle tells us about the wetting property of the solid material used. The contact angle gives us a sense of whether the material is hydrophilic or hydrophobic, information which can be used to select the wick material. Hydrophilic materials are often selected for the wick.

- Capillary pumping: The wick structure gives rise to capillary pressure which eventually creates a pressure difference at both the ends of the heat pipe. The pressure difference created at the ends of the heat pipe helps to pump the liquid from the condenser to the evaporator and provides the circulation of the fluid.

- Capillary pressure: When we talk about heat pipe, the term ′capillarity′ often comes into the picture. Capillarity measures the flow of liquid under its own surface tension flows. As mentioned above when discussing heat pipes, the capillary pressure difference is something that causes the flow in a heat pipe. Capillary pressure is generated when there is a difference in curvature at the liquid- vapor interface and the existence of surface tension.

- Mass Flow rate: A heat pipe is a self-sufficient device. At steady state the mass flow rate of liquid is equal and opposite to the mass flow rate of vapor. In our analysis, we have satisfied the equal and opposite mass flow rate condition inside the heat pipe. The model presented in this work focuses on the maximum mass flow rate, which maximizes the axial heat transfer. We have also presented some limits to the pressure gradients inside a heat pipe.

In this thesis, we have presented mathematical modeling to study the flow in the adiabatic section of heat pipes in four different geometries. Mathematical modeling is an art of representing physical problems mathematically by sorting out the whole spectrum of effects that play a role and making a judicious selection of including the relevant effects and neglecting the small effects. In our mathematical model we have adopted core annular flow theory for liquid-vapor flow for a planar geometry as was done by Busse et al. (2013). The first mathematical model presented was the planar geometry of a heat pipe devoid of a wick. The model shows the functioning of a heat pipe in a planar geometry, and the flow of liquid and vapor in the adiabatic section. Our flow in vapor and liquid is considered laminar and is within all the limits of the heat pipe that were mentioned above. As mass flow rates are derived by using velocity, we have presented the velocity profiles after maintaining the equal and opposite mass flow rates in liquid and vapor. All our equations are non-dimensionalized using appropriate parameters. The equation of equal and opposite mass flow rate allows us to express the ratio of pressure gradients of vapor and liquid. We found that that the ratio of pressure gradients depends on the ratio of viscosity and the ratio of density. Therefore, we get a solution space for a heat pipe′s density ratio and viscosity ratio. Finally, we have investigated the optimum liquid layer thickness required to obtain the maximum mass flow rate. It seems logical that increasing the liquid volume will increase the mass flow rate, but one concern arises: an aggressive increase in the liquid fill ratio chokes the vapor area, which results in a lower mass flow rate.

With a similar analogy to heat pipes devoid of a wick, we can reintroduce the wick-based heat pipe for a planar geometry. Accordingly, there are a few more variables and parameters introduced in this model. With the introduction of the wick, permeability and porosity come into the picture.

Permeability has been discussed above in the heat pipes section 1.0.1. We have used the Karmen-Cozeny equation to define permeability. The wick we have used is a screen type wick, and we have modified permeability to be suitable for screen type wicks. Due to the relation be-

tween permeability, porosity and the wire diameter used, we have used the relationship between permeability of the wick diameter and wire thickness in the wick. Porosity is defined as the ratio of the percentage of empty space with the total volume. Therefore, porosity can also be related to the wire thickness and the spacing between the wires. These two relationships help us to reduce the total number of parameters introduced due to the wick.

In our models, we have avoided considering a flooded wick, because we do not have an interface which could give rise to capillarity in case of a flooded heat pipe. Moreover, we have a surface tension driven flow; therefore, we need interface curvature formed due to the contact of all three phases (liquid, vapor, and wick).

Taking the path of having a non-flooded porous medium, we provide room for the vapor phase to enter the porous medium and then form an interface inside of it. Therefore, we now have two interfaces. The first interface is the usual liquid-vapor interface formed inside the porous medium. The second interface is the porous medium and the free medium interface; this introduces a boundary condition which has some new parameters and is discussed in chapter one. Thus, our solution space in wick-based geometry has a few new variables.

Following the same way as we did in wickless geometry, we have defined the governing equations that will drive the flow. The governing equations are different than the wickless case as we must deal with Darcy′s law due to the flow in the porous medium. However, we have used the Brinkmann equation for flow in a porous medium, and the reason for this is explained in section 2 of chapter 2. Keeping all this in mind in the case of planar geometry with wick, we have maintained the equal and opposite mass flow rates in liquid and vapor, and we have shown and plotted the velocity profiles expressions. Furthermore, we have again shown the optimum liquid fill ratio by changing all the new variables present due to the porous medium. The optimum mass flow rates have been plotted with respect to the liquid fill ratio.

In regard to the pressure gradient ratio for vapor and liquid, we get an expression by using the equal and opposite mass flow rate equation. However, the expression of the ratio of pressure gradients must satisfy the wick constraints and bring surface tension and contact angle into the picture. The constraints and their derivation for our model have been discussed in detail in section 2 of chapter 2. Thus, the presence of these constraints sets a limit on the derived ratio of pressure gradients and we obtain the correct solution space, i.e., the suitable viscosity ratio and density ratio to drive the flow inside a heat pipe.

Finally, we have shown how the solution space changes by changing the surface tension and the contact angle. As the flow inside a heat pipe is a surface tension driven flow, we have shown different solution sets with the help of a plot containing isolines for different surface tension values. Similarly, different contact angles also play an essential role in driving the flow of liquid; therefore, we have shown isolines with different contact angles containing the respective solutions sets.

We have borrowed some of the ideas from the planar geometry devoid of a wick to model the flow of a cylindrical thermosyphon. The introduction of a cylindrical geometry comes with some additional algebraic challenges. We have used the equations and boundary conditions to express the velocity profiles of liquid and vapor inside a thermosyphon. However, a thermosyphon is placed at an angle, rather than horizontally, to use the force of gravity for the flow of liquid. We have shown the model placed in a horizontal position to avoid the complications of the angle.

We have again shown the optimum fill ratio required to have a maximum mass flow rate. Again, we have derived an expression for the ratio of pressure gradients in terms of the density and viscosity ratio. The introduction of cylindrical geometry gave us the idea of modelling a capillary driven heat pipe which has a cylindrical shape as is the case with most conventional heat pipes.

Following the model for the adiabatic section of the thermosyphon, we must realize that a conventional capillary driven heat pipe includes a wick and has a cylindrical shape. Section 3 of chapter 2 presents a theoretical model of a heat pipe containing a wick. The presence of a wick and the cylindrical structure together introduces new complications other than those we had in the planar wick-based model. The presence of the wick and the cylindrical Brinkman equation together results in a governing equation which is different than all the above cases, and we arrive at the solution using Bessel′s function of the first kind.

Solving the governing equations and the boundary conditions involved which are the same as we had in the planar wick−based geometry but are now in cylindrical coordinates we get the velocity expressions for liquid and vapor. We have satisfied the equal and the opposite mass flow rate conditions and the obtained theoretical expressions were plotted to show the velocity profiles for the liquid and vapor phases. We have shown the optimum fill ratio with different parameters involved due to the introduction of a porous medium.

Finally, as in the case of planar geometry, we have obtained the limit for the pressure gradient ratio depending upon the wick geometry. Due to the complications associated with the cylindrical geometry, we have not provided the expressions for the pressure gradient ratio. The obtained pressure gradient ratio limit was plotted with the surface plot of all the pressure gradient ratios obtained by solving the mass flow rate equation. We also provided isolines for various surface tension and contact angles, showing the solution space.

1.0.4 Robustness

We have compared the results of our model with an experimental investigation of a heat pipe done by Shafahi et al. (2008). Shafahi et al. (2010) studied the thermal performance of a cylindrical heat pipe using nanofluids. They found that introducing nanoparticles into the liquid increases the thermal performance of the heat pipe. They also found that the smaller the size of the particles, the better the effect of the temperature gradient of a heat pipe. Shafahi et al. (2008) used the

parameters from another theoretical and experimental study done by Vafai et al. (1998). Vafai et al. (1998) presented a two-dimensional analytical model of low-temperature cylindrical heat pipes. They showed the solution for liquid-vapor interfacial hydrodynamic coupling and considered non-Darcian transport in the wick. They provided the velocity profiles, pressure distributions and the heat pipe capillary limit.

We have used the results obtained by Shafahi et al. (2010) for the case of zero concentration of nano−particles in the liquid to validate our model. We used the same parameters for the length of the adiabatic section, and the same temperature, type of liquid, liquid fill ratio and wick properties to obtain the pressure gradient ratio that they obtained. We got similar values for the pressure gradient ratio proposed in chapter 2.

1.0.5 Limitations of our model

The work presented in chapter 2 was the modelling of liquid−vapor counterflow in a heat pipe using core annular flow theory. One inconsistency that our model contains is that the interface is assumed to be flat insofar as applying a shear stress boundary condition but curved insofar as supporting the capillary pressure required to drive the flow of liquid. A heat pipe unassisted by gravity requires capillary pumping and requires the radius of curvature of the liquid−vapor interface to be larger at the evaporator end than it is at the condenser end. This difference gives rise to a difference in capillary pressure between the condenser section and the evaporator section that supports the flow of liquid (and vapor). Our heat pipe model ignores any kind of interface deflection and surface chemistry effects.

In chapter 3 we present a work which substantiates our model presented in chapter 2 about using a flat interface instead of a deflected interface. Chapter 3 will show the effect of using a deflected interface on the velocity profiles in the porous medium. The physical model considered in chapter 3 is simplified slightly but retains the essential features which are required to determine the effect of a deflected interface. We have used perturbation theory to solve the problem considered in chapter 3.

Solving a perturbation problem is predicated on the idea that we have in chapter 2 a fairly good model which describes a phenomenon, but if we want to improve the model, we have to include some aspects or effects which were previously ignored, even if the effects in question are relatively small. The adding of new effects will lead to change in model and makes the equations more complex and difficult to solve. To quantify the small effect in a model, we introduce a small positive dimensionless parameter Φ. In general terms, the physical meaning of Φ depends on the problem but is always the ratio between two inherent length scales, time scales, or other characteristic quantities of the problem.

An improved model is only the next step in the modelling hierarchy but not the exact model

and “an exact solution of an approximate model is not better than an approximate solution of an exact model" (Rienstra & Sjoerd. 2018). Once we have the accepted approximate solutions, we can increase the complexity of the model to study the significance of effects in more efficient way. Formalizing the method of utilizing the systematic approach of adding the small effects in the model is the central aim of any perturbation problem. “perturbation methods"(Rienstra & Sjoerd. 2018). In this fashion, we recall the following quote due to David Crighton: David Crighton(1994) called ”Asymptotics − an indispensable complement to thought, computation, and experiment in applied mathematical modeling”.

In chapter 3, we have considered the liquid and vapor flow only inside a porous medium as our focus lies within the porous medium where there is the formation of an interface. Therefore, for simplicity, we have the entire domain in the porous medium where both the porous medium and the vapor phase extends infinitely. The liquid has a finite thickness and is in contact with the wall, and the vapor flows on top of the liquid and extends infinitely, whereas in chapter 2 the vapor layer is also finite. In chapter 3, we have avoided maintaining an equal and opposite mass flow rate as the vapor layer extends infinitely. Rather, we have maintained an equal and opposite pressure gradient in the liquid and vapor phase. We use square wires instead of circular wires in our porous medium because, in the case of square wires, only the vertical position of the triple point changes, whereas with circular wires, both the vertical and horizontal position of the triple point changes. The change in vertical and horizontal positions of the triple point makes the volume conservation of the liquid displaced due to the meniscus below and under the flat interface very complex.

We have presented an expression for an interface which depends upon the horizontal spacing between two wires. We have shown that the deflection of the interface depends upon the pressure difference. Increasing the pressure difference up to a certain limit increases the interface deflection. Similarly, decreasing the surface tension or using a fluid with less surface tension also increases the interface deflection. We have plotted the interface deflection for the same values of parameters used in chapter 2, except for the liquid fill ratio. The liquid fill ratio is taken to be different because of some mathematical complications that occur while solving the governing equations.

The interface boundary conditions are satisfied at a deflected interface and therefore linearized. Now we perturb our solutions, i.e., our velocities with a small parameter of Φ. We assumed a perturbation based solution to the governing equation for liquid and vapor, which is given by the Brinkman equation. Firstly, we equated only the zeroth−order solution of the small parameter, which depicts some similarity with our model presented in chapter 2. The reason why the zeroth−order solution is similar to the solutions in chapter 2 is that it has its interface boundary condition satisfied at a flat interface which is the height of the liquid layer. Then we solved by equating the higher−order terms of the small parameters. To be precise, we only considered first−order terms and ignored all the higher-order terms of the small parameter. The solution to

the governing equation and the boundary conditions required both a Fourier and a Taylor series transformation. The method for the solution was elaborated on in chapter 3. The composite solution takes into account the deflected interface; therefore, we compared the leading order solution, which is the zeroth−order, having all the boundary conditions satisfied at the flat interface with the composite solution.

The velocity profile for composite solutions depends upon the horizontal distance between the two wires. We have presented the velocity profiles for composite solutions for different horizontal positions. Finally, we have shown the interface deflection corresponding to the difference in velocity for different values of liquid layer thickness.

In chapter 3, we found that there is a discontinuity of the velocity at the interface. This is because the boundary conditions at the interface are linearized, and the higher−order terms of the small parameter are ignored in the first−order solution, which accounts for the composite solution. The discontinuity between the velocity at the interface increases as the interface deflection increases. We have also shown the velocity difference between the leading order solution and the composite solution, corresponding to the interface deflection. It was shown that the velocity difference is more significant only at the interface but is negligible at all other positions of the domain. Therefore, we determined that the results obtained in chapter 2 considering a flat interface are not of limited value. The analysis shown in chapter 3 can also be done using circular wires by simply removing the extra volume of wires.

Chapter 2

Core annular flow theory as applied to the adiabatic section of heat pipes

2.1 Abstract

Core annular flow theory is used to model the parallel flow of fluids of different phases and has been used to describe drag reduction in the context of internal flows bounded by superhydrophobic surfaces. The work presented here is an extension of core annular flow theory to the study of the adiabatic section of heat pipes. Our aim is to develop a first-principles estimate of the conditions necessary to maximize the (counter) flow of liquid and vapor and, by extension, the axial flow of heat. Both planar and axisymmetric geometries are examined as are heat pipes containing versus being devoid of a wick. In the wick versus no-wick cases, the peripheral return flow of liquid is respectively driven by capillarity and by gravity. Our model is used to predict velocity profiles and the flux-maximizing pressure gradient ratio (vapor-to-liquid). We further obtain estimates for the optimum thickness of the liquid layer. Note finally that when the liquid flow occurs via capillary pumping, there is a minimum surface tension below which the wick cannot supply a sufficient flow of liquid. We characterize this critical point in terms of the properties of the working fluid and of the wick.

2.2 Introduction

Core annular flows are internal flows where a core of viscous liquid is surrounded by a sheathing layer of lower viscosity, be this liquid or gas e.g. air (Ooms et al. 2007). Because the viscous liquid does not then make direct contact with the boundaries of the confining geometry (e.g. the inner surface of a pipeline), drag is reduced. This realization has been used to positive effect in, say, the transport of heavy oils where the addition of a thin layer of water along the inner surface of the pipeline results in a nontrivial drop in the overall shear stress (Joseph et al. 1995, Joseph et

al. 1997, Gruncell et al. 2013).

More recently, there has emerged a significant interest in the prospect of depressing drag using superhydrophobic surfaces, which support a continuous layer of air and thereby separate the solid from the (aqueous) liquid. This scenario has been explored in the context of flows characterized as either external (McHale et al. 2010, McHale et al. 2011) or internal (e.g. Panchanathan et al. 2018). Of particular relevance to this study is the theoretical investigation by Busse et al. (2013), which defined, for a variety of steady, laminar internal flows (i.e. Couette flow, symmetric channel flow, pressure-driven channel flow and pipe flow), upper limits to the overall drag reduction. Whatever the flow type, such upper limits are associated with a air layer of intermediate thickness. If the air layer is too thin, then it plays a modest role in reducing the overall shear stress. If, by contrast, the air layer is too thick, insufficient cross-sectional area is available for the flowing liquid and the drag must again increase.

One of the limitations associated with Busse et al. (2013) is that the air layer is assumed to either (i) have no net downstream flow, or, (ii) to flow owing to the shear force imposed by the overlying liquid. The latter assumption is the more reasonable one but, from a practical point of view, it begs the question of how the air layer is replenished. Although alternatives to upstream injection have been considered (e.g. Panchanathan et al. 2018 examine the possibility of chemical re- action), further research is needed to optimize such schemes at scales ranging from lab-on-a-chip designs to large-scale marine vessels.

Extending the work of Busse et al. (2013), we explore below the non-core annular flow scenario of an equal and *opposite* counterflow of vapor and liquid. This counterflow, representing the first major difference with Busse et al.'s study, is made possible by evaporation and condensation, which occur at the far ends of the control volume. To this end, we have in mind studying, in generic terms, the flows that arise within the adiabatic section of heat pipes. heat pipes are "thermal superconductors" in that they can readily (and passively) transfer heat by exploiting phase change. Owing to their versatility and low maintenance costs, they have found application everywhere from aerospace (Shukla et al. 2015) to electronics (Pastukhov et al. 2003) to nuclear power generation (Hampel et al. 1989) to building heat recovery (Gan et al. 1998). The key components of a heat pipe are illustrated schematically in figure 2.1 and consist of a working fluid within a closed container, the hot end of which is the evaporator and the cold end of which is the condenser. Working fluid evaporated in the evaporator flows as a vapor along the central core of the heat pipe. Between the evaporator and the condenser is the adiabatic section, which is often longer than the other two sections combined (Qu et al. 2008). In other designs, the adiabatic section is instead omitted e.g. that of Zhu & Vafai (1998), which includes vertical and horizontal wick structures. Working fluid evaporated in the evaporator flows as a vapor along the central core of the heat pipe. Upon reaching the opposite end, condensation occurs and the resulting liquid flows back to the

evaporator. Oftentimes (and as explored in sections 3 and 5 below), a wick is included along the heat pipe inner surface in order to facilitate this return flow of liquid, i.e. by capillary pumping (Reay et al. 2013, Zohuri 2011, Peterson 1994, Faghri et al. 2012). At steady state, the mass flow rates of the liquid and the vapor must be equal in magnitude. However, because $\rho_v \ll \rho_l$, where ρ_v and ρ_l are the densities of vapor and liquid respectively, $u_v \gg u_l$ where u_v and u_l respectively indicate the vapor and liquid flow velocities.

With the above description in mind, we now identify the second major difference with the work of Busse et al. (2013), namely that the vapor layer appears in the core rather than along the periphery. Corresponding to this change of orientation, our focus is not on drag minimization by the lubrication of a more viscous fluid with a less viscous fluid. Rather, and with reference to a parameter space that considers liquid/vapor fluid properties and geometric parameters, we look to identify the point of maximum mass flow rate, which corresponds also to the point of maximum axial heat transfer.

For simplicity, the above calculation is first completed by neglecting, similar to Busse et al. (2013), McHale et al. (2011) and McHale et al. (2010), the role of surface micro-topography. In this instance, our heat pipe is actually more properly considered as a thermosyphon where liquid flows owing not to capillary pumping but rather to the pull of gravity. Thereafter, we consider a screen-type wick structure within the heat pipe and so model the flow of liquid as one that (i) is driven by capillarity, and, (ii) occurs through a porous medium. This calculation step represents the third major difference with the work of Busse et al. (2013); it introduces a number of new variables, geometric and otherwise, for characterizing the porous medium.

The rest of the manuscript is organized as follows: In sections II and III, we present the calculations related to a heat pipe with a rectilinear geometry. Because heat pipes much more typically feature a circular cross-section, we extend our model to a cylindrical geometry in sections IV and V. Finally, in section VI, we summarize key findings and offer ideas for future work.

2.3 Planar geometry, no wick

This section presents calculations for a heat pipe devoid of an internal wick structure. We impicitly assume, therefore, that the liquid flow is driven by gravity, the body force term being incorporated into the pressure gradient term in the governing equations to follow. Technically speaking, this renders our heat pipe into a thermosyphon, although we will avoid this terminology here and thereby maintain a consistent nomenclature throughout the exposition. Figure 2.1 shows the (planar) geometry of a heat pipe without a wick structure.

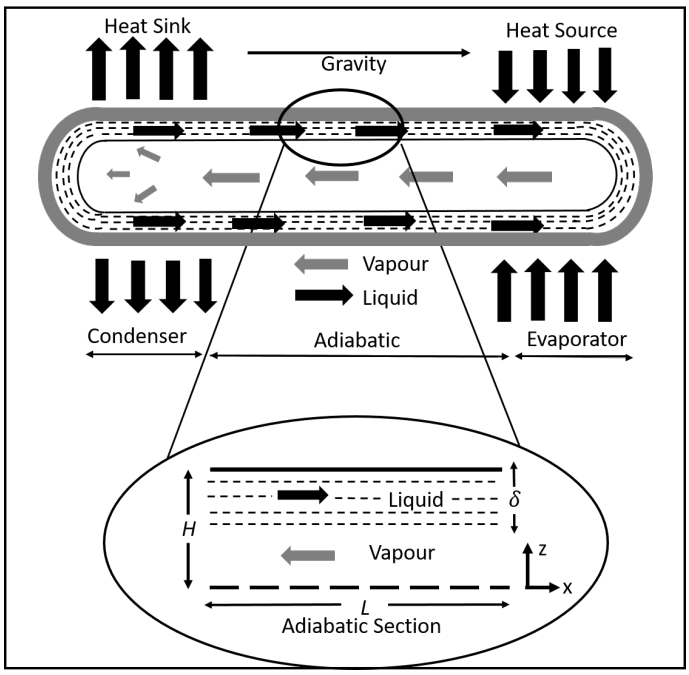

Figure 2.1 – Heat pipe geometry (no wick). The liquid vapor interface is not separated by a wall.

2.3.1 Governing equations and solutions

The governing equations are given by the Poiseuille flow equations where we assume an incompressible, steady and laminar flow in both phases. This latter assumption is made for convenience, but is not essential. In other words, the equations to be presented below can be recast assuming e.g. a vapor velocity satisfying a modified form of von Kármán's law of the wall. We avoid following this path here: assuming a turbulent vapor flow renders the algebra more tedious without adding much additional physical insight. With the above assumptions to hand, the Poisseulle flow equations for liquid and vapor read as follows:

$$\mu_v \frac{d^2}{dz^2} u_v = \frac{dp_v}{dx} \equiv \pi_v < 0 \qquad 0 < z < H - \delta \tag{2.1}$$

$$\mu_l \frac{d^2}{dz^2} u_l = \frac{dp_l}{dx} \equiv \pi_l > 0 \qquad H - \delta < z < H \tag{2.2}$$

where u_v and u_l are the velocities for vapor and liquid, respectively, π_v and π_l are the pressure gradients in the vapor and liquid, respectively, and μ_v and μ_l are the corresponding dynamic viscosities. Moreover, π_v and π_l are, respectively, the pressure gradients in the vapor and liquid. In the heat pipe context, these can be related to the axial heat flux and the temperatures of the evaporator and condenser using the methodology outlined in Appendix B. Complementing (2.1) and (2.2), the standard no slip boundary condition is applied at the upper surface, $z = H$, and a symmetrical boundary condition is applied along the heat pipe axis, $z = 0$. At the interface between the liquid

and vapor, the viscous shear stress must be continuous i.e.

$$\mu_v \left(\frac{du_v}{dz}\right)_{z=H-\delta} = \mu_l \left(\frac{du_l}{dz}\right)_{z=H-\delta} \tag{2.3}$$

Moreover,

$$u_v(z = H-\delta) = u_l(z = H-\delta)\,. \tag{2.4}$$

Finally, a global mass balance equation must be satisfied by which

$$-\dot{m}_v = \dot{m}_l \qquad \text{where} \qquad \dot{m}_v = \rho_v \int_0^{H-\delta} u_v dz \tag{2.5}$$

$$\text{and} \qquad \dot{m}_l = \rho_l \int_{H-\delta}^{H} u_l dz$$

The above equations are non-dimensionlized using H, μ_v and π_v as characteristic variables. Thus, we define

$$z^* = \frac{z}{H}, \qquad u_v^* = \frac{\mu_v}{H^2\pi_v} u_v \qquad \text{and} \qquad u_l^* = \frac{\mu_v}{H^2\pi_v} u_l,$$

where stars indicate non-dimensional variables. With benefit of the above characteristic variables, laminar flow conditions apply provided

$$\mathrm{Re} = u_v^* \frac{\rho_v H^3 \pi_v}{\mu_v^2} \lesssim 2100$$

in which Re is the Reynolds number. By the same token, the vapor flow can be considered incompressible provided

$$\mathrm{Ma} = u_v^* \frac{H^2\pi_v}{\mu_v \sqrt{\frac{\gamma \mathscr{R} T}{M}}} \lesssim 0.3$$

where Ma is the Mach number, γ is the ratio of specific heats, $\mathscr{R}$ is the universal gas constant, T is the absolute temperature and M is the molar mass. A corollary of assuming low Ma and low Re is that the entrainment limit defined Kemme (1968) is never reached. Using the above non-dimensional variables, the previously specified governing equations and boundary conditions may be rewritten as

$$\frac{d^2}{dz^{*2}} u_v^* = 1 \tag{2.6}$$

$$\frac{d^2}{dz^{*2}} u_l^* = \frac{c_\mu}{c_p} \tag{2.7}$$

$$u_l^*(z^* = 1) = 0 \tag{2.8}$$

$$\left(\frac{du_v^*}{dz^*}\right)_{z^*=0} = 0 \tag{2.9}$$

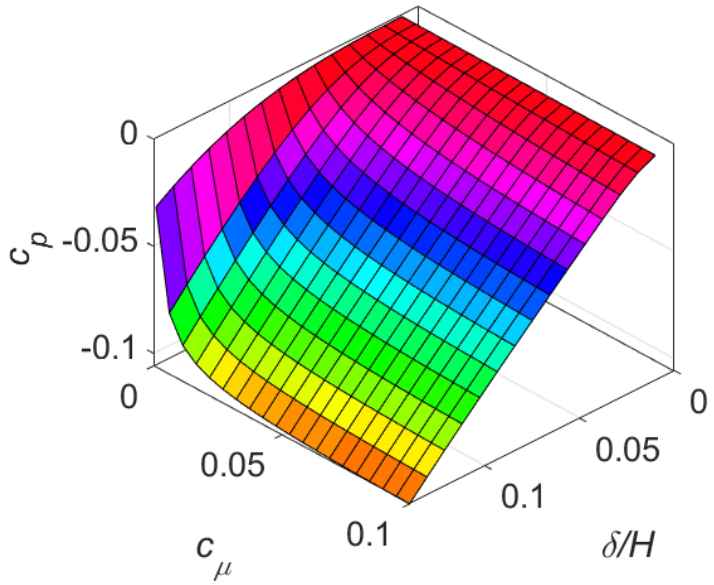

Figure 2.2 – Pressure gradient ratio, c_p, as determined from (2.15) versus c_μ and $\frac{\delta}{H}$ with $c_\rho = 10^{-4}$.

$$c_\mu \left(\frac{du_v^*}{dz^*}\right)_{z^*=1-\frac{\delta}{H}} = \left(\frac{du_l^*}{dz^*}\right)_{z^*=1-\frac{\delta}{H}} \tag{2.10}$$

$$u_v^*\left(z^* = 1-\frac{\delta}{H}\right) = u_l^*\left(z^* = 1-\frac{\delta}{H}\right) \tag{2.11}$$

where $c_p = \frac{\pi_v}{\pi_l} < 0$ is the pressure gradient ratio and $c_\mu = \frac{\mu_v}{\mu_l}$ is the dynamic viscosity ratio. Solutions to (2.6) and (2.7) respectively read as follows:

$$u_v^* = \frac{1}{2}z^{*2} - c_\mu\left[\frac{\delta}{H} + \frac{\delta^2}{2H^2}\left(1-\frac{1}{c_p}\right)\right] - \frac{1}{2} + \frac{\delta}{H} \tag{2.12}$$

and

$$\begin{aligned} u_l^* = {} & \frac{c_\mu}{2c_p}z^{*2} + c_\mu\left[1 - \frac{\delta}{H}\left(1-\frac{1}{c_p}\right) - \frac{c_\mu}{c_p}\right]z^* + \\ & c_\mu\left[\frac{\delta}{H}\left(1-\frac{1}{c_p}\right) - 1 + \frac{1}{2c_p}\right] \end{aligned} \tag{2.13}$$

2.3.2 Evaluation of c_p

The solutions prescribed by (2.12) and (2.13) are incomplete because they rely on c_p whose value is determined from (2.5). Expressing (2.5) using non-dimensional variables, we require that

$$c_\rho \int_0^{1-\frac{\delta}{H}} u_v^* dz^* + \int_{1-\frac{\delta}{H}}^1 u_l^* dz^* = 0 \tag{2.14}$$

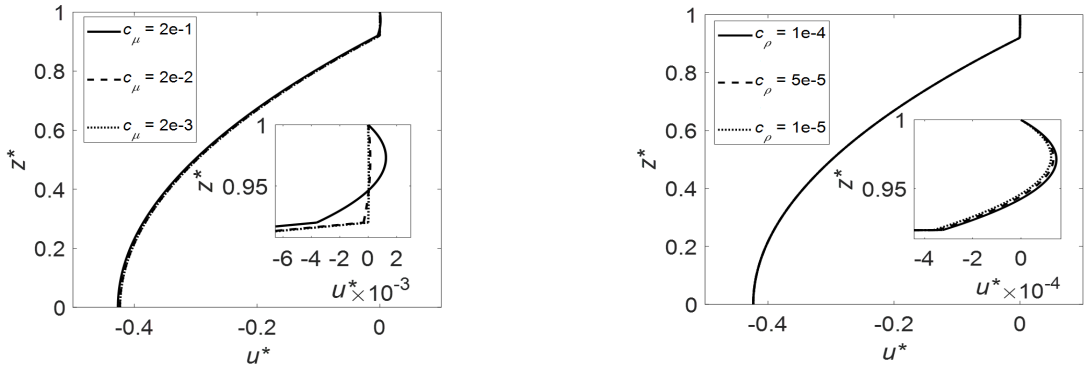

Figure 2.3 – (a) Composite velocity profiles for various c_μ with $c_\rho = 10^{-4}$ and $\frac{\delta}{H} = 0.08$. (b) Composite velocity profiles for various c_ρ with $c_\mu = 2 \times 10^{-2}$ and $\frac{\delta}{H} = 0.08$. The inset shows the velocity profile in the liquid section.

where the density ratio is defined as $c_\rho = \frac{\rho_v}{\rho_l}$. Applying (2.12) and (2.13) in (2.14) and solving (2.14) with the help of Newton-Raphson iterative root solver, yields the following solution for c_p in terms of c_μ, c_ρ and δ/H:

$$c_p = \frac{c_\mu \left(\frac{\delta}{H}\right)^2 \left[\left(\frac{\delta}{H}\right)(3c_\rho - 2) - 3c_\rho\right]}{\mathscr{D}} \tag{2.15}$$

where

$$\mathscr{D} = \left(\frac{\delta}{H}\right)^3 \left(6c_\mu c_\rho - 3c_\mu - 2c_\rho\right) + \left(\frac{\delta}{H}\right)^2 \left(-12c_\mu c_\rho + 3c_\mu + 6c_\rho\right) + \frac{\delta}{H} 6c_\rho \left(c_\mu - 1\right) + 2c_\rho$$

Figure 2.2 shows c_p versus $\frac{\delta}{H}$ and c_μ for fixed c_ρ. It can be seen that $|c_p|$ increases with $\frac{\delta}{H}$: as the liquid layer thickness increases, we require a smaller (larger) pressure gradient to drive the liquid (vapor) flow, which has the effect of increasing $|c_p|$. By similar reasoning, $|c_p|$ increases with c_μ (and also c_ρ). Once c_p is known, liquid and vapor velocity profiles may be computed from (2.12) and (2.13). Figure 2.3 a shows the composite velocity profiles for fixed $c_\rho = 10^{-4}$ and various c_μ. Corresponding results with c_μ fixed and c_ρ variable are shown in figure 2.3 b. Note that the curves in figures 3 a,b corresponding to different c_μ and c_ρ nearly overlap, a consequence of the manner in which the governing equations have been non-dimensionalized. Figures 3 a,b confirm that the vapor velocity is much larger than that of the liquid, this due to the fact that $-\dot{m}_v = \dot{m}_l$ but $\rho_v \ll \rho_l$ and hence $c_\rho \ll 1$.

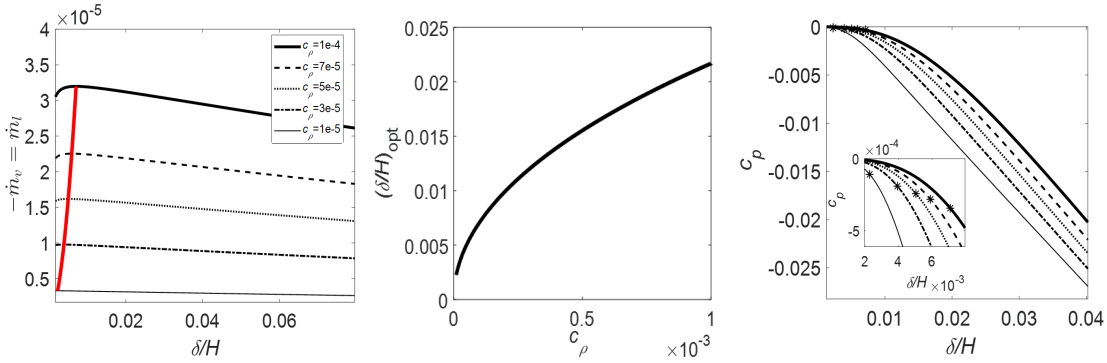

Figure 2.4 – (a) $-\dot{m}_v = \dot{m}_l$ versus $\frac{\delta}{H}$ for various c_ρ with $c_\mu = 2\times10^{-2}$. The thick red solid line connects the maxima of the individual curves and thereby defines $\left(\frac{\delta}{H}\right)_{\text{opt}}$ whose variation with c_ρ is shown in (b). (c) c_p versus $\frac{\delta}{H}$ for the same c_ρ considered in (a). Stars indicate $\left(\frac{\delta}{H}\right)_{\text{opt}}$.

2.3.3 Optimum liquid layer thickness

For fixed c_ρ and c_μ, we expect the mass flow rate, $-\dot{m}_v = \dot{m}_l$ to be a non-monotone function of δ/H c.f. Busse et al. (2013). If the liquid layer is too thin or too thick, a large drag will be experienced in the liquid and vapor, respectively. In turn, this large drag will limit the mass of fluid that can be moved in the axial direction. Our hypothesis is confirmed by inspection of figure 2.4 a which shows $-\dot{m}_v = \dot{m}_l$ as a function of $\frac{\delta}{H}$ for various c_ρ with fixed c_μ. Each curve exhibits a global maximum corresponding to an optimal value for the (non-dimensional) liquid layer thickness, $\left(\frac{\delta}{H}\right)_{\text{opt}}$. The variation of $\left(\frac{\delta}{H}\right)_{\text{opt}}$ with c_ρ is exhibited in figure 2.4 b. Note that $\left(\frac{\delta}{H}\right)_{\text{opt}}$ is a monotone increasing function of the density ratio: as the liquid density increases relative to the vapor, we require a lesser depth of liquid to achieve maximal axial transport of fluid and, in the heat pipe context, of heat. Extracting data from figure 2.4 b, figure 2.4 c shows the variation of c_p with $\frac{\delta}{H}$ where we have now specifically highlighted those optimum values for the non-dimensional liquid layer thickness as determined from the preceding analysis. The figure confirms that maximal transport is associated with small values of the pressure gradient ratio. As we shall show in the next section, larger values of c_p arise by forcing the liquid to flow through a wick.

2.4 Planar geometry, wick

A limitation of the studies by McHale et al. (2010) and Busse et al. (2013) is that they assume a "perfect" plastron layer, i.e. a surface-attached air layer that is supported without reference to surface microstructure. This omission is nontrivial because any such microstructural layer is expected to influence the flow. As a first step towards rectifying the above limitation, we build on the analysis of section 2 by specifically considering an idealized peripheral wick, which is, in real

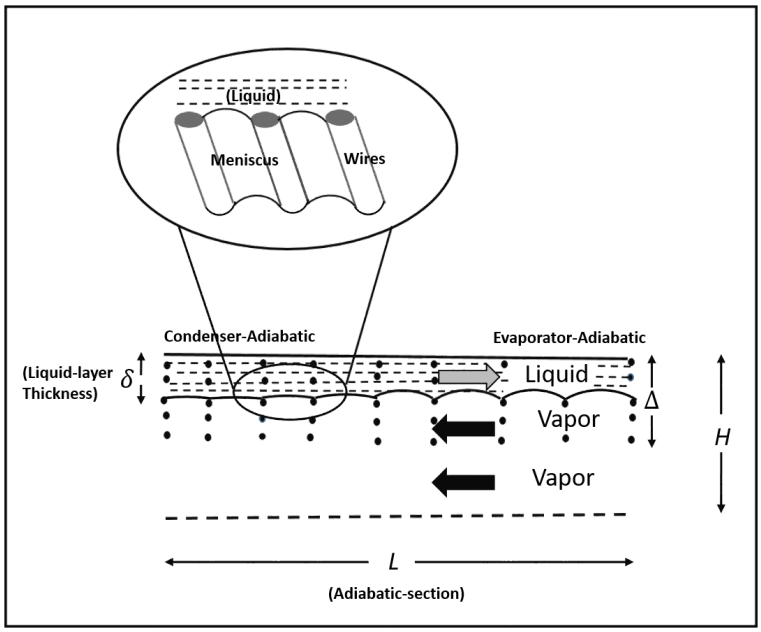

Figure 2.5 – Heat pipe geometry (with screen type wick). Schematic not to scale.

heat pipes, responsible for the capillary pumping of liquid from the condenser to the evaporator. Our wick is idealized in that, although it is of screen type, we ignore the contribution of the fibers aligned with the axis of the heat pipe. A further idealization in our analysis is to assume that the curvature of the liquid-vapor interface is sufficiently modest to allow an order-one linearization of inter-facial boundary conditions. In actual fact, capillary pumping requires that the radius of curvature of the vapor-liquid interface is lager at the evaporator end than it is at the condenser end. This difference gives rise to a difference in capillary pressure between the condenser section and the evaporator section that supports the flow of liquid (and vapor). Figure 2.5 shows the geometry of the porous medium and the alignment of the wires comprising the screen type wick.

2.4.1 Governing equations and boundary conditions

By assumption, and consistent with figure 2.5, vapor is present in the porous medium and also the free medium whereas liquid is present only in the porous medium. We assume that flow in the porous medium (whether liquid or vapor) is governed by the Brinkman equation. Brinkman's equation is derived from Darcy's law but includes a viscous shear dissipative term (Durlofsky & Brady 1987). Letting the velocity of vapor and liquid in the porous medium be represented, respectively, by U_v and U_l, the (dimensional) governing equations now read

$$\frac{\mu_v}{\varepsilon}\frac{d^2}{dz^2}U_v - \frac{\mu_v}{\kappa}U_v = \pi_v \tag{2.16}$$

$$\frac{\mu_l}{\varepsilon}\frac{d^2}{dz^2}U_l - \frac{\mu_l}{\kappa}U_l = \pi_l \tag{2.17}$$

Here ε and κ are, respectively, the porosity and permeability of the porous medium. The associated boundary conditions are given by

$$U_v(z = H-\Delta) = u_v(z = H-\Delta) \tag{2.18}$$

$$\left(\frac{dU_v}{dz}\right)_{z=H-\Delta} - \varepsilon\left(\frac{du_v}{dz}\right)_{z=H-\Delta} - \frac{\alpha\varepsilon}{\sqrt{\kappa}}U_v(z = H-\Delta) = 0 \tag{2.19}$$

$$U_v(z = H-\delta) = U_l(z = H-\delta) \tag{2.20}$$

$$c_\mu\left(\frac{dU_v}{dz}\right)_{z=H-\delta} = \left(\frac{dU_l}{dz}\right)_{z=H-\delta} \tag{2.21}$$

$$U_l(z = H) = 0 \tag{2.22}$$

$$\left(\frac{du_v}{dz}\right)_{z=0} = 0 \tag{2.23}$$

where Δ is the thickness of the porous medium exhibited in figure 2.5. As with the analysis of section 2, (2.18-2.23) include a no slip top boundary condition and a shear-free bottom boundary condition. Also familiar from our previous analysis are boundary conditions specifying a continuity of fluid velocity and of shear stress at the liquid-vapor interface, $z = H-\delta$ (Stallery 1970). Along the boundary, $z = H-\Delta$, between the porous medium and the free medium, (2.19) specifies an Ochoa-Tapia & Whittaker (1995)-type boundary condition that describes the shear stress exerted by the flowing vapor. (2.19) accounts for the momentum transport at the boundary between a porous medium and free medium. Here, α is a non-dimensional, $\mathcal{O}(1)$ coefficient that characterizes the excess stress along $z = H-\Delta$. For convenience, we set $\alpha = 1$ in the discussion to follow.

The above governing equations are non dimentionalized using the same characteristic variables as in section 2.1. Thus (2.1, 2.16-2.17) can be re-written as

$$\frac{d^2u_v^*}{dz^{*2}} = 1 \tag{2.24}$$

$$\frac{1}{\varepsilon}\frac{d^2U_v^*}{dz^{*2}} - \frac{H^2}{\kappa}U_v^* = 1 \tag{2.25}$$

$$\frac{1}{\varepsilon}\frac{d^2U_l^*}{dz^{*2}} - \frac{H^2}{\kappa}U_l^* = \frac{c_\mu}{c_p} \tag{2.26}$$

Analogously, the boundary conditions become

$$U_v^*\left(z^*=1-\frac{\Delta}{H}\right)=u_v^*\left(z^*=1-\frac{\Delta}{H}\right) \tag{2.27}$$

$$\left(\frac{dU_v^*}{dz^*}\right)_{z^*=1-\frac{\Delta}{H}}-\varepsilon\left(\frac{du_v^*}{dz^*}\right)_{z^*=1-\frac{\Delta}{H}}-\alpha\varepsilon\frac{H}{\sqrt{\kappa}}U_v^*\left(z^*=1-\frac{\Delta}{H}\right)=0 \tag{2.28}$$

$$U_v^*\left(z^*=1-\frac{\delta}{H}\right)=U_l^*\left(z^*=1-\frac{\delta}{H}\right) \tag{2.29}$$

$$c_\mu\left(\frac{dU_v^*}{dz}\right)_{z^*=1-\frac{\delta}{H}}=\left(\frac{dU_l^*}{dz}\right)_{z^*=1-\frac{\delta}{H}} \tag{2.30}$$

$$U_l^*\left(z^*=1\right)=0 \tag{2.31}$$

$$\left(\frac{du_v^*}{dz}\right)_{z^*=0}=0 \tag{2.32}$$

The general solutions for the vapor and liquid velocities are given by

$$u_v^*=-z^{*2}+az^*+b \tag{2.33}$$

$$U_v^*=A\exp\left(\frac{\sqrt{\varepsilon}H}{\sqrt{\kappa}}z^*\right)+B\exp\left(-\frac{\sqrt{\varepsilon}H}{\sqrt{\kappa}}z^*\right)-\frac{\kappa}{H^2} \tag{2.34}$$

$$U_l^*=A'\exp\left(\frac{\sqrt{\varepsilon}H}{\sqrt{\kappa}}z^*\right)+B'\exp\left(-\frac{\sqrt{\varepsilon}H}{\sqrt{\kappa}}z^*\right)-\frac{\kappa c_\mu}{H^2c_p} \tag{2.35}$$

The constants a, b, A, B, A' and B' are evaluated using (2.27-2.32). As before, the model is closed by insisting that, for the steady flows of interest here, there is an equal and opposite mass flow of liquid (to the evaporator) and vapor (to the condenser), i.e.

$$0=c_\rho\left[\int_0^{1-\frac{\Delta}{H}}u_v^*dz^*+\int_{1-\frac{\Delta}{H}}^{1-\frac{\delta}{H}}U_v^*dz^*\right]+\int_{1-\frac{\delta}{H}}^{1}U_l^*dz^* \tag{2.36}$$

Given the additional dynamics associated with the porous media flow, the list of key independent parameters is now longer than in section 2.3.1 in that it includes c_μ, c_ρ, $\frac{\delta}{H}$, $\frac{\Delta}{H}$, $\frac{H}{\sqrt{\kappa}}$, and ε. Each of these seven variables influences the value of c_p, which appears in (2.35) and is determined from (2.36). Owing to the expanded list of independent variables, we do not attempt to derive an analytical solution for c_p but rather compute this pressure gradient ratio numerically. To this end, representative values for most of the independent variables mentioned above are selected

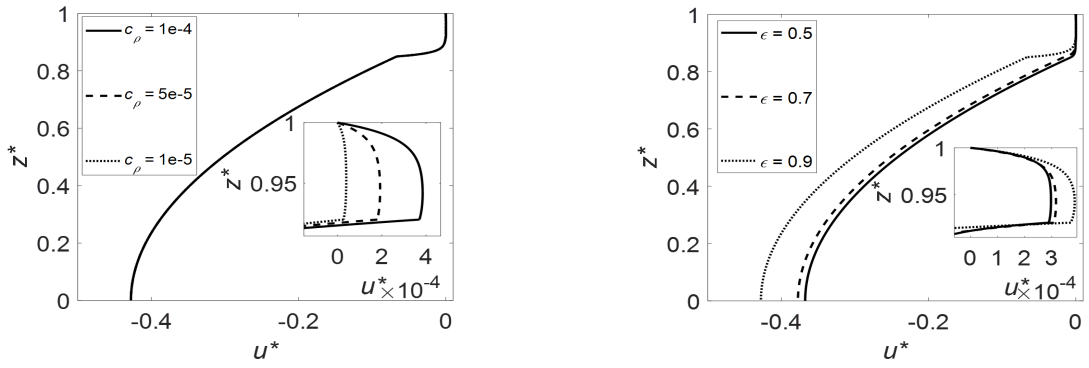

Figure 2.6 – (a) Composite velocity profiles for various c_ρ with $c_\mu = 2\times10^{-2}$, $\frac{\delta}{H} = 0.08$, $\frac{\Delta}{H} = 0.15$, $\varepsilon = 0.9$ and $\frac{H}{\sqrt{\kappa}} = 5766$. (b) Composite velocity profiles for various ε with $c_\rho = 10^{-4}$, $c_\mu = 2\times10^{-2}$, $\frac{\delta}{H} = 0.08$, $\frac{\Delta}{H} = 0.15$ and $\frac{H}{\sqrt{\kappa}} = 5766$. The inset shows the velocity profile in the liquid section.

with reference to the experimental values presented in the primarily-analytical work of Shafahi et al. (2010).

Figure 2.6 a is the analogue of figure 2.3 b; it shows composite velocity profiles for different c_ρ and $c_\mu = 2\times10^{-2}$. Figure 6 b is similar but considers the impact of changing the porosity, ε. As expected, increasing ε causes U_l (and, by extension, $|U_v|$) to likewise increase.

2.4.2 Optimum liquid layer thickness

As with the analysis of section 2.3.3, we wish to estimate the optimum liquid layer thickness, $\left(\frac{\delta}{H}\right)_{\text{opt}}$ whereby the axial transport of mass (and heat) is maximized. Figure 2.7 a shows the variation of $-\dot{m}_v = \dot{m}_l$ with the liquid layer thickness for various c_ρ. Unlike in figure 2.4 a, mass flow rates very close to maximal are realized over a broad range of $\frac{\delta}{H}$. From a practical point of view, this observation is positive: it suggests that the heat pipes in question will perform at very close to their optimal level even if the liquid fill ratio is above or below the value prescribed by $\left(\frac{\delta}{H}\right)_{\text{opt}}$. The maximum mass flow rates prescribed by figure 2.7 a are smaller than those reported in figure 2.4 a, this a consequence of restricting the liquid flow to occur only within the wick. Figure 2.7 b shows $\left(\frac{\delta}{H}\right)_{\text{opt}}$ vs. c_ρ. As before, $\left(\frac{\delta}{H}\right)_{\text{opt}}$ increases with the density ratio. Figure 2.7 c shows c_p versus $\frac{\delta}{H}$ for different c_ρ where the stars indicate the optimum liquid layer thickness as determined from figure 2.7 a. Figures 2.8 and 2.9 are similar to figure 2.7, but consider the variation of $-\dot{m}_v = \dot{m}_l$ with $\frac{\delta}{H}$ for various $\frac{\Delta}{H}$ and ε, respectively. Note that, in contrast to figure 7 b, the variation of $\left(\frac{\delta}{H}\right)_{\text{opt}}$ exhibited in figure 8 b and 9 b is non-monotone: when Δ/H increases, more and more of the vapor must flow through a porous medium. As a result the maximum mass flow rate is eventually associated with smaller $\left(\frac{\delta}{H}\right)_{\text{opt}}$. Similarly, as $\varepsilon \to 1$ there is more available

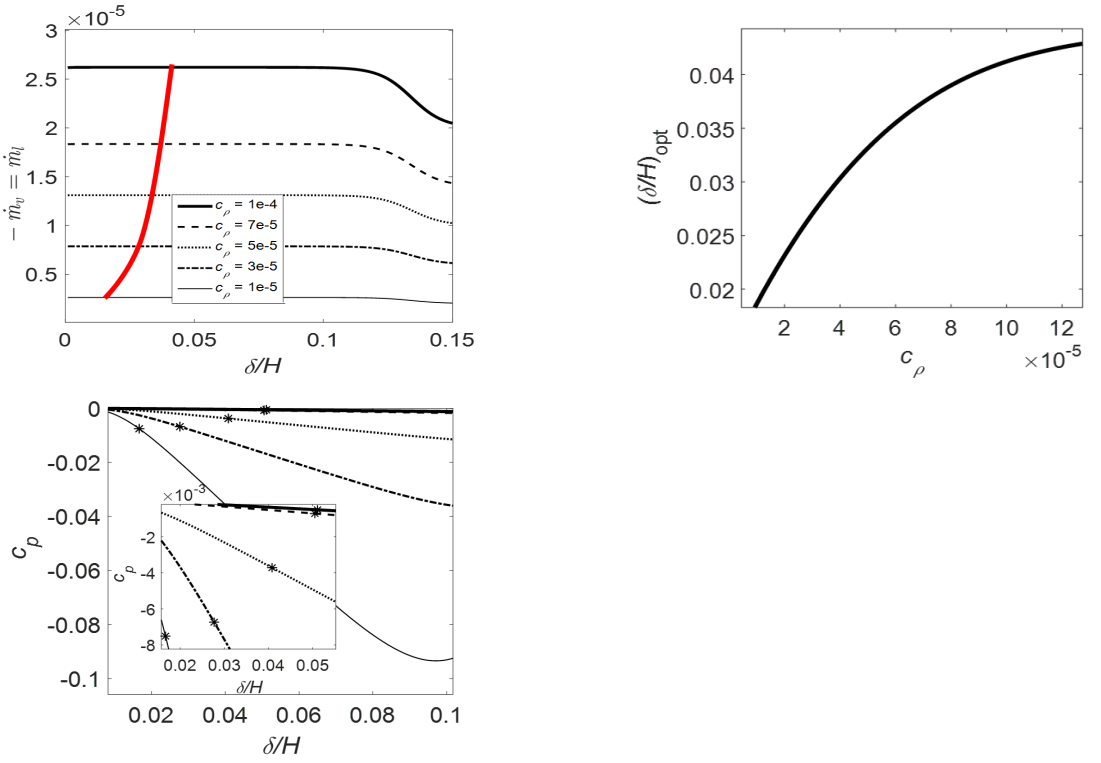

Figure 2.7 – (a) $-\dot{m}_v = \dot{m}_l$ versus $\frac{\delta}{H}$ for various c_ρ with $c_\mu = 2 \times 10^{-2}$, $\frac{\Delta}{H} = 0.15$, $\varepsilon = 0.9$ and $\frac{H}{\sqrt{\kappa}} = 5766$. The thick red solid line connects the maxima of the individual curves and thereby defines $\left(\frac{\delta}{H}\right)_{\text{opt}}$ whose variation with c_ρ is shown in (b). (c) c_p versus $\frac{\delta}{H}$ for the same c_ρ considered in (a). Stars indicate $\left(\frac{\delta}{H}\right)_{\text{opt}}$.

pore space for the liquid to flow as a result of which the maximum mass flow rate is, after a period, realized for smaller $\left(\frac{\delta}{H}\right)_{\text{opt}}$.

2.4.3 The capillary pumping limit

Our analysis has so far assumed that whatever gradients of pressure are necessary to drive the flow of liquid can be accommodated by capillarity. In actuality, there are limits to the difference of liquid pressure that may be experienced between the evaporator- and condenser-ends of the adiabatic section of a heat pipe. These limits are related to the deflection of the liquid-vapor interface, which is, in turn, a function of the surface tension, σ, and the geometric details of the screen type wick. To illustrate this point, consider figure 2.10, which shows a representative axial pressure variation from the evaporator section to the condenser section. For reference, we suppose that $x = 0$ corresponds to the boundary between the condenser and the adiabatic section. At this location, the capillary pressure is given by $\Delta p_{\text{cond}} \equiv p_{v0} - p_{l0}$ where $p_{v0} \equiv p_v(x = 0)$ and $p_{l0} \equiv p_l(x = 0)$. Consistent with the previous discussion, Khrustalev et al. (1994), Zhang et al.

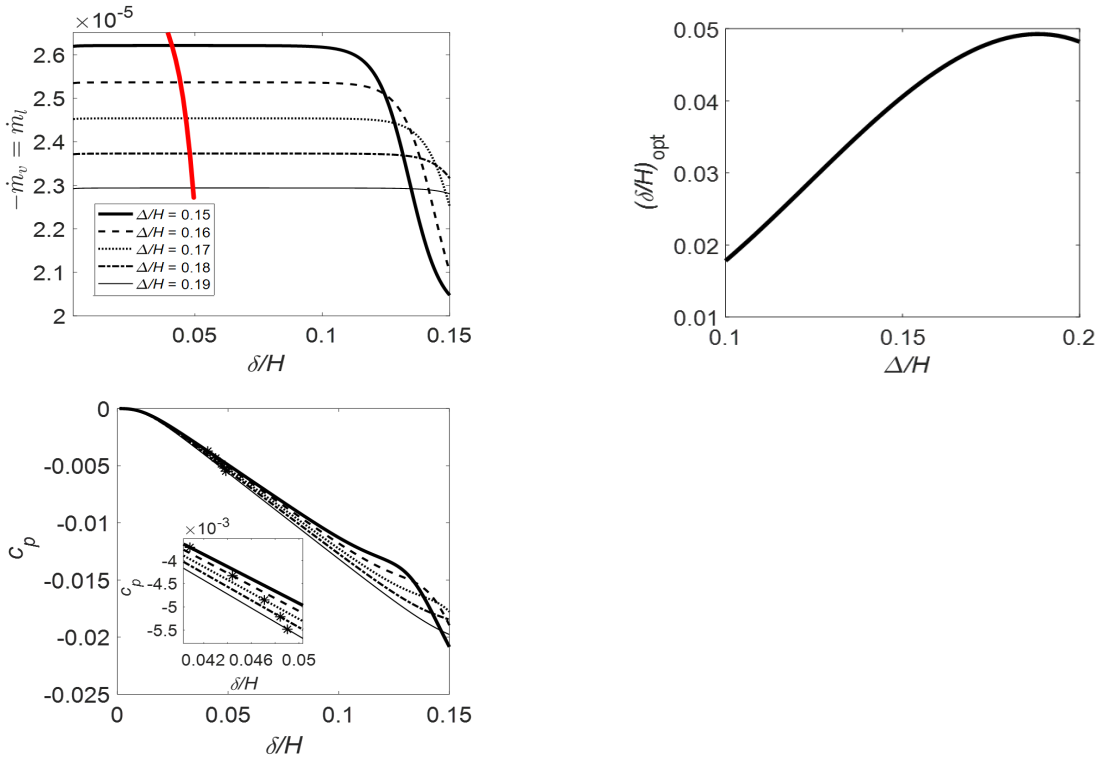

Figure 2.8 – (a) $-\dot{m}_v = \dot{m}_l$ versus $\frac{\delta}{H}$ for various $\frac{\Delta}{H}$ with $c_\rho = 10^{-4}$, $c_\mu = 2\times10^{-2}$, $\varepsilon = 0.9$ and $\frac{H}{\sqrt{\kappa}} = 5766$. The thick red solid line connects the maxima of the individual curves and thereby defines $\left(\frac{\delta}{H}\right)_{\text{opt}}$ whose variation with $\frac{\Delta}{H}$ is shown in (b). (c) c_p versus $\frac{\delta}{H}$ for the same $\frac{\Delta}{H}$ considered in (a). Stars indicate $\left(\frac{\delta}{H}\right)_{\text{opt}}$. In panel (a), note that the vertical axis does not start from zero.

(2007) and Shafahi et al. (2010), we assume, in the adiabatic section, linear variations of pressure in both phases such that $p_v(x=L) = \pi_v L + p_{v0}$ and $p_l(x=L) = \pi_l L + p_{l0} = \pi_l L + p_{v0} - \Delta p_{\text{cond}}$ (recall that $\pi_v < 0$). Here L is the axial length of the adiabatic section as shown in figure 2.10. The capillary pressure at $x = L$ is given by

$$\Delta p_{\text{evap}} = (\pi_v - \pi_l)L + \Delta p_{\text{cond}} \tag{2.37}$$

In order that a stable meniscus form, and with reference to figure 2.11, we require that the meniscus deformation associated with Δp_{evap} satisfy $R_{\text{evap}} \geq R_{\text{evap,min}}$. Here $R_{\text{evap}} = \sigma/\Delta p_{\text{evap}}$ is the meniscus radius of curvature measured at $x = L$ whose minimum possible value is given by the solution of

$$4R_{\text{evap,min}}^2 + 4R_{\text{evap,min}} D\cos\theta + D^2 = \beta^2 \tag{2.38}$$

where θ is the contact angle, β is the center-to-center distance between adjacent wires comprising the porous medium and D is the wire diameter. Note that $R_{\text{evap,min}}$ is associated with the maximum

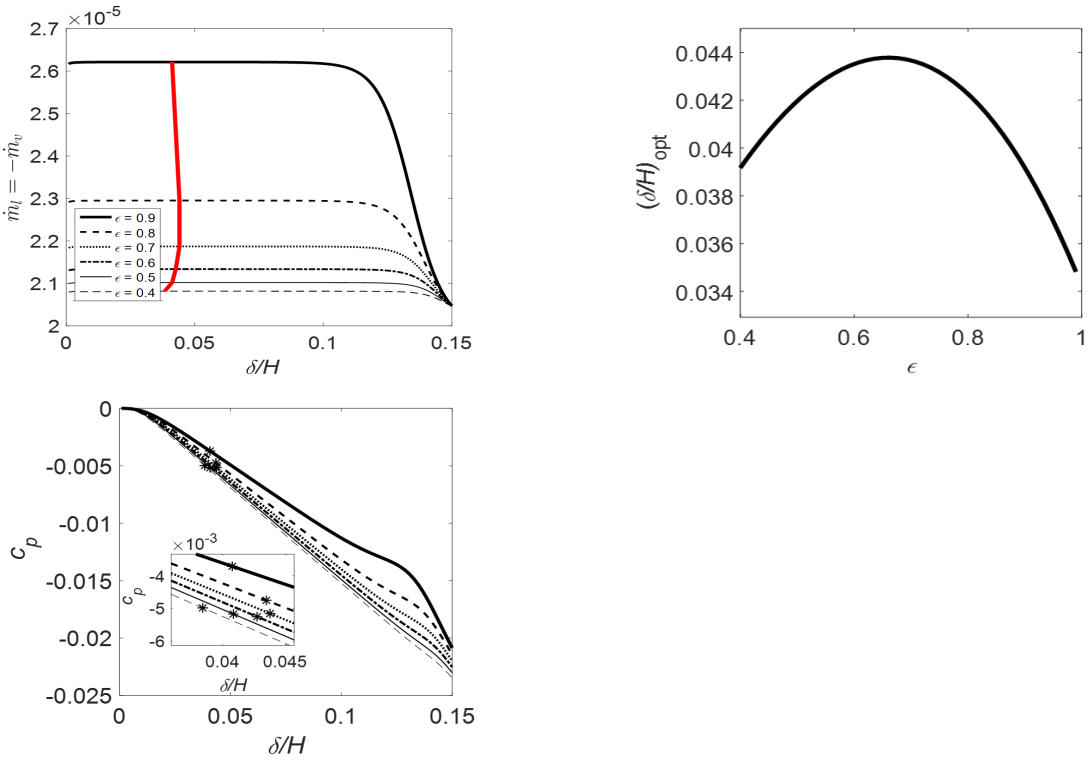

Figure 2.9 – (a) $-\dot{m}_v = \dot{m}_l$ versus $\frac{\delta}{H}$ for various ε with $c_\rho = 10^{-4}$, $c_\mu = 2\times10^{-2}$, $\frac{\Delta}{H} = 0.15$ and $\frac{H}{\sqrt{\kappa}} = 5766$. The thick red solid line connects the maxima of the individual curves and thereby defines $\left(\frac{\delta}{H}\right)_{\text{opt}}$ whose variation with ε is shown in (b). (c) c_p versus $\frac{\delta}{H}$ for the same ε considered in (a). Stars indicate $\left(\frac{\delta}{H}\right)_{\text{opt}}$. In panel (a), note that the vertical axis does not start from zero.

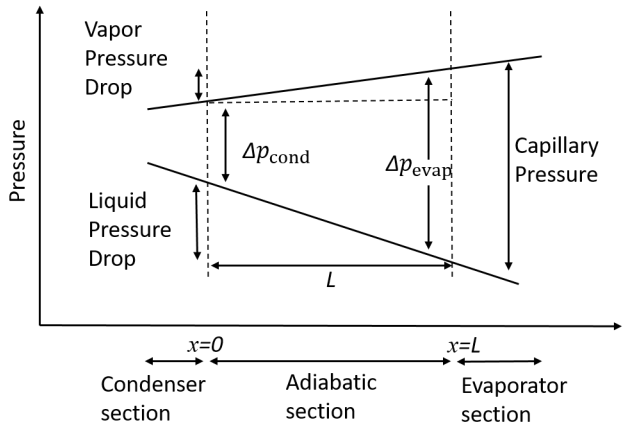

Figure 2.10 – Axial pressure variation for the liquid and vapor phases. The vapor pressure drops from the evaporator to the condenser and the liquid pressure drops from condenser to evaporator.

possible pressure drop, $\Delta p_{\text{evap,max}}$, measured at $x = L$. Note, furthermore, that R_{evap} can be related to the geometric details of the wires comprising the wick by adapting the analysis of Flynn & Bush

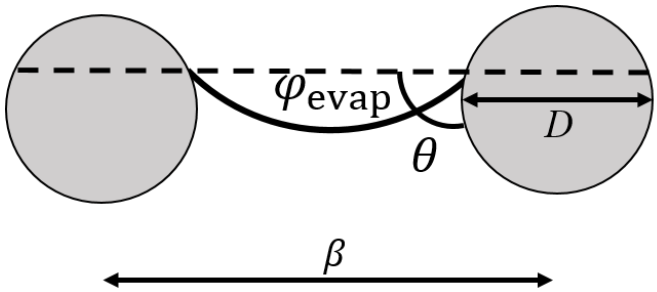

Figure 2.11 – Geometry of the meniscus at the adiabatic-evaporator end.

(2008), i.e.

$$R_{evap} = \frac{\beta}{2\sin\phi_{evap}}\left[1 - \frac{D}{\beta}\sin\left(\theta + \phi_{evap}\right)\right] \tag{2.39}$$

where, consistent with figure 2.11, ϕ_{evap} is defined as the angle that the meniscus makes with the horizontal.

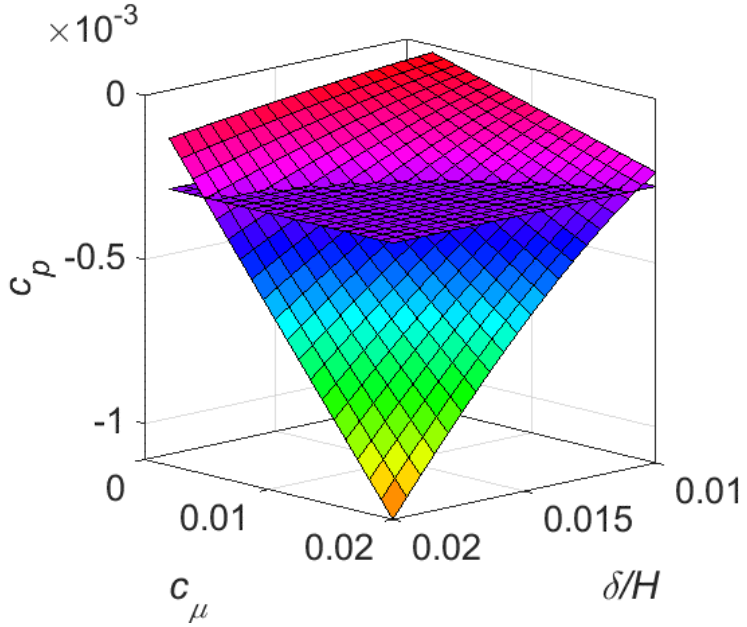

Figure 2.12 – The pressure gradient ratio, c_p, as determined from (2.36) versus c_μ and $\frac{\delta}{H}$ with $c_\rho = 10^{-4}$, $\frac{\Delta}{H} = 0.15$, $\varepsilon = 0.9$, $\frac{H}{\sqrt{\kappa}} = 5766$. The curved surface shows the limiting value prescribed by (2.36) and the flat surface shows the solution of (2.44) where we have assumed $\theta = 0°$, $\Sigma = 1015$ and $\frac{\Delta p_{cond}}{\pi_v L} = 3043$. Physically-admissible solutions are those located below the intersection of the two surfaces.

Ostensibly, (2.38)-(2.39) introduce two new geometric variables, β and D. However, β and D can be related to other, previously defined variables such as ε and κ using the Kozeny-Carman

equation (Peterson 1994) and the geometric expression for porosity, i.e.

$$\beta = \sqrt{\frac{\pi\kappa\Upsilon}{4}\left(\frac{1-\varepsilon}{\varepsilon^3}\right)}, \qquad D = (1-\varepsilon)\sqrt{\frac{\kappa\Upsilon}{\varepsilon^3}} \tag{2.40}$$

Here Υ is an $\mathscr{O}(10^2)$ constant that is here taken to be 100 for simplicity (Zohuri 2011).

On the basis of the above analysis, it can be shown that the maximum possible value for the liquid-vapor pressure difference at $x = L$ which is realized when ϕ achieves its maximum value, is given by

$$\frac{\Delta p_{\text{evap,max}}}{\pi_v L} = \frac{-2\Sigma\varepsilon^{3/2}\sin\phi_{\text{evap,max}}}{2(1-\varepsilon)\sin\left(\phi_{\text{evap,max}}+\theta\right) - \sqrt{\pi(1-\varepsilon)}} \tag{2.41}$$

where the non-dimensional surface tension is given by

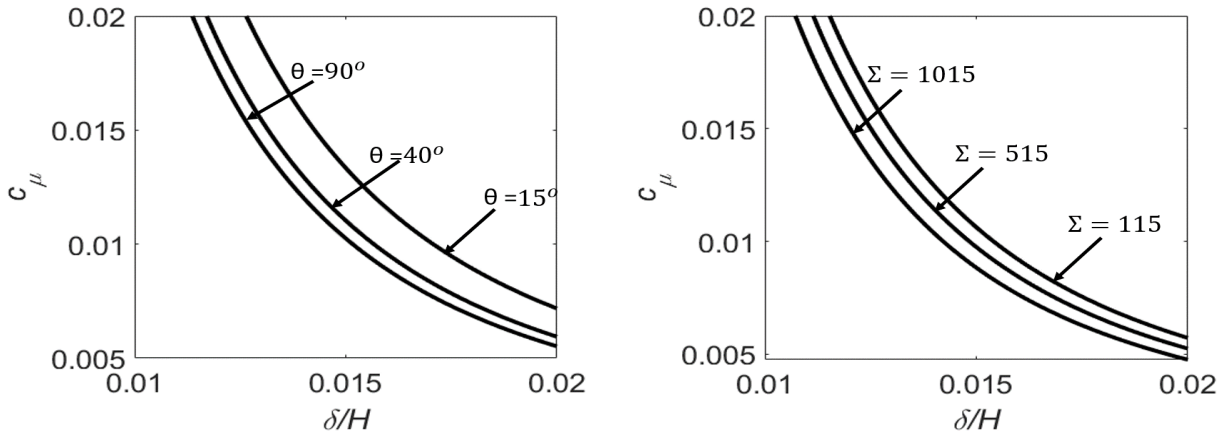

Figure 2.13 – (a) Regime diagram showing the solution space for various θ with $c_\rho = 10^{-4}$, $\frac{\Delta}{H} = 0.15$, $\varepsilon = 0.9$, $\frac{H}{\sqrt{\kappa}} = 5766$, $\Sigma = 1015$ and $\frac{\Delta p_{\text{cond}}}{\pi_v L} = 3043$. Physically-admissible solutions are those located above each curve. (b) As in panel (a) but considering the influence of Σ with $\theta = 90^\circ$.

$$\Sigma = \frac{2\sigma}{|\pi_v| L\sqrt{\kappa\Upsilon}} \tag{2.42}$$

and $\phi_{\text{evap,max}}$ can be obtained by combining (2.38) and (2.39). Finally, substituting (2.41) into (2.37) yields, after non-dimensionalizing,

$$c_p \leq \left[1 + \frac{\Delta p_{\text{cond}}}{\pi_v L} + \frac{2\Sigma\varepsilon^{3/2}\sin\phi_{\text{evap,max}}}{2(1-\varepsilon)\sin\left(\phi_{\text{evap,max}}+\theta\right) - \sqrt{\pi(1-\varepsilon)}}\right]^{-1} \tag{2.43}$$

For fixed σ, (2.43) prescribes the largest possible ratio of pressure gradients that will facilitate capillary pumping. For the special case when $\theta = 0^\circ$, the wick is perfectly hydrophilic, the minimum value for R_{evap} prescribed by (2.38) is $R_{\text{evap,min}} = \frac{1}{2}(\beta - D)$ and, from (2.39), we determine that $\phi_{\text{evap,max}} = 90^\circ$. In this circumstance, (2.43) can be simplified to

$$c_p \leq \left(1 + \frac{\Delta p_{\text{cond}}}{\pi_v L} + \frac{\Sigma \varepsilon^{\frac{3}{2}}}{1 - \varepsilon - \frac{1}{2}\sqrt{\pi(1-\varepsilon)}} \right)^{-1} \tag{2.44}$$

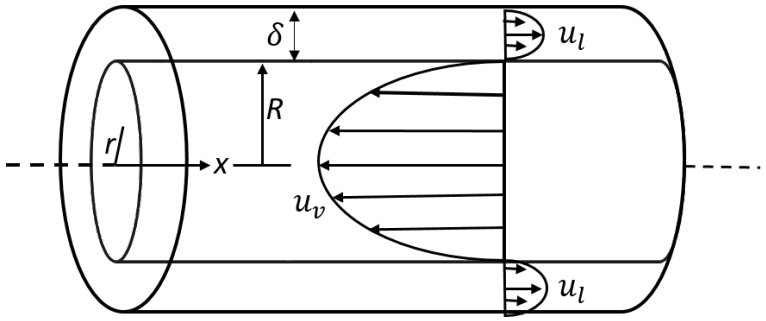

Figure 2.14 – Axisymmetric flow in a heat pipe, devoid of a wick.

Similar to figure 2.2, a surface plot showing the variation of c_p with respect to $\frac{\delta}{H}$ and c_μ is presented in figure 2.12. Also included in this figure is a horizontal plane corresponding to the $\theta = 0^\circ$ limit for c_p prescribed by (2.44) where we have selected $\frac{\Delta p_{\text{cond}}}{\pi_v L} = 3043$ and $\Sigma = 1015$ (Shafahi et al. 2010, Zhu & Vafai. 1999). Physically-acceptable solutions arise only below the intersection of the two surfaces exhibited in figure 2.12.

Figure 2.12 highlights the importance of the limiting curve corresponding to the intersection of the surfaces derived from the solutions to (2.36) and (2.44). Examples of such limiting curves are shown for different values of θ and Σ in figures 2.13 a,b, respectively. Physically-admissible combinations of c_μ and δ/H appear strictly above each of the curves in question. Thus the solution space broadens with increasing Σ: larger Σ is associated with larger surface tension and this is obviously advantageous for flows that are driven by capillarity. In a similar vein, larger values of the contact angle are more straightforward to accommodate given the meniscus/wire geometries exhibited schematically in figure 2.11. Hence, the solution space broadens with increasing θ.

2.5 Axisymmetric flow, no wick

Whereas the planar geometry case covered in sections 2 and 3 admits relatively straightforward solutions, it must be acknowledged that virtually all heat pipes are constructed with a cylindrical

geometry. As such, and for the remainder of our manuscript, we shall consider the case of an axisymmetric flow. Here, similar to section 2, we ignore the complication of an interior wick. In section 5, this simplification is relaxed and we pursue an analysis similar to that just completed in section 3.

2.5.1 Governing equations

With reference to the schematic of figure 2.14, the governing equations now read as follows:

$$\frac{\mu_v}{r}\frac{d}{dr}\left(r\frac{du_v}{dr}\right) = \frac{dp_v}{dx} \equiv \pi_v < 0 \tag{2.45}$$

$$\frac{\mu_l}{r}\frac{d}{dr}\left(r\frac{du_l}{dr}\right) = \frac{dp_l}{dx} \equiv \pi_l > 0 \tag{2.46}$$

Here, obviously, we have assumed axisymmetric Poiseuille flow devoid of swirl. The standard no-slip boundary condition is applied at the interior wall, $r = R$, and a symmetrical boundary condition is applied along the pipe axis $r = 0$. Along the interface between liquid and vapor, the velocity and shear stress must be continuous. In solving (2.45) and (2.46), a global mass balance equation must again be satisfied by which

$$-\dot{m}_v = \dot{m}_l \qquad \text{where} \qquad \dot{m}_v = \rho_v \int_0^{R-\delta} u_v r dr \tag{2.47}$$

$$\text{and} \qquad \dot{m}_l = \rho_l \int_{R-\delta}^{R} u_l r dr$$

and factors of 2π have been omitted for algebraic convenience. The equations given above are non-dimensionlized using R, μ_v and π_v. Thus, we define

$$r^* = \frac{r}{R}, \qquad u_v^* = \frac{\mu_v}{R^2\pi_v}u_v \qquad \text{and} \qquad u_l^* = \frac{\mu_v}{R^2\pi_v}u_l$$

and we find that

$$\frac{1}{r^*}\frac{d}{dr^*}\left(r^*\frac{du_v^*}{dr^*}\right) = 1 \tag{2.48}$$

$$\frac{1}{r^*}\frac{d}{dr^*}\left(r^*\frac{du_l^*}{dr^*}\right) = \frac{c_\mu}{c_p} \tag{2.49}$$

with corresponding boundary conditions

$$u_l^*(r^* = 1) = 0 \tag{2.50}$$

$$\left(\frac{du_v^*}{dr^*}\right)_{r^*=0} = 0 \tag{2.51}$$

$$u_v^*\left(r^* = 1 - \frac{\delta}{R}\right) = u_l^*\left(r^* = 1 - \frac{\delta}{R}\right) \tag{2.52}$$

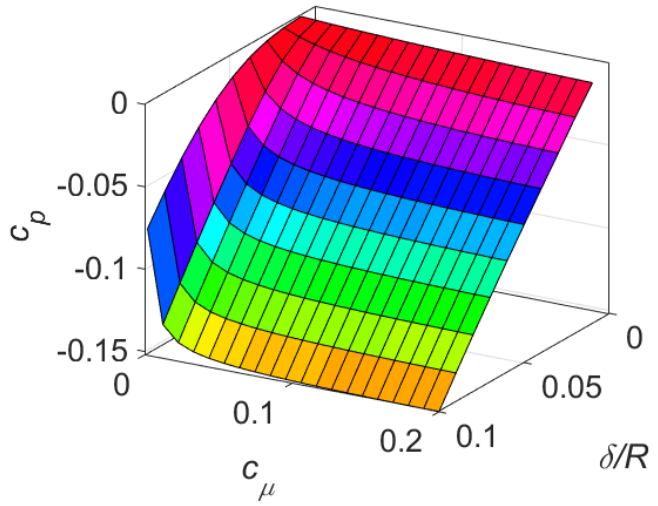

Figure 2.15 – The pressure gradient ratio, c_p, as determined from (2.57) versus c_μ and $\frac{\delta}{R}$ with $c_\rho = 10^{-4}$.

$$c_\mu \left(\frac{du_v^*}{dr^*}\right)_{r^*=1-\frac{\delta}{R}} = \left(\frac{du_l^*}{dr^*}\right)_{r^*=1-\frac{\delta}{R}} \tag{2.53}$$

Solutions to (2.48) and (2.49) respectively read as follows:

$$u_v^* = \frac{r^{*2}}{4} + b \tag{2.54}$$

$$u_l^* = \frac{r^{*2}}{4} + a' \ln r^* + b' \tag{2.55}$$

The constants b, a' and b' can be determined using (2.50-2.53).

2.5.2 Evaluation of c_p and determination of the optimum liquid layer thickness

Equations (2.54) and (2.55) are incomplete because they rely on c_p whose value is determined from (2.47). Expressing (2.47) using non-dimensional variables, we require that

$$c_\rho \int_0^{1-\frac{\delta}{R}} u_v^* r^* dr^* + \int_{1-\frac{\delta}{R}}^1 u_l^* r^* dr^* = 0 \tag{2.56}$$

Applying (2.54) and (2.55) in (2.56) yields, after some algebra, the following solution for c_p in terms of c_μ, c_ρ and δ/R:

$$c_p = \frac{\mathscr{N}}{\mathscr{D}} \tag{2.57}$$

where

$$\mathscr{N} = 4c_\mu \left[\left(1-\frac{\delta}{R}\right)^4 (c_\rho - 1) \ln\left(1-\frac{\delta}{R}\right) + \frac{1}{2}\left[(3-2c_\rho)\frac{\delta}{R}^2 + (3-2c_\rho)\frac{\delta}{R} + c_\rho - 1 \right] \frac{\delta}{R}\left(2-\frac{\delta}{R}\right) \right]$$

and

$$\mathscr{D} = 4\left[1-\frac{\delta}{R}\right]^2 \left[c_\mu \left(1-\frac{\delta}{R}\right)^2 (c_\rho - 1) \ln\left(1-\frac{\delta}{R}\right) + \frac{1}{2}\left(c_\mu - \frac{c_\rho}{2}\right)\left(\frac{\delta}{R}\right)^2 + \left(\frac{c_\rho}{2} - c_\mu\right)\frac{\delta}{R} - \frac{c_\rho}{4} \right]$$

Figure 2.15 shows c_p versus $\frac{\delta}{R}$ and c_μ for fixed c_ρ. Similar trends arise as in the rectilinear case

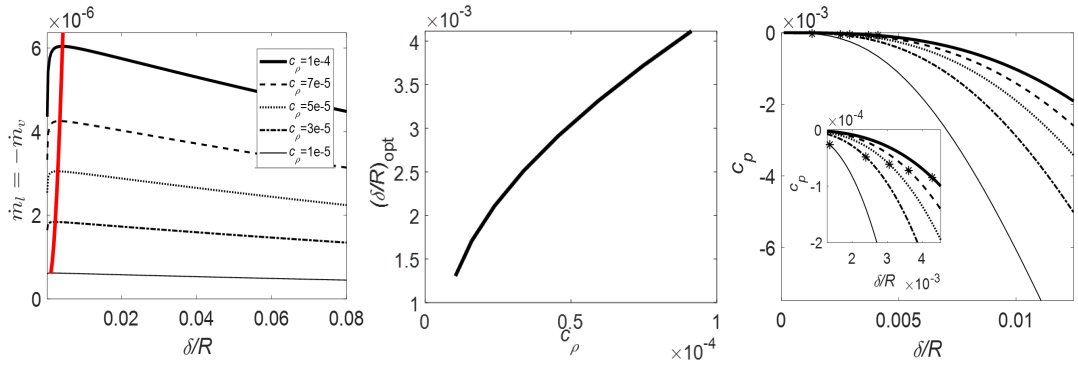

Figure 2.16 – (a) $-\dot{m}_v = \dot{m}_l$ versus $\frac{\delta}{R}$ for various c_ρ with $c_\mu = 2\times10^{-2}$. The thick red solid line connects the maxima of the individual curves and thereby defines $\left(\frac{\delta}{R}\right)_{\text{opt}}$ whose variation with c_ρ is shown in (b). (c) c_p versus $\frac{\delta}{R}$ for the same c_ρ considered in (a). Stars indicate $\left(\frac{\delta}{R}\right)_{\text{opt}}$

.

examined in figure 2.2. Once c_p is known, liquid and vapor velocity profiles may be computed from (2.12) and (2.13). The velocity profiles obtained for an axisymmetric geometry are similar to the velocity profiles for planar geometry and therefore not shown here. Figure 2.16 a confirms that the mass flow rate, $-\dot{m}_v = \dot{m}_l$, exhibits a qualitatively similar variation with the liquid layer thickness as exhibited in figure 2.4 a. In turn, the variation of $\left(\frac{\delta}{R}\right)_{\text{opt}}$ with c_ρ is exhibited in figure 2.16 b and the variation of c_p with $\frac{\delta}{R}$ is exhibited in figure 2.16 c.

2.6 Axisymmetric geometry, wick

We turn finally to the case of an axisymmetric geometry containing a screen-type wick. Figure 2.17 shows the cross-sectional profile relevant to this problem.

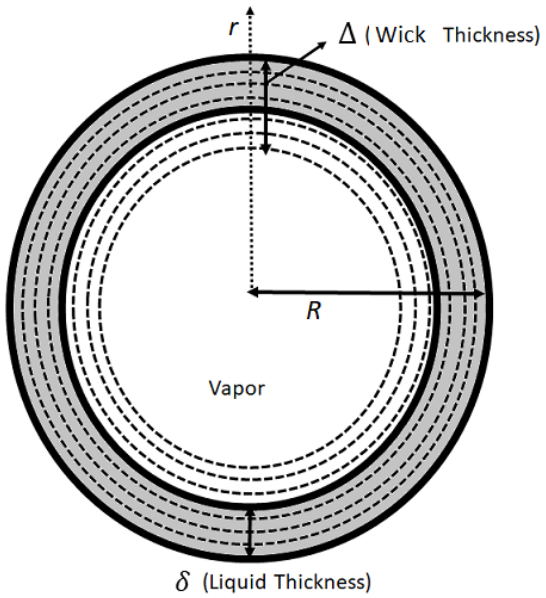

Figure 2.17 – Cross-sectional view of a cylindrical heat pipe containing a peripheral wick of thickness Δ inside of which is a liquid layer of thickness δ.

2.6.1 Governing equations and boundary conditions

Considering the vapor and liquid flow through the wick, (2.16) and (2.17) must now be replaced with their axisymmetric counterparts, i.e.

$$\frac{\mu_v}{\varepsilon}\frac{1}{r}\frac{d}{dr}\left(r\frac{dU_v}{dr}\right)-\frac{\mu_v}{\kappa}U_v=\frac{dp_v}{dx}\equiv\pi_v<0 \tag{2.58}$$

$$\frac{\mu_l}{\varepsilon}\frac{1}{r}\frac{d}{dr}\left(r\frac{dU_l}{dr}\right)-\frac{\mu_l}{\kappa}U_l=\frac{dp_l}{dx}\equiv\pi_l>0 \tag{2.59}$$

where, as before, velocities represented by an upper-case letter are measured inside the wick. Equations (2.58-2.59) are to be solved in conjunction with (2.45) subject to the following boundary conditions:

$$U_v(r=R-\Delta)=u_v(r=R-\Delta) \tag{2.60}$$

$$\left(\frac{dU_v}{dr}\right)_{r=R-\Delta}-\varepsilon\left(\frac{du_v}{dr}\right)_{r=R-\Delta}-\frac{\alpha\varepsilon}{\sqrt{\kappa}}U_v(r=R-\Delta)=0 \tag{2.61}$$

$$U_v(r=R-\delta)=U_l(r=R-\delta) \tag{2.62}$$

$$c_\mu \left(\frac{dU_v}{dr}\right)_{r=R-\delta} = \left(\frac{dU_l}{dr}\right)_{r=R-\delta} \tag{2.63}$$

$$U_l(r=R) = 0 \tag{2.64}$$

The above equations may be non-dimentionalized using a similar procedure to section (2.1). Thus we define

$$u_v^* = \left(\frac{\mu_v}{R^2\pi_v}\right) u_v, \qquad u_l^* = \left(\frac{\mu_v}{R^2\pi_v}\right) u_l,$$
$$U_v^* = \left(\frac{\mu_v}{R^2\pi_v}\right) U_v, \qquad U_l^* = \left(\frac{\mu_v}{R^2\pi_v}\right) U_l$$

and $r^* = \frac{r}{R}$. The governing equations therefore consist of (2.48) plus

$$r^{*2}\frac{d^2U_{v^*}}{dr^{*2}} + r^*\frac{dU_v^*}{dr^*} - \frac{\varepsilon R^2}{\kappa} r^{*2} U_v^* = r^{*2} \tag{2.65}$$

$$r^{*2}\frac{d^2U_l^*}{dr^{*2}} + r^*\frac{dU_l^*}{dr^*} - \frac{\varepsilon R^2}{\kappa} r^{*2} U_l^* = \frac{c_\mu}{c_p} r^{*2} \tag{2.66}$$

Analogously, the boundary conditions may be rewritten as

$$U_v^*\left(r^* = 1 - \frac{\Delta}{R}\right) = u_v^*\left(r^* = 1 - \frac{\Delta}{R}\right) \tag{2.67}$$

$$\left(\frac{dU_v^*}{dr^*}\right)_{r^*=1-\frac{\Delta}{R}} - \varepsilon\left(\frac{du_v^*}{dr^*}\right)_{r^*=1-\frac{\Delta}{R}} - \alpha\varepsilon\frac{R}{\sqrt{\kappa}} U_v^*\left(r^* = 1 - \frac{\Delta}{R}\right) = 0 \tag{2.68}$$

$$U_v^*\left(r^* = 1 - \frac{\delta}{R}\right) = U_l^*\left(r^* = 1 - \frac{\delta}{R}\right) \tag{2.69}$$

$$c_\mu \left(\frac{dU_v^*}{dr}\right)_{r^*=1-\frac{\delta}{R}} = \left(\frac{dU_l^*}{dr}\right)_{r^*=1-\frac{\delta}{R}} \tag{2.70}$$

$$U_l^*\left(r^* = 1\right) = 0 \tag{2.71}$$

The general solution for u_v is given by (2.54). Meanwhile, the general solutions to (2.65) and (2.66) involve modified Bessel functions, i.e.

$$U_v^* = AI_0\left(r^*\sqrt{\frac{\varepsilon R^2}{\kappa}}\right) + BK_0\left(r^*\sqrt{\frac{\varepsilon R^2}{\kappa}}\right) - \left(\frac{\varepsilon R^2}{\kappa}\right)^{-1} \tag{2.72}$$

$$U_l^* = A'I_0\left(r^*\sqrt{\frac{\varepsilon R^2}{\kappa}}\right) + B'K_0\left(r^*\sqrt{\frac{\varepsilon R^2}{\kappa}}\right) - \frac{c_\mu}{c_p}\left(\frac{\varepsilon R^2}{\kappa}\right)^{-1} \tag{2.73}$$

The constants b, A, B, A' and B' are evaluated using (2.67-2.71). Similar to before, the model is closed, and the value of c_p determined, by enforcing

$$0 = c_\rho \left[\int_0^{1-\frac{\Delta}{R}} u_v^* r^* dr^* + \int_{1-\frac{\Delta}{R}}^{1-\frac{\delta}{R}} U_v^* r^* dr^* \right] + \int_{1-\frac{\delta}{R}}^{1} U_l^* r^* dz^* \tag{2.74}$$

Moreover, the list of key independent variables now reads as follows: c_μ, c_ρ, $\frac{\delta}{R}$, $\frac{\Delta}{R}$, $\frac{R}{\sqrt{\kappa}}$ and ε. Solving the above equations yields velocity profiles (not shown) that are qualitatively similar to those of figure 2.6.

2.6.2 Optimum liquid layer thickness

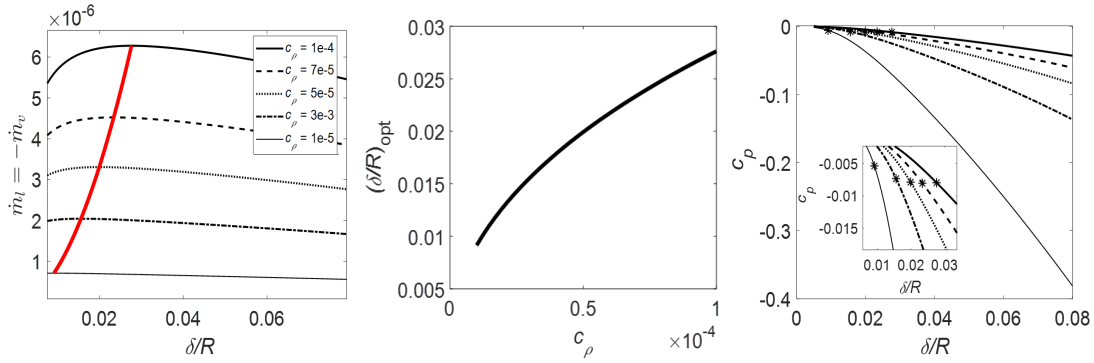

Figure 2.18 – (a) $-\dot{m}_v = \dot{m}_l$ versus $\frac{\delta}{H}$ for various c_ρ with $c_\mu = 2 \times 10^{-2}$, $\frac{\Delta}{R} = 0.15$, $\varepsilon = 0.9$ and $\frac{R}{\sqrt{\kappa}} = 5766$. The thick red solid line connects the maxima of the individual curves and thereby defines $\left(\frac{\delta}{R}\right)_{\text{opt}}$ whose variation with c_ρ is shown in (b). (c) c_p versus $\frac{\delta}{R}$ for the same c_ρ considered in (a). Stars indicate $\left(\frac{\delta}{R}\right)_{\text{opt}}$.

As with the analysis performed in sections 2.3.3, 2.4.2 and 2.5.2, we wish to estimate the optimum liquid layer thickness, $\left(\frac{\delta}{R}\right)_{\text{opt}}$ whereby the axial transport of mass (and heat) is maximized. Consistent with figure 2.16 a, figure 2.18 a shows the variation of $-\dot{m}_v = \dot{m}_l$ with the liquid layer thickness for different c_ρ. As before, we note that $\left(\frac{\delta}{R}\right)_{\text{opt}}$ increases with the density ratio, a fact also made clear in figure 2.18 b. However, we observe in figure 2.18 b larger values for $\left(\frac{\delta}{R}\right)_{\text{opt}}$ than in figure 2.16 b, this a consequence of restricting the liquid flow to occur only within the wick. Figure 2.18 c is analogous to figure 2.16 c and shows c_p versus $\frac{\delta}{R}$ for different c_ρ where the stars indicate the optimum liquid layer thickness as determined from figure 2.18 b. Figures 2.19 and 2.20 are similar to figure 2.18, but consider the variation of $-\dot{m}_v = \dot{m}_l$ with $\frac{\delta}{R}$ for various $\frac{\Delta}{R}$ and ε, respectively.

A unifying characteristic of figures 2.18 a, 2.19 a and 2.20 a that sets them apart from figures 2.7 a, 2.8 a and 2.9 a, respectively, is the appearance of distinct maxima that arise for well-defined values of the liquid layer thickness. Note also that the curves of 2.18 b, 2.19 b, which respectively

show the variation of $\left(\frac{\delta}{R}\right)_{\text{opt}}$ with c_ρ and Δ/R are monotone. By contrast, and consistent with the discussion of section II C, the curve of figure 2.20 b exhibits non-monotone behavior.

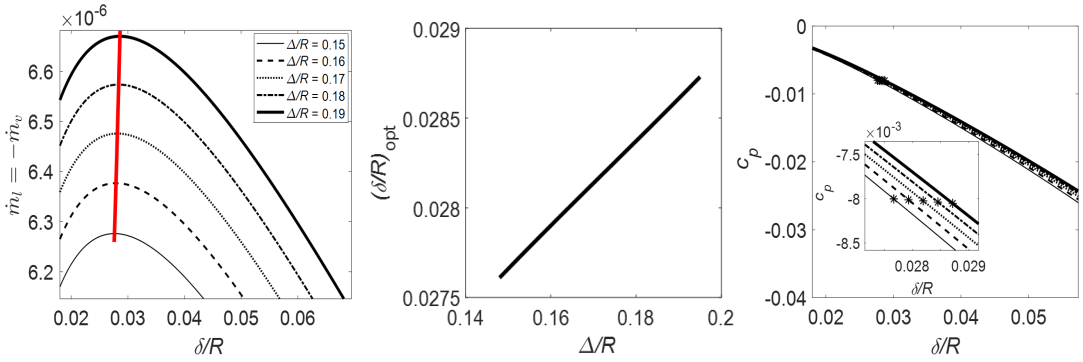

Figure 2.19 – (a) $-\dot{m}_v = \dot{m}_l$ versus $\frac{\delta}{R}$ for various $\frac{\Delta}{R}$ with $c_\rho = 10^{-4}$, $c_\mu = 2 \times 10^{-2}$, $\varepsilon = 0.9$ and $\frac{R}{\sqrt{\kappa}} = 5766$. The thick red solid line connects the maxima of the individual curves and thereby defines $\left(\frac{\delta}{R}\right)_{\text{opt}}$ whose variation with $\frac{\Delta}{R}$ is shown in (b). (c) c_p versus $\frac{\delta}{R}$ for the same $\frac{\Delta}{R}$ considered in (a). Stars indicate $\left(\frac{\delta}{R}\right)_{\text{opt}}$.

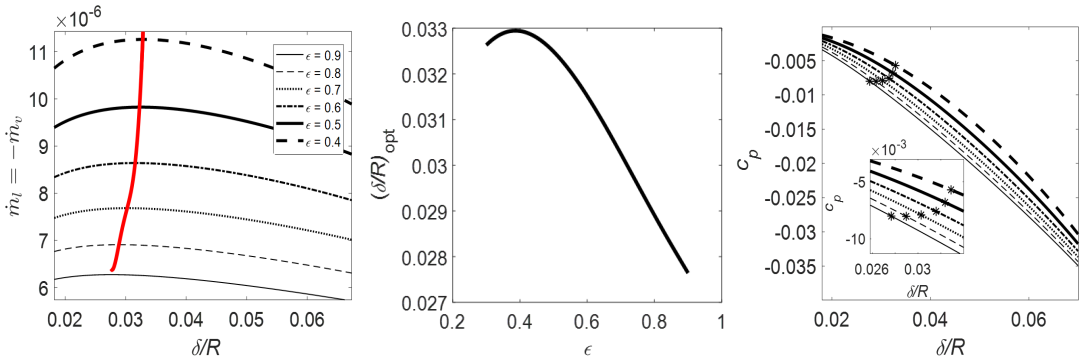

Figure 2.20 – (a) $-\dot{m}_v = \dot{m}_l$ versus $\frac{\delta}{R}$ for various ε with $c_\rho = 10^{-4}$, $c_\mu = 2 \times 10^{-2}$, $\frac{\Delta}{R} = 0.15$ and $\frac{R}{\sqrt{\kappa}} = 5766$. The thick red solid line connects the maxima of the individual curves and thereby defines $\left(\frac{\delta}{R}\right)_{\text{opt}}$ whose variation with ε is shown in (b). (c) c_p versus $\frac{\delta}{R}$ for the same ε considered in (a). Stars indicate $\left(\frac{\delta}{R}\right)_{\text{opt}}$.

2.6.3 The capillary pumping limit

Similar to figure 2.12 for the case of a planar heat pipe with a wick, a surface plot showing the variation of c_p with respect to $\frac{\delta}{R}$ and c_μ is presented in figure 2.21. Also included is a horizontal plane which considers the limit for c_p given by (2.44). The analogue to figure 2.13 a,b is figure 2.22 a,b. It shows, on the basis of the intersection of surfaces such as those from figure 2.21, the range of c_μ and $\frac{\delta}{R}$ that are conducive to capillary pumping.

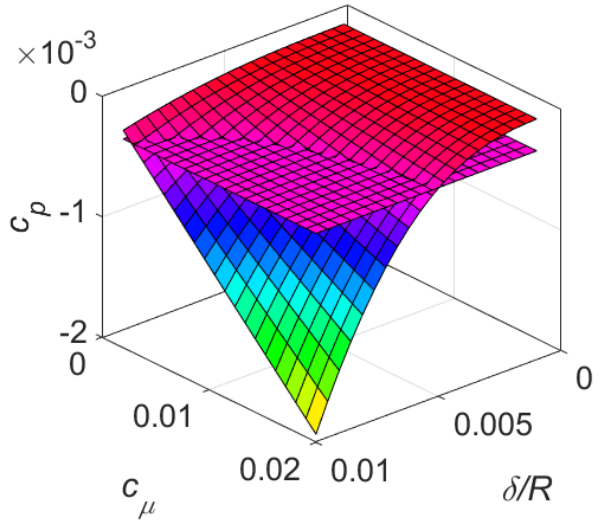

Figure 2.21 – The pressure gradient ratio, c_p, as determined from (2.74) versus c_μ and $\frac{\delta}{R}$ with $c_\rho = 10^{-4}$, $\frac{\Delta}{R} = 0.15$, $\varepsilon = 0.9$, $\frac{R}{\sqrt{\kappa}} = 5766$. The curved surface shows the limiting value prescribed by (2.74) and the flat surface shows the limiting value prescribed by (2.44) where we have assumed $\theta = 0^\circ$, $\Sigma = 1015$ and $\frac{\Delta p_{\text{cond}}}{\pi_v L} = 3043$. Physically-admissible solutions are those located below the intersection of the two surfaces.

2.6.4 Comparison with the results of Zhu & Vafai (1999) and Shafahi et al. (2010)

The axisymmetric geometry considered in section V.A provides the most straightforward opportunity for comparing the predictions of our model with related results reported in the literature. To this end, we pay particular attention to the investigations conducted by Zhu & Vafai (1999) and Shafahi et al. (2010). Focusing first of all on the latter study, their figure 3 indicates a predicted pressure gradient ratio of $c_p = -0.0011$ for a heat pipe characterized by a flooded wick having a permeability of $\kappa = 1.5 \times 10^{-9}\,\text{m}^2$. Adopting this value here (as compared to the more permeable wick implicitly considered in figures 2.6-2.9, 2.12, 2.13 and 2.18-2.22) and matching other independent parameters besides, we predict a pressure gradient ratio of similar scale, i.e. $c_p = -0.0012$.

The comparison with the earlier results of Zhu & Vafai (1999) is somewhat more involved as it requires an estimation of the maximum possible heat flux as calculated in the capillary limit where $R_{\text{evap}} = R_{\text{evap,min}}$ (and, with reference to equation (2.38), $\theta = 0^\circ$). Zhu & Vafai's analytical model is predicated on some different assumptions than we consider here. For instance, they solve the liquid flow problem using a generalized momentum equation (Vafai et al. 1981) that includes a Forchheimer term. As a result, the capillary limit is realized at a different wick permeability in Zhu & Vafai's model vs. our own. All other parameters are the same and we therefore consider $\varepsilon = 0.9$, $\delta/R = \Delta/R = 0.08$, where the heat pipe inner radius measures $R = 9.4\,\text{mm}$. In turn, we

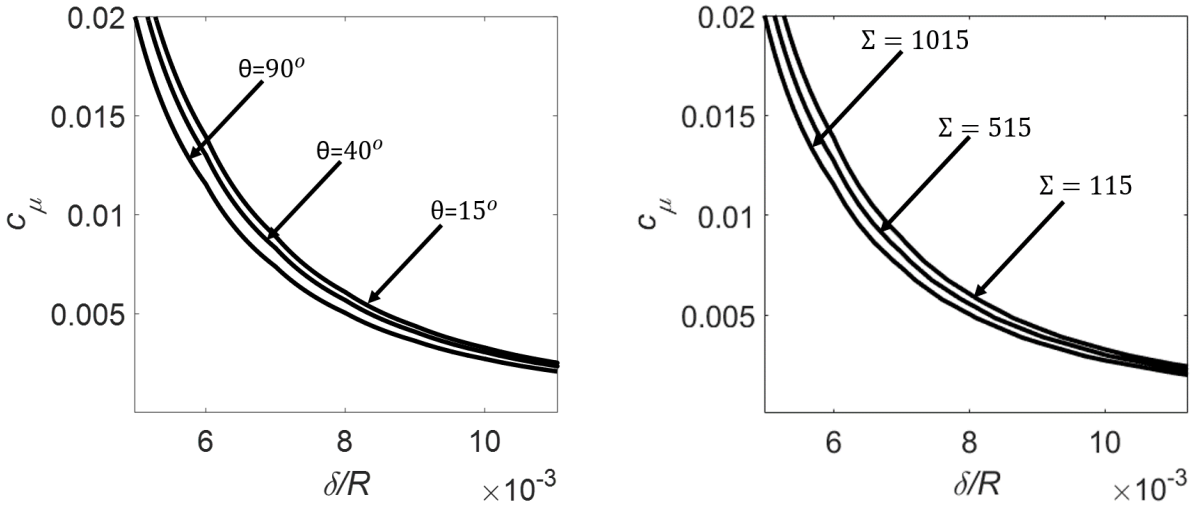

Figure 2.22 – (a) Regime diagram showing the solution space for various θ with $c_\rho = 10^{-4}$, $\frac{\Delta}{R} = 0.15$, $\varepsilon = 0.9$, $\frac{R}{\sqrt{\kappa}} = 5766$, $\Sigma = 1015$ and $\frac{\Delta p_{\text{cond}}}{\pi_v L} = 3043$. Physically-admissible solutions are those located above each curve. (b) As in panel (a) but considering the influence of Σ with $\theta = 90°$.

suppose a heat pipe operating temperature of 63°C and a liquid pressure gradient of |1000|Pa/m. With the above variables to hand, our model predicts a maximum heat flux of 1.35 kW. This value compares favorably to the corresponding value of 1.30 kW recovered from the complete model curve of figure 9 of Zhu & Vafai (1999).

Although it would obviously be helpful to expand upon the comparison between our model predictions vs. those reported by other researchers, the relatively close agreements reported above are encouraging. They suggest that the modeling approach adopted here is not unreasonable even though we have focused our attention solely on the heat pipe adiabatic section.

2.7 Conclusions

In this work, we have adapted core annular flow theory to describe the anti-parallel flow of liquid and vapor that arises, for instance, inside of a heat pipe. Key to our analysis is to enforce a mass balance by which $-\dot{m}_v = \dot{m}_l$, which applies once steady conditions are realized. The mass balance requirement imposes a restriction on the vapor-to-liquid pressure gradient ratio, whose value, determined from equations like (2.14) or (2.56), depends on the density and viscosity ratios.

Broadly speaking, our work is motivated by Busse et al. (2013) who studied internal flows lubricated by a surface-attached air bubble or plastron. Busse et al. (2013) developed an expression for the drag-minimizing plastron thickness. Our interest concerns not drag minimization per se but rather a maximization of the axial flow of mass (and, in the heat pipe context, of heat). To this

end, and for the flows illustrated schematically in figures 2.1, 2.5, 2.14 and 2.17, we determine the optimal liquid layer thickness as a function of the vapor-to-liquid density ratio and, where, applicable, the depth and porosity of the porous media constituting the peripheral wick. Calculations are performed for four configurations: planar, no wick (section II); planar, with wick (section III); axisymmetric, no wick (section IV); axisymmetric, with wick (section V). Not surprisingly, the optimal liquid layer thickness runs larger in cases with a wick where the liquid flow is more constrained. Of course, when the liquid flow (and part of the vapor flow) is through a wick, additional variables are important to the flow dynamics e.g. the wick permeability, porosity and thickness. Such considerations were avoided in McHale et al. (2011) and Busse et al. (2013) because they considered an idealized plastron layer i.e. one supported along the solid surface without benefit of a porous medium or network of hydrophobic structures.

Finally, we perform an analysis to find the minimum pressure gradient ratio required to support the capillary pumping of liquid from the condenser to the evaporator see – eg. (2.43) and (2.44). The analysis in question employs the Young-Laplace equation at the scale of the wick microstructure and considers, therefore, the diameter of, and spacing between, the wires that comprise the (screen-type) wick. Equations (2.43) and (2.44), which define the limiting pressure gradient ratio as a function of the contact angle, θ, and the surface tension, σ, are therefore applicable to both of the planar and cylindrical geometries. In either case, we find that increasing θ or σ serves to facilitate capillary pumping and thereby broaden the range of admissible viscosity ratios and liquid layer thicknesses – see e.g. figures 2.13 and 2.22.

One small inconsistency embedded into our model derivation is that the interface is assumed to be flat insofar as applying a shear stress boundary condition, but curved insofar as supporting a capillary pressure that ultimately drives the liquid flow. This inconsistency is expected to be most significant when the interface deflection relative to the liquid layer depth is comparatively large. It remains to address the above inconsistency e.g. by incorporating the geometric details of a deflected interface in equation sets such as (2.16, 2.17, 2.20, 2.21) or (2.58, 2.59, 2.62, 2.63) using a perturbation analysis. An analysis along these lines is underway and shall be the topic of a forthcoming study.

An additional topic for further study that relates specifically to heat pipe design/operation is to extend the analyses summarized herein beyond the adiabatic section. One might ask, for instance, whether the optimum liquid layer depths predicted by the present model are sufficient to avoid performance-killing phenomena like evaporator-end dry out. Making reference to the heat pipe evaporator and condenser would necessarily entail a detailed consideration of not only phase change but also surface chemical effects (section 2.4.3). For example, some heat pipes are designed specifically to exploit drop-wise condensation and film-wise evaporation, both of which have been associated with increase of heat pipe performance (Daniel et al. 2001, Cheng et al. 2012). Whereas

these kinds of details do not influence the adiabatic section-centric results reported upon above, they would be potentially significant if the optimization were extended to include all three sections of the heat pipe.

2.8 Acknowledgements

Financial support for this study was generously provided by Engineered Air and by NSERC through its CRD program.

2.9 Data availability

The data that supports the finding of this study are available within the article.

2.10 Appendix A: Variable definitions

Table 1 shows the variables used in the analysis of sections II-V.

Symbol	**Meaning (unit, if applicable)**
L	Length of the adiabatic section (m)
H	Thickness of the symmetrical part of heat pipe (m)
u_v	Velocity of vapor (m/s)
u_l	Velocity of liquid (m/s)
δ	Thickness of the liquid layer (m)
π_v	Pressure gradient in vapour phase (kg/(m^{2}s^2))
π_l	Pressure gradient in liquid phase (kg/(m^{2}s^2))
μ_l	Viscosity in liquid phase (m^2/s)
μ_v	Viscosity in vapour phase (m^2/s)
μ_{ev}	Effective viscosity in vapour phase (m^2/s)
μ_{el}	Effective viscosity in liquid phase (m^2/s)
ρ_l	Density in liquid phase (kg/m^3)
ρ_v	Density in vapour phase (kg/m^3)
$c_\mu = \frac{\mu_v}{\mu_l}$	Viscosity ratio
$c_\rho = \frac{\rho_v}{\rho_l}$	Density ratio
$c_p = \frac{\pi_v}{\pi_l}$	Pressure gradient ratio
Δ	Thickness of the complete porous medium (m)
ε	Porosity
κ	Permeability (m^2)
β	Distance between center of two wires in a wick (m^2)
D	Diameter of the wick (m^2)
$\dot{m}_v$	Mass flow rate in vapour phase (kg/s)
$\dot{m}_l$	Mass flow rate in liquid phase (kg/s)

Table 2.1 – Variable definitions

2.11 Appendix B: Temperature and pressure relation

Our analysis requires specification of the liquid and vapor pressure gradients in order that velocity profiles and, by extension, optimum liquid layer thicknesses may be determined. From a pragmatic point of view, however, pressure gradients are less accessible than is the temperature difference between the evaporator and condenser. In this appendix, we provide insight into how such a temperature difference may inform π_v. With π_v to hand, the counterpart π_l may be estimated as soon as c_p is known.

Recall, first of all, that a linear pressure variation is assumed so that

$$\pi_v = \frac{1}{L}\left[p_v(x=L) - p_v(x=0)\right]. \tag{2.75}$$

The pressures that appear in the numerator of (2.75) may be replaced with temperatures using the Magnus equation (Alduchov et al. 1996). Assuming water as the working fluid, the correlation in question reads as follows:

$$p_v(x) = 0.61094\exp\left[\frac{17.625T_v(x=0)}{T_v(x)+243.04}\right], \tag{2.76}$$

where T_v indicates the vapor temperature measured along the interior of the heat pipe. From (2.75), it is evident that $T_v(x=0)$ and $T_v(x=L)$ are required and, for this purpose, we must consider the connection between this pair of interior temperatures and the corresponding exterior temperatures, which we shall respectively denote as $T_{\text{ext}}(x=0)$ and $T_{\text{ext}}(x=L)$. To wit,

$$T_v(x=L) = T_{\text{ext}}(x=L) - Q(R_{\text{shell}} + R_{\text{wick}}), \tag{2.77}$$

$$T_v(x=0) = T_{\text{ext}}(x=0) + Q(R_{\text{shell}} + R_{\text{wick}}), \tag{2.78}$$

where R_{shell} is the thermal resistance due to (conductive) heat transfer through the wall (or shell) of the heat pipe and R_{wick} is the thermal resistance due to heat transfer through the wick. Furthermore, and to a good approximation, the heat flux, Q, is given by

$$Q = \frac{T_{\text{shell}}(x=L) - T_{\text{shell}}(x=0)}{2(R_{\text{shell}} + R_{\text{wick}}) + R_{\text{axial}}}. \tag{2.79}$$

Note that in many cases of practical interest, the thermal resistance, R_{axial}, associated with heat transfer along the length of the heat pipe is much smaller than either of R_{shell} or R_{wick}. We expect, therefore, only a modest difference between $p_v(x=L)$ and $p_v(x=0)$, which, in turn, explains the small value of π_v (relative to π_l).

Chapter 3

Perturbation Theory Applied to a Two Phase Flow

3.1 Introduction

The work presented in the chapter 2 focussed on liquid-vapor counterflow using core annular flow theory. One inconsistency that our model contains is that the interface is assumed to be flat insofar as applying a shear stress boundary condition, but curved insofar as supporting a capillary pressure that ultimately drives the liquid flow. A heat pipe not assisted by gravity requires capillary pumping and that the radius of curvature of the liquid-vapor interface is lager at the evaporator end than it is at the condenser end. This difference gives rise to a difference in capillary pressure between the condenser section and the evaporator section that supports the flow of liquid (and vapor). Our heat pipe model ignores any kind of interface deflection and surface chemistry effects.

To address this discrepancy of assuming a flat interface versus assuming a deflected interface, this chapter presents a follow-up work to our existing model presented in chapter one. In this work, we assume that there is a small deflection at the interface and use perturbation theory to account for the small disturbance at the interface. The perturbation theory applied to the current problem gives an idea of whether or not we can use a flat interface at liquid and vapor interface in a porous medium.

For simplicity, we have the entire domain in the porous medium and extends till infinity. The liquid has a finite thickness and is in contact with the wall, and the vapor flows on top of the liquid and continues till infinity whereas, in chapter 2 the liquid and vapor layer were finite. An equal and opposite pressure gradient is maintained in liquid and vapor whereas, an equal and opposite mass flow rate in liquid and vapor was maintained in chapter 2. We are using square wires instead of circular wires in our porous medium because using circular wires changes the horizontal position of the triple point along with the vertical position whereas in square wires only the vertical position of the triple point changes. But we used circular wires in chapter 2. The rest of the work is organized

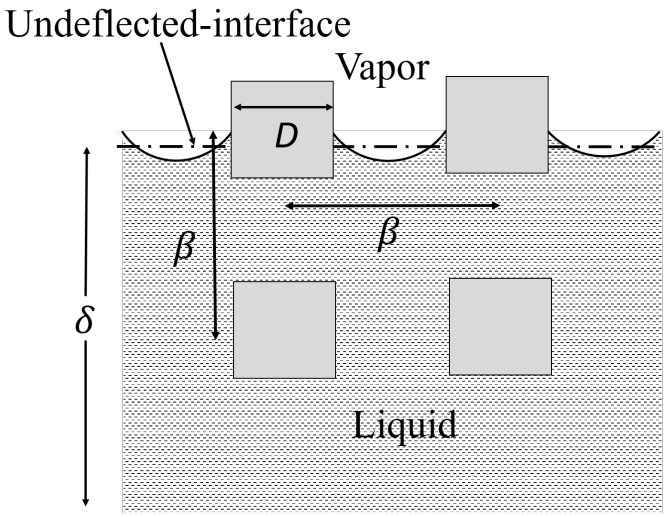

Figure 3.1 – Liquid layer has a finite thickness and vapor layer has infinite thickness.

as follows: Section 3.2 shows the meniscus deflection. Section 3.3 shows the solutions to the leading order solution and composite solution after applying the perturbation theory. Section 3.3.2 shows the percentage difference in the velocity profiles after using a deflected interface. Finally, the conclusion discusses the results and the advantage of this analysis.

3.2 Deflection at the liquid-vapor interface

This section provides information about the liquid-vapor interface deflection to support the capillary pressure. Our entire analysis focusses on one single cell to study the interface deflection. Once the problem is solved for one cell, the approach is similar for all the other cells too. The wires considered in our problem are square wires rather than cylindrical. Considering square wires makes the derivation of meniscus shape easy without changing the essential physics of the deflected interface as the horizontal position of the triple point does not change. Unlike, in our previous analysis the interface height is dependent on x and is no more a constant $z = \delta$. Figure 3.1 shows the deflection of the interface.

Meniscus is given by $\eta(x) = \delta(1 + \frac{t'}{\delta} f(x))$, here $f(x)$ and $t' \ll \delta$ measures the deflection of the interface in a manner to be clarified below. The deflection in the meniscus is due to a pressure difference between the two phases therefore, using Young-Laplace equation we find the complete expression for $\eta(x)$

$$\frac{\Delta p}{\sigma} = \frac{\eta_{xx}}{(1+\eta_x^2)^{\frac{3}{2}}} \tag{3.1}$$

Figure 3.2 shows the interface is symmetrical around $x = 0$. Using this fact while integrating

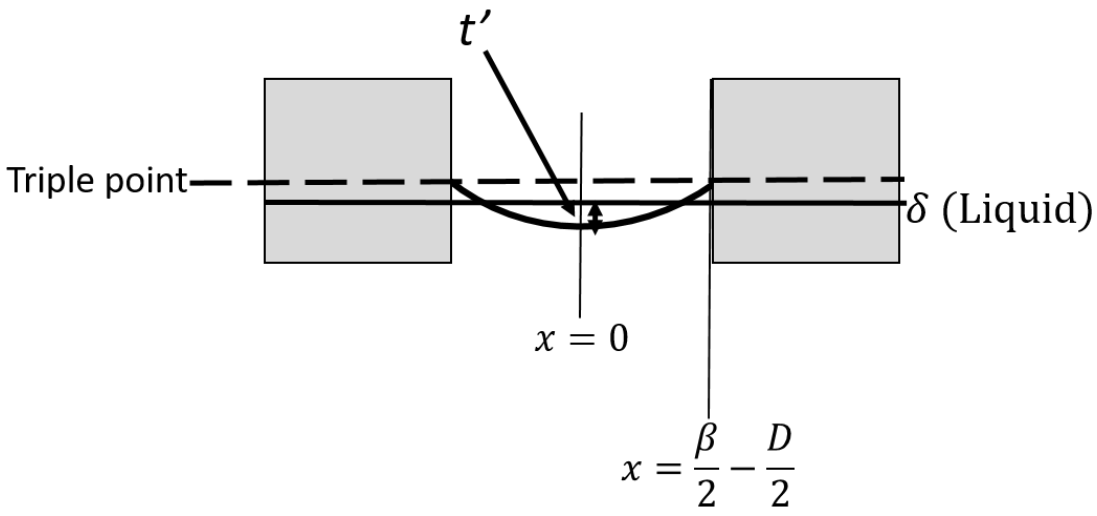

Figure 3.2 – Meniscus deflection and the triple point

(3.1) gives,

$$\eta(x) = -\frac{\sigma}{\Delta p}\left(1-\left(\frac{\Delta p}{\sigma}x\right)^2\right)^{\frac{1}{2}} + \delta - t' + \frac{\sigma}{\Delta p} \tag{3.2}$$

where t' is defined in figure 3.2. Rearranging the above result yields

$$\eta = \delta + \frac{t'}{\delta}\delta\left(\frac{\sigma}{t'\Delta p} - \frac{\sigma}{t'\Delta p}\left(1-\left(\frac{\Delta p}{\sigma}x\right)^2\right)^{\frac{1}{2}} - 1\right) \tag{3.3}$$

or, more simply,

$$\eta = \delta + \Phi\delta f(x) \tag{3.4}$$

Here, $\Phi \equiv \frac{t'}{\delta}$ and $f(x)$ is given by

$$f(x) = \left(\frac{\sigma}{t'\Delta p} - \frac{\sigma}{t'\Delta p}\left(1-\left(\frac{\Delta p}{\sigma}x\right)^2\right)^{\frac{1}{2}} - 1\right) \tag{3.5}$$

The function $\eta(x)$ shown in (3.2) describes a circular arc with radius of curvature $R = \sigma/\Delta P$. The input parameters in our problem are β, D, σ and Δp.

By using the volume conservation under the deflected interface to the volume under an undeflected interface in one single cell, we can evaluate t'. (3.6) gives the volume conservation equation where $\frac{\beta}{2} - \frac{D}{2}$, is the x value at the triple point. Here wires are arranged in a square grid pattern, where β is the center to centre distance between two wires and D is the length of each side of the square wires as shown in figure 3.1.

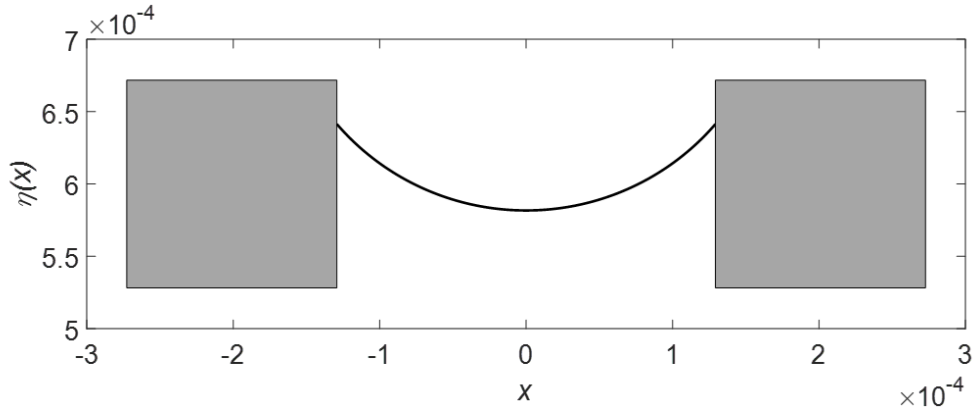

Figure 3.3 – Deflection of the menisus $\eta(x)$ within one single cell with $\delta = 0.0006$m, $\beta = 1.4 \times 10^{-4}$m, $D = 4 \times 10^{-4}$m, $\sigma = 0.0662$Nm^{-1}, $\Delta p = 390$Pa. The two squares indicate the cross sectional view of the wires.

$$\int_0^{\left(\frac{\beta}{2}-\frac{D}{2}\right)} \eta(x)dx = \delta\left(\frac{\beta}{2}-\frac{D}{2}\right) \tag{3.6}$$

Combining (3.3) and (3.6), it can be shown that

$$t' = \frac{1}{4}\frac{\sigma}{\Delta p^2(\beta - D)}\left(-4\sigma \arcsin\left(\frac{\Delta p(\beta - D)}{2\sigma}\right) - \Delta p(\beta - D)\left(\sqrt{\frac{4\sigma^2 - (\beta - D)^2\Delta p^2}{\sigma^2}} - 4\right)\right) \tag{3.7}$$

(3.7) gives the expression of t' in terms of the independent variables β, D, σ and Δp.

In order that a stable meniscus form and with reference to figure 3.2, we require that the meniscus deflection satisfy the condition given by

$$R > \frac{\beta - D}{2} \tag{3.8}$$

Here $R = \sigma/\Delta p$ is the meniscus radius of curvature. Hereby, we encounter another difference compared to chapter 2. In chapter 2 we used circular wires therefore, R could be related to the geometric details of the porous medium and also the surface chemistry, i.e. the contact angle, θ.

Figure 3.3 shows the deflection of the meniscus in one single cell. The values for the variables $\beta = 1.4 \times 10^{-4}$m, $D = 4 \times 10^{-4}$m, $\sigma = 0.0662$Nm^{-1} have been obtained from chapter one. The value for δ is taken to be 0.0006m unlike in chapter 2 where $\delta = 0.0007$m. We chose the value for the pressure difference between the liquid and vapor $\Delta p = 390$Pa, which falls within the range of values given in the experimental investigation of Shafahi et. al (2010). $\Delta p = 390$Pa is chosen to satisfy (3.8) and gives a 5% deflection of the interface. The percentage interface deflection

increases by increasing Δp. But increasing Δp more than a threshold value for a given edge-length and distance between the wires shifts the interface upwards near the triple point so that the meniscus is no longer in contact with the wires on both sides.

3.3 Liquid and vapor present in porous medium

This section involves the introduction of perturbation theory to solve the liquid-vapor counter flow present in an infinite porous medium.

3.3.1 Governing Equations

We again assume an incompressible, steady and laminar flow in both phases. By assumption, and consistent with figure 3.1, vapour and liquid are present in the porous medium. We assume that flow in the porous medium (whether liquid or vapor) is governed by the Brinkman equation (Durlofsky & Brady 1987). Brinkman's equation is derived from Darcy's law but includes a viscous shear dissipative term. With the above assumptions to hand the velocity of vapour and liquid in the porous medium are represented, respectively, by U_v and U_l and the (dimensional) governing equations now read

$$\frac{\mu_l}{\varepsilon}\left(\frac{d^2U_l}{dx^2}+\frac{d^2U_l}{dz^2}\right)-\frac{\mu_l}{\kappa}U_l=\frac{dp_l}{dx} \tag{3.9}$$

$$\frac{\mu_v}{\varepsilon}\left(\frac{d^2U_v}{dx^2}+\frac{d^2U_v}{dz^2}\right)-\frac{\mu_v}{\kappa}U_v=\frac{dp_v}{dx} \tag{3.10}$$

where $\frac{dp_v}{dx}$ and $\frac{dp_l}{dx}$ are the pressure gradients in the vapour and liquid respectively, μ_v and μ_l are the corresponding dynamic viscosities. ε is the porosity and κ is the permeability. The permeability is given by the Carmen-Kozeny equation, i.e.

$$\kappa=\frac{D^2\varepsilon^3}{100(1-\varepsilon)^2} \tag{3.11}$$

A no-slip boundary condition is maintained at the lower wall $z=0$, given by (3.12). A far-field boundary condition is maintained at $z\to\infty$ given by (3.13). A velocity and shear stress matching boundary condition (3.14) and (3.15) is maintained at the liquid vapor interface.

$$U_l(z=0)=0 \tag{3.12}$$

$$\frac{dU_v}{dz}|_{(z\to\infty)}=0 \tag{3.13}$$

$$U_l(z=\delta(1+\Phi f(x)))=U_v(z=\delta(1+\Phi f(x))) \tag{3.14}$$

$$\mu_l \frac{dU_l}{dz}|_{(z=\delta(1+\Phi f(x)))} = \mu_v \frac{dU_v}{dz}|_{(z=\delta(1+\Phi f(x)))} \tag{3.15}$$

The problem assumes a deflection at the interface. Keeping this assumption in mind and using the results obtained in section 3.2 we can assume a perturbation based solution in terms of small disturbance $\Phi = \frac{t'}{\delta}$. Thus, the perturbed velocity for U_l and U_v is shown in (3.16) and (3.17) respectively.

$$U_l = U_{l0} + \Phi U_{l1} + \text{H.O.T} \tag{3.16}$$

$$U_v = U_{v0} + \Phi U_{v1} + \text{H.O.T} \tag{3.17}$$

where, 'H.O.T' represents higher order terms of Φ. Plugging in (3.16) and (3.17) in the governing equations (3.9) and (3.10) gives

$$\left(\frac{\mu_l}{\varepsilon}\left(\frac{d^2U_{l0}}{dx^2} + \frac{d^2U_{l0}}{dz^2}\right) - \frac{\mu_l}{\kappa}U_{l0}\right) + \Phi\left(\frac{\mu_l}{\varepsilon}\left(\frac{d^2U_{l1}}{dx^2} + \frac{d^2U_{l1}}{dz^2}\right) - \frac{\mu_l}{\kappa}U_{l1}\right) + \text{H.O.T} = \frac{dp_l}{dx} \tag{3.18}$$

$$\left(\frac{\mu_v}{\varepsilon}\left(\frac{d^2U_{v0}}{dx^2} + \frac{d^2U_{v0}}{dz^2}\right) - \frac{\mu_v}{\kappa}U_{v0}\right) + \Phi\left(\frac{\mu_v}{\varepsilon}\left(\frac{d^2U_{v1}}{dx^2} + \frac{d^2U_{v1}}{dz^2}\right) - \frac{\mu_v}{\kappa}U_{v1}\right) + \text{H.O.T} = \frac{dp_v}{dx} \tag{3.19}$$

Meanwhile plugging in (3.16) and (3.17) in the no-slip and far-field boundary conditions gives

$$U_{l0}(z=0) + \Phi U_{l1}(z=0) + \text{H.O.T} = 0 \tag{3.20}$$

$$\frac{dU_{v0}}{dz}|_{(z\to\infty)} + \Phi\frac{dU_{v1}}{dz}|_{(z\to\infty)} + \text{H.O.T} = 0 \tag{3.21}$$

Using Taylor-series expansion the matching boundary condition (3.14) can be written as

$$U_l(z=\delta) + \Phi\delta f\frac{dU_l}{dz}|_{(z=\delta)} + \text{H.O.T} = U_v(z=\delta) + \Phi\delta f\frac{dU_v}{dz}|_{(z=\delta)} + \text{H.O.T} \tag{3.22}$$

Substituting (3.16) and (3.17) in (3.22) gives

$$\begin{aligned} &U_{l0}(z=\delta) + \Phi\left(U_{l1}(z=\delta) + \delta f\frac{dU_{l0}}{dz}|_{(z=\delta)}\right) + \text{H.O.T} = \\ &U_{v0}(z=\delta) + \Phi\left(U_{v1}(z=\delta) + \delta f\frac{dU_{v0}}{dz}|_{(z=\delta)}\right) + \text{H.O.T} \end{aligned} \tag{3.23}$$

Similarily after applying Taylor-series and substituting (3.16) and (3.17) in the shear-stress boundary condition (3.15) gives

$$\mu_l\left(\frac{dU_{l0}}{dz}|_{(z=\delta)}+\Phi\left(\frac{dU_{l1}}{dz}|_{(z=\delta)}+\delta f\frac{d^2U_{l0}}{dz^2}|_{(z=\delta)}\right)+\text{H.O.T}\right)= \tag{3.24}$$
$$\mu_v\left(\frac{dU_{v0}}{dz}|_{(z=\delta)}+\Phi\left(\frac{dU_{v1}}{dz}|_{(z=\delta)}+\delta f\frac{d^2U_{v0}}{dz^2}|_{(z=\delta)}\right)+\text{H.O.T}\right)$$

Leading order Solution

The leading order solution is obtained by equating the zeroth order of the small parameter Φ in left hand side and right hand side of (3.18) and (3.19). The governing equations are independent of x and are given by

$$\frac{\mu_l}{\varepsilon}\left(\frac{d^2U_{l0}}{dz^2}\right)-\frac{\mu_l}{\kappa}U_{l0}=\frac{dp_l}{dx} \tag{3.25}$$

$$\frac{\mu_v}{\varepsilon}\left(\frac{d^2U_{v0}}{dz^2}\right)-\frac{\mu_v}{\kappa}U_{v0}=\frac{dp_v}{dx} \tag{3.26}$$

The boundary conditions are again obtained by equating the zeroth order of Φ in the no-slip boundary condition (3.20), the far field boundary condition (3.21), matching boundary condition (3.22) and shear stress boundary condition (3.24)

$$U_{l0}(z=0)=0 \tag{3.27}$$

$$\frac{dU_{v0}}{dz}|_{(z\to\infty)}=0 \tag{3.28}$$

$$U_{l0}(z=\delta)=U_{v0}(z=\delta) \tag{3.29}$$

$$\mu_l\frac{dU_{l0}}{dz}|_{(z=\delta)}=\mu_v\frac{dU_{v0}}{dz}|_{(z=\delta)} \tag{3.30}$$

Solving (3.25) and (3.26) gives the following respective solutions:

$$U_{l0}=A\exp\left(\sqrt{\frac{\varepsilon}{\kappa}}z\right)+B\exp\left(-\sqrt{\frac{\varepsilon}{\kappa}}z\right)-\frac{\kappa}{\mu_l}\frac{dp_l}{dx}\qquad 0<z<\delta \tag{3.31}$$

$$U_{v0}=a\exp\left(\sqrt{\frac{\varepsilon}{\kappa}}z\right)+b\exp\left(-\sqrt{\frac{\varepsilon}{\kappa}}z\right)-\frac{\kappa}{\mu_v}\frac{dp_v}{dx}\qquad \delta<z<\infty \tag{3.32}$$

Using the far field boundary condition the vapor velcity expression becomes

$$U_{v0}=b\exp\left(-\sqrt{\frac{\varepsilon}{\kappa}}z\right)-\frac{\kappa}{\mu_v}\frac{dp_v}{dx} \tag{3.33}$$

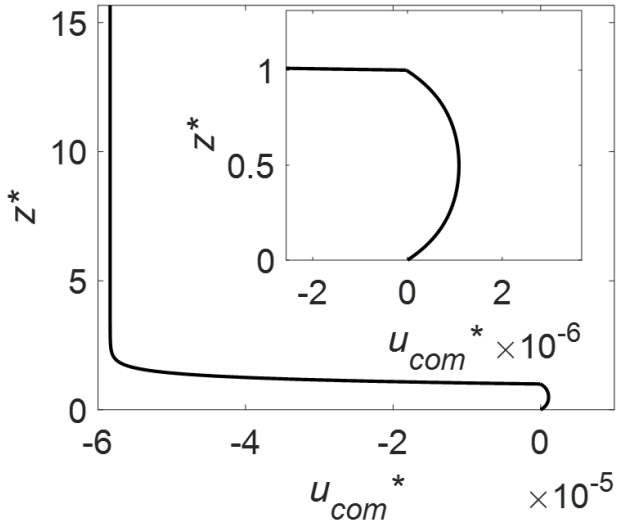

Figure 3.4 – Velocity profile with $H = 0.0094$m, $\delta = 0.0006$m, $D = 1.4 \times 10^{-4}$m, $\beta = 4 \times 10^{-4}$m, $\sigma = 0.0662\text{Nm}^{-1}$, $\Delta p = 390$Pa, $\frac{dp_v}{dx} = 1.11\text{Pa/m}$.

The constants A, B and b are determined using (3.27)-(3.30). The theoretical expressions for these constants are shown in (3.34), (3.35) and (3.36).

$$A = \frac{\kappa}{\mu_l} \frac{\left[(-\mu_l \pi_v + \mu_v \pi_l) \exp\left(\sqrt{\frac{\varepsilon}{\kappa}}\delta\right) + \pi_l (\mu_l - \mu_v)\right]}{\left[(\mu_l + \mu_v) \exp\left(2\sqrt{\frac{\varepsilon}{\kappa}}\delta\right) + \mu_l - \mu_v\right]} \tag{3.34}$$

$$B = \frac{\kappa}{\mu_l} \exp\left(\sqrt{\frac{\varepsilon}{\kappa}}\delta\right) \frac{\left[\pi_l (\mu_l + \mu_v) \exp\left(\sqrt{\frac{\varepsilon}{\kappa}}\delta\right) + \mu_l \frac{dp_v}{dx} - \mu_v \frac{dp_l}{dx}\right]}{\left[(\mu_l + \mu_v) \exp\left(2\sqrt{\frac{\varepsilon}{\kappa}}\delta\right) + \mu_l - \mu_v\right]} \tag{3.35}$$

$$b = \frac{\kappa}{\mu_v} \exp\left(\sqrt{\frac{\varepsilon}{\kappa}}\delta\right) \frac{\left[\left(\mu_l \frac{dp_v}{dx} - \mu_v \frac{dp_l}{dx}\right) \exp\left(2\sqrt{\frac{\varepsilon}{\kappa}}\delta\right) + 2\exp\left(\sqrt{\frac{\varepsilon}{\kappa}}\delta\right) \mu_v \frac{dp_l}{dx} + \mu_l \frac{dp_v}{dx} - \mu_v \frac{dp_l}{dx}\right]}{\left[(\mu_l + \mu_v) \exp\left(2\sqrt{\frac{\varepsilon}{\kappa}}\delta\right) + \mu_l - \mu_v\right]} \tag{3.36}$$

Figure 3.4 shows the velocity profile for the leading order solution. The height of the domain chosen to represent the velocity profile is $H = 0.0094$m. The values for all the variables except for δ are again obtained from chapter 2. The velocity profile is non-dimensionlized using δ, μ_v and $\frac{dp_v}{dx}$ as characteristic variables. Thus, we define

$$u_v^* = \frac{\mu_v}{\delta^2 \frac{dp_v}{dx}} U_v \qquad \text{and} \qquad u_l^* = \frac{\mu_v}{\delta^2 \frac{dp_v}{dx}} U_l,$$

where stars indicate non-dimensional variables. In a similar spirit, $z^* = z/\delta$.

First order Solution

The governing equations for the first order solution is obtained by equating order one terms of the small parameter 'Φ' in (3.18) and (3.19)

$$\frac{\mu_l}{\varepsilon}\left(\frac{d^2U_{l1}}{dx^2}+\frac{d^2U_{l1}}{dz^2}\right)-\frac{\mu_l}{\kappa}U_{l1}=0 \tag{3.37}$$

$$\frac{\mu_v}{\varepsilon}\left(\frac{d^2U_{v1}}{dx^2}+\frac{d^2U_{v1}}{dz^2}\right)-\frac{\mu_v}{\kappa}U_{v1}=0 \tag{3.38}$$

The order one governing equations are Helmholtz equations (Rees et al. 2004). In order to solve the Helmholtz equations we seek a solution of U_{v1} by assuming the solution in the form given below:

$$U_{v1}=X(x)Z(z) \tag{3.39}$$

Substituting (3.39) in (3.38) we get

$$\frac{Z''}{Z}+\frac{X''}{X}-\frac{\varepsilon}{\kappa}=0 \tag{3.40}$$

Equation (3.40) can also be written as

$$\frac{Z''}{Z}-\frac{\varepsilon}{\kappa}=-\frac{X''}{X}=\lambda^2 \tag{3.41}$$

where λ is an eigen-value. From (3.41) we get the following two equations

$$Z''-\left(\frac{\varepsilon}{\kappa}+\lambda^2\right)Z=0 \tag{3.42}$$

$$X''+\lambda^2X=0 \tag{3.43}$$

Solving the eigen-value problem (3.42) for $Z(z)$ gives

$$Z=C_{1\lambda}\exp\left(\sqrt{\left(\frac{\varepsilon}{\kappa}+\lambda^2\right)}z\right)+C_{2\lambda}\exp\left(-\sqrt{\left(\frac{\varepsilon}{\kappa}+\lambda^2\right)}z\right) \tag{3.44}$$

Solving (3.43) for $X(x)$ gives

$$X=C_{3\lambda}\cos(\lambda x)+C_{4\lambda}\sin(\lambda x) \tag{3.45}$$

The full solution for U_{v1} is therefore

$$U_{v1}=\left[C_{1\lambda}\exp\left(\sqrt{\frac{\varepsilon}{\kappa}+\lambda^2}z\right)+C_{2\lambda}\exp\left(-\sqrt{\frac{\varepsilon}{\kappa}+\lambda^2}z\right)\right]\left[C_{3\lambda}\sin(\lambda x)+C_{4\lambda}\cos(\lambda x)\right] \tag{3.46}$$

Reducing the number of constants by dividing all the constants with $C_{2\lambda}$ we get the vapor velocity expression given below

$$U_{v1} = \left[c_{1\lambda}\exp\left(\sqrt{\frac{\varepsilon}{\kappa}+\lambda^2}z\right)+\exp\left(-\sqrt{\frac{\varepsilon}{\kappa}+\lambda^2}z\right)\right]\left[c_{2\lambda}\sin(\lambda x)+c_{3\lambda}\cos(\lambda x)\right] \tag{3.47}$$

Similiarily, the velocity expression for liquid is given by

$$U_{l1} = \left[c_{4\lambda}\exp\left(\sqrt{\frac{\varepsilon}{\kappa}+\lambda^2}z\right)+\exp\left(-\sqrt{\frac{\varepsilon}{\kappa}+\lambda^2}z\right)\right]\left[c_{5\lambda}\sin(\lambda x)+c_{6\lambda}\cos(\lambda x)\right] \tag{3.48}$$

Now replacing

$$\lambda \to \lambda_n = \frac{n\pi}{L} \tag{3.49}$$

here $L = \frac{\beta - D}{2}$, again reminding ourselves that our focus is only a single cell so our interest length is the free distance between two wires and n is an integer with values from 0 to ∞. We can write the eigen-values in terms of n. The sin terms are dropped as the meniscus is symmetrical about $x = 0$ and the final solution will be summation for all values of n.

$$U_{v1} = \sum_{n=0}^{\infty}\left[c_{1n}\exp\left(\sqrt{\frac{\varepsilon}{\kappa}+\left(\frac{n\pi}{L}\right)^2}z\right)+\exp\left(-\sqrt{\frac{\varepsilon}{\kappa}+\left(\frac{n\pi}{L}\right)^2}z\right)\right]\left[c_{3n}\cos\left(\frac{n\pi x}{L}\right)\right] \tag{3.50}$$

$$U_{l1} = \sum_{n=0}^{\infty}\left[c_{4n}\exp\left(\sqrt{\frac{\varepsilon}{\kappa}+\left(\frac{n\pi}{L}\right)^2}z\right)+\exp\left(-\sqrt{\frac{\varepsilon}{\kappa}+\left(\frac{n\pi}{L}\right)^2}z\right)\right]\left[c_{6n}\cos\left(\frac{n\pi x}{L}\right)\right] \tag{3.51}$$

The boundary conditions are also obtained by equating the order one of the small parameter in (3.20), (3.21), (3.23) and (3.24) revealing that

$$U_{l1}(z=0) = 0 \tag{3.52}$$

$$\frac{dU_{v1}}{dz}|_{(z\to\infty)} = 0 \tag{3.53}$$

$$\left(U_{l1}(z=\delta)+\delta f\frac{dU_{l0}}{dz}|_{(z=\delta)}\right) = \left(U_{v1}(z=\delta)+\delta f\frac{dU_{v0}}{dz}|_{(z=\delta)}\right) \tag{3.54}$$

$$\mu_l\left(\frac{dU_{l1}}{dz}|_{(z=\delta)}+\delta f\frac{d^2U_{l0}}{dz^2}|_{(z=\delta)}\right) = \mu_v\left(\frac{dU_{v1}}{dz}|_{(z=\delta)}+\delta f\frac{d^2U_{v0}}{dz^2}|_{(z=\delta)}\right) \tag{3.55}$$

Using the no-slip boundary condition (3.52) we get

$$\sum_{n=0}^{\infty}\left(c_{4n}+1\right)c_{6n}\cos\left(\frac{n\pi x}{L}\right) = 0 \tag{3.56}$$

The only non-trivial solution to (3.56) is $c_{4n} = -1$. Applying the far field boundary condition (3.53) to (3.50), we note that $\exp\left(\sqrt{\frac{\varepsilon}{\kappa}+\left(\frac{n\pi}{L}\right)^2}z\right) \to \infty$ therefore $c_{1n} = 0$. Thus, our velocity expression simplifies to the equations given below:

$$U_{v1} = \sum_{n=0}^{\infty}\left[\exp\left(-\sqrt{\frac{\varepsilon}{\kappa}+\left(\frac{n\pi}{L}\right)^2}z\right)\right]\left[c_{3n}\cos\left(\frac{n\pi}{L}x\right)\right] \tag{3.57}$$

$$U_{l1} = \sum_{n=0}^{\infty}\left[-2\sinh\left(\sqrt{\frac{\varepsilon}{\kappa}+\left(\frac{n\pi}{L}\right)^2}z\right)\right]\left(c_{6n}\cos\left(\frac{n\pi}{L}x\right)\right) \tag{3.58}$$

The remaining constants c_{3n} and c_{6n} are evaluated using (3.54) and (3.55) which make reference to the leading order solution. The leading order solution does not depend upon n or x therefore is straightforward to incorporate. Rearranging and substituting (3.31) and (3.32) in (3.54) gives

$$U_{l1}(z=\delta) - U_{v1}(z=\delta) = \tag{3.59}$$
$$\delta f(x)\left[-\frac{\kappa(\mu_l-\mu_v)}{\mu_l\mu_v}\sqrt{\frac{\varepsilon}{\kappa}}\frac{\left[(\mu_l\pi_{v0}-\mu_l\pi_{l0})\exp\left(2\delta\sqrt{\frac{\varepsilon}{\kappa}}\right)+2\exp\left(\delta\sqrt{\left(\frac{\varepsilon}{\kappa}\right)}\right)\mu_v\pi_{l0}+\mu_l\pi_{v0}-\mu_v\pi_{l0}\right]}{\left[(\mu_l+\mu_v)\exp\left(2\delta\sqrt{\frac{\varepsilon}{\kappa}}\right)+\mu_l-\mu_v\right]}\right]$$

Substituting (3.57) and (3.58) in (3.59)

$$\sum_{n=0}^{\infty}-2\sinh\left(\delta\sqrt{\frac{\varepsilon}{\kappa}+\lambda^2}\right)c_{6n}\cos(\lambda x) - \sum_{n=0}^{\infty}\exp\delta\left(-\sqrt{\frac{\varepsilon}{\kappa}+\lambda^2}\right)c_{3n}\cos(\lambda x) \tag{3.60}$$
$$= \delta f(x)\left[-\frac{\kappa(\mu_l-\mu_v)}{\mu_l\mu_v}\sqrt{\frac{\varepsilon}{\kappa}}\frac{\left[(\mu_l\pi_{v0}-\mu_l\pi_{l0})\exp\left(2\sqrt{\frac{\varepsilon}{\kappa}}\delta\right)+2\exp\left(\sqrt{\left(\frac{\varepsilon}{\kappa}\right)}\delta\right)\mu_v\pi_{l0}+\mu_l\pi_{v0}-\mu_v\pi_{l0}\right]}{\left[(\mu_l+\mu_v)\exp\left(2\sqrt{\frac{\varepsilon}{\kappa}}\delta\right)+\mu_l-\mu_v\right]}\right]$$

(3.60) involves $f(x)$ which can, for purposes of solving for c_{3n} and c_{6n}, be written in terms of its constituent Fourier components, i.e.

$$f(x) = \sum_{n=0}^{\infty}a_n\cos\left(\frac{n\pi x}{L}\right) \tag{3.61}$$

where

$$a_0 = \frac{1}{2L}\int_{-L}^{L}f(x)dx \tag{3.62}$$

and

$$a_n = \frac{1}{L}\int_{-L}^{L}f(x)\cos\left(\frac{n\pi x}{L}\right)dx \tag{3.63}$$

Now substituting $f(x)$ in (3.60) we get

$$\sum_{n=0}^{\infty} -2\sinh\left(\delta\sqrt{\frac{\varepsilon}{\kappa}+\left(\frac{n\pi}{L}\right)^2}\right)c_{6n}\cos\left(\frac{n\pi x}{L}\right)-\sum_{n=0}^{\infty}\exp\left(-\delta\sqrt{\frac{\varepsilon}{\kappa}+\left(\frac{n\pi}{L}\right)^2}\right)c_{3n}\cos\left(\frac{n\pi x}{L}\right)= \tag{3.64}$$

$$\left[-\frac{\kappa(\mu_l-\mu_v)}{\mu_l\mu_v}\sqrt{\frac{\varepsilon}{\kappa}}\frac{\left[(\mu_l\pi_{v0}-\mu_l\pi_{l0})\exp\left(2\delta\sqrt{\frac{\varepsilon}{\kappa}}\right)+2\exp\left(\delta\sqrt{\frac{\varepsilon}{\kappa}}\right)\mu_v\pi_{l0}+\mu_l\pi_{v0}-\mu_v\pi_{l0}\right]}{\left[(\mu_l+\mu_v)\exp\left(2\delta\sqrt{\frac{\varepsilon}{\kappa}}\right)+\mu_l-\mu_v\right]}\right]$$

$$\delta\left(\sum_{n=0}^{\infty}a_n\cos\left(\frac{n\pi x}{L}\right)\right)$$

Similarily, the shear-stress boundary condition (3.55) for the first order solution is rearranged as shown below

$$\mu_l\frac{dU_{l1}}{dz}|_{(z=\delta)}-\mu_v\frac{dU_{v1}}{dz}|_{(z=\delta)}= \tag{3.65}$$

$$\left[-2\varepsilon\exp\left(\delta\sqrt{\frac{\varepsilon}{\kappa}}\right)\frac{\left[(-\mu_l\pi_{v0}+\mu_l\pi_{l0})\exp\left(\delta\sqrt{\frac{\varepsilon}{\kappa}}\right)+\pi_{l0}(\mu_l-\mu_v)\right]}{\left[(\mu_l+\mu_v)\exp\left(2\delta\sqrt{\frac{\varepsilon}{\kappa}}\right)+\mu_l-\mu_v\right]}\right]\delta\left(\sum_{n=0}^{\infty}a_n\cos\left(\frac{n\pi x}{L}\right)\right)$$

Substituting (3.57), (3.58) and (3.61) in (3.65) we get

$$\mu_v\left(\sqrt{\frac{\varepsilon}{\kappa}+\left(\frac{n\pi}{L}\right)^2}\right)\sum_{n=0}^{\infty}\exp\left(-\delta\sqrt{\frac{\varepsilon}{\kappa}+\left(\frac{n\pi}{L}\right)^2}\right)c_{3n}\cos\left(\frac{n\pi x}{L}\right)- \tag{3.66}$$

$$\mu_l\sum_{n=0}^{\infty}2\sqrt{\frac{\varepsilon}{\kappa}+\left(\frac{n\pi}{L}\right)^2}\cosh\left(\delta\sqrt{\frac{\varepsilon}{\kappa}+\left(\frac{n\pi}{L}\right)^2}\right)c_{6n}\cos\left(\frac{n\pi x}{L}\right)$$

$$=\delta\left[-2\delta\varepsilon\exp\left(\sqrt{\frac{\varepsilon}{\kappa}}\right)\frac{\left[(-\mu_l\pi_{v0}+\mu_l\pi_{l0})\exp\left(\delta\sqrt{\frac{\varepsilon}{\kappa}}\right)+\pi_{l0}(\mu_l-\mu_v)\right]}{\left[(\mu_l+\mu_v)\exp\left(2\delta\sqrt{\frac{\varepsilon}{\kappa}}\right)+\mu_l-\mu_v\right]}\right]\left(\sum_{n=0}^{\infty}a_n\cos\left(\frac{n\pi x}{L}\right)\right)$$

The coefficients c_{3n} and c_{6n} are calculated with reference to the factors of a_n that appear on the RHS of (3.64) and (3.66). Now by multiplying by $\cos(m\pi x/L)$, where m is again the set of all positive integers and then integrating and exploiting trigonometric orthogonality, it can be shown that

$$c_{3n} = -\frac{\delta}{L}\exp\left(\delta\sqrt{\left(\frac{n\pi}{L}\right)^2+\frac{\varepsilon}{\kappa}}\right)\left[\cosh\left(\delta\sqrt{\left(\frac{n\pi}{L}\right)^2+\frac{\varepsilon}{\kappa}}\right)\mu_l\sqrt{\left(\frac{n\pi}{L}\right)^2+\frac{\varepsilon}{\kappa}}\right. \tag{3.67}$$
$$\left[-\frac{\kappa(\mu_l-\mu_v)}{\mu_l\mu_v}\sqrt{\frac{\varepsilon}{\kappa}}\frac{\left[(\mu_l\pi_{v0}-\mu_l\pi_{l0})\exp\left(2\delta\sqrt{\frac{\varepsilon}{\kappa}}\right)+2\exp\left(\delta\sqrt{\left(\frac{\varepsilon}{\kappa}\right)}\right)\mu_v\pi_{l0}+\mu_l\pi_{v0}-\mu_v\pi_{l0}\right]}{\left[(\mu_l+\mu_v)\exp\left(2\delta\sqrt{\frac{\varepsilon}{\kappa}}\right)+\mu_l-\mu_v\right]}\right]\times$$
$$\left.\sinh\left(\delta\sqrt{\left(\frac{n\pi}{L}\right)^2+\frac{\varepsilon}{\kappa}}\right)\left[2\varepsilon\exp\left(\sqrt{\frac{\varepsilon}{\kappa}}\delta\right)\frac{\left[(-\mu_l\pi_{v0}+\mu_l\pi_{l0})\exp\left(\sqrt{\frac{\varepsilon}{\kappa}}\delta\right)+\pi_{l0}(\mu_l-\mu_v)\right]}{\left[(\mu_l+\mu_v)\exp\left(2\sqrt{\frac{\varepsilon}{\kappa}}\delta\right)+\mu_l-\mu_v\right]}\right]\right]\times$$
$$\frac{1}{\sqrt{\left(\frac{n\pi}{L}\right)^2+\frac{\varepsilon}{\kappa}}}\frac{1}{\left(\cosh\left(\delta\sqrt{\left(\frac{n\pi}{L}\right)^2+\frac{\varepsilon}{\kappa}}\right)\mu_l+\sinh\left(\delta\sqrt{\left(\frac{n\pi}{L}\right)^2+\frac{\varepsilon}{\kappa}}\right)\mu_v\right)}\int_{-L}^{L}f(x)\cos\left(\frac{n\pi x}{L}\right)dx$$

$$c_{6n} = \left(\left[\frac{\kappa(\mu_l-\mu_v)}{\mu_l\mu_v}\sqrt{\frac{\varepsilon}{\kappa}}\frac{\left[(\mu_l\pi_{v0}-\mu_l\pi_{l0})\exp\left(2\delta\sqrt{\frac{\varepsilon}{\kappa}}\right)+2\exp\left(\delta\sqrt{\left(\frac{\varepsilon}{\kappa}\right)}\right)\mu_v\pi_{l0}+\mu_l\pi_{v0}-\mu_v\pi_{l0}\right]}{\left[(\mu_l+\mu_v)\exp\left(2\delta\sqrt{\frac{\varepsilon}{\kappa}}\right)+\mu_l-\mu_v\right]}\right]\times\right. \tag{3.68}$$
$$\left.\mu_v\sqrt{\left(\frac{n\pi}{L}\right)^2-\frac{\varepsilon}{\kappa}}-\left[2\varepsilon\exp\left(\delta\sqrt{\frac{\varepsilon}{\kappa}}\right)\frac{\left[(-\mu_l\pi_{v0}+\mu_l\pi_{l0})\exp\left(\delta\sqrt{\frac{\varepsilon}{\kappa}}\right)+\pi_{l0}(\mu_l-\mu_v)\right]}{\left[(\mu_l+\mu_v)\exp\left(2\sqrt{\frac{\varepsilon}{\kappa}}\delta\right)+\mu_l-\mu_v\right]}\right]\right)\times$$
$$\frac{\delta}{2L\sqrt{\left(\frac{n\pi}{L}\right)^2+\frac{\varepsilon}{\kappa}}\left(\cosh\left(\delta\sqrt{\left(\frac{n\pi}{L}\right)^2+\frac{\varepsilon}{\kappa}}\right)\mu_l+\sinh\left(\delta\sqrt{\left(\frac{n\pi}{L}\right)^2+\frac{\varepsilon}{\kappa}}\right)\mu_v\right)}\int_{-L}^{L}f(x)\cos\left(\frac{n\pi x}{L}\right)dx$$

Using the constants and summation for all integer values of n the composite velocity solution given by (3.16) and (3.17) is plotted in figure 3.5. The solution is plotted for various x.

There is a discontinuity at the interface in the velocity profile. This is because the matching boundary condition and the shear stress boundary condition for the composite solution is linearized and is an approximation by neglecting the higher order terms of the small number in (3.23) and (3.24). The discontinuity becomes smaller as the interface deflection becomes smaller and also as x changes. The position of x where the difference between the leading order solution and the composite solution is least, is given by

$$x_1 = \frac{\sqrt{\Delta p t'(2\sigma - t'\Delta P)}}{\Delta p} \tag{3.69}$$

The equation given by (3.69) is the horizontal position where $\eta(x)$ becomes equal to δ. The position x_1 is also the location where the volume of liquid displaced by the meniscus from $x = 0$ to x_1 is equal to the volume of liquid under the meniscus measured from x_1 to the triple point.

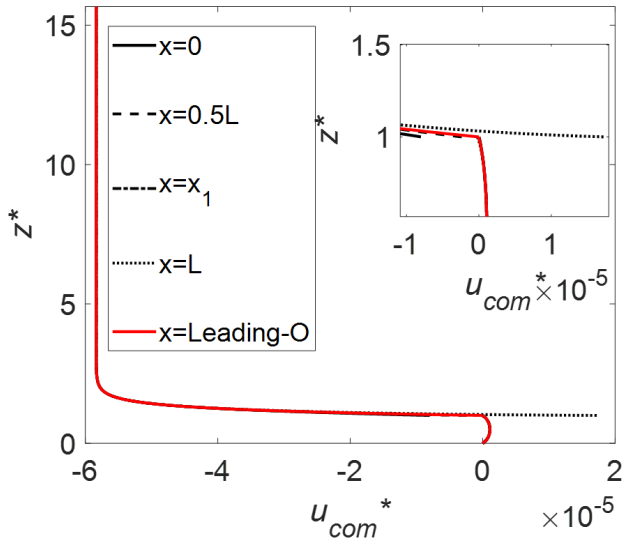

Figure 3.5 – Composite velocity profile with $H = 0.0094$m, $\delta = 0.0006$m, $\kappa = 1.5 \times 10^{-8}$m^2, $\varepsilon = 0.9$, $\sigma = 0.0662$Nm^{-1}, $\Delta p = 390$Pa and $\frac{dp_v}{dx} = 1.11$Pa/m. x_1 represents the horizontal position where $\eta(x)$ is equal to δ and is given by (3.69). The red curve represents the leading order solution.

3.3.2 Percentage velocity difference with percentage increase in interface deflection

This section shows an analysis involving the percentage interface deflection with the percentage velocity difference between the base solution and the composite solution. Figure 3.6 shows the percentage deflection (as evaluated for different Δp spanning a range 0.01 Pa to 395 Pa) plotted for different δ/β . The interface deflection is measured at $x = 0$ and so corresponds to a maximum deflection in the interval $-\frac{1}{2}(\beta - D) < x < \frac{1}{2}(\beta - D)$. Meanwhile, the velocity difference is evaluated at $x = 0$ and $z = \delta$. More precisely, the percentage velocity difference is given by $\frac{U-U_0}{U_{far-field}} \times 100$ where U_0 is the base solution, U is the composite solution and $U_{far-field}$ is the far-field velocity. The percentage interface deflection is given by $\frac{\delta - \eta_{min}}{\delta} \times 100$.

Figure 3.6 shows that the percent velocity difference typically exceeds the percent interface deflection. This result gives us the impression that even for a very small interface deflection we encounter a large change in the velocity, therefore the results obtained in chapter one by assuming a flat interface are of limited value. It is important to highlight, however, that the velocities in Figure 3.6 are measured at $z = \delta$ where the difference between the leading order solution and composite solution is greatest, therefore we can see a large change in velocity. However, when the velocity is measured at a different vertical position the difference between the leading order solution and the composite solution is often negligible as can be seen in figure 3.7. Figure 3.7 shows that the velocity difference is ussually small for different values of z but becomes comparatively large when

z approaches $\delta = 0.0006$m. Figure 3.8 is a 2-dimensional plot which shows that the velocity difference rises only when the vertical position approaches the interface but at other vertical positions the velocity differnce is negligible.

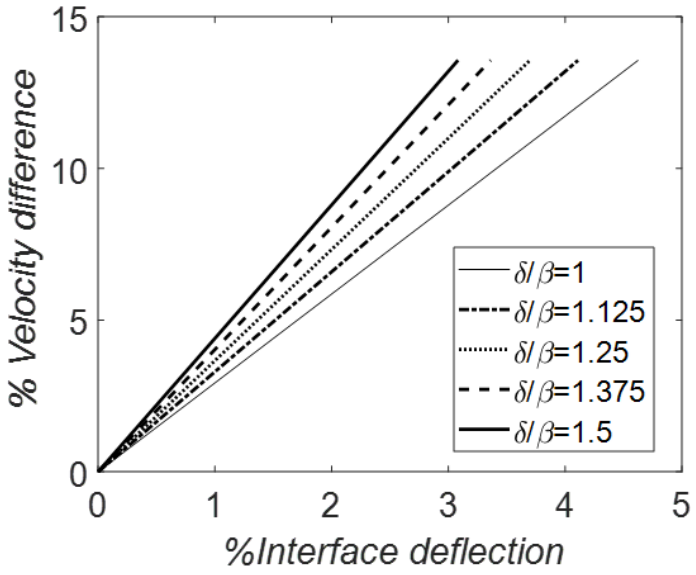

Figure 3.6 – Velocity difference versus the interface deflection for various δ with $\beta = 4 \times 10^{-4}$m, $D = 1.4 \times 10^{-4}$m, $\sigma = 0.0662$Nm^{-1}. Velocities are being measured at $z = \delta$.

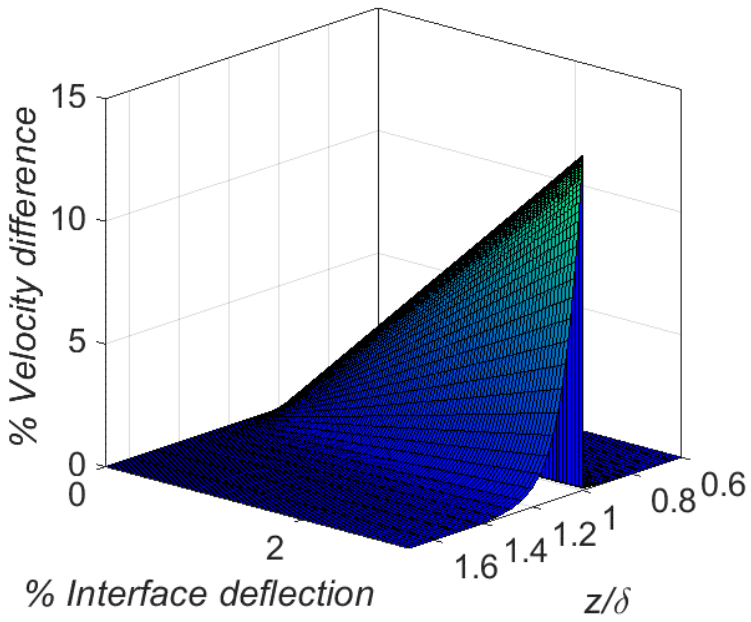

Figure 3.7 – Surface plot representing velocity difference with interface deflection and z with $H = 0.0094$m, $\delta = 0.0006$m, $\beta = 4 \times 10^{-4}$m, $D = 1.4 \times 10^{-4}$m and $\sigma = 0.0662$Nm^{-1}.

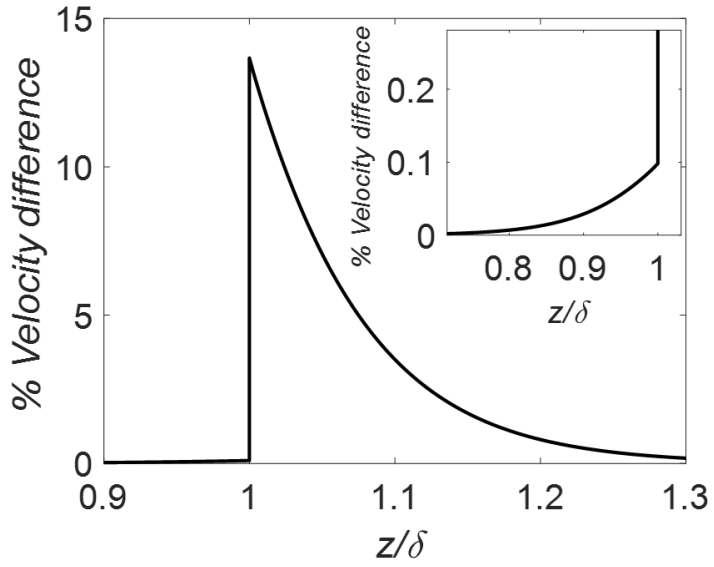

Figure 3.8 – Velocity difference versus z with $H = 0.0094$m, $\delta = 0.0006$m, $\beta = 4 \times 10^{-4}$m, $D = 1.4 \times 10^{-4}$m, $\sigma = 0.0662$Nm^{-1} and $\Delta p = 390$Pa. The inset plot shows the velocity differnce in the liquid section.

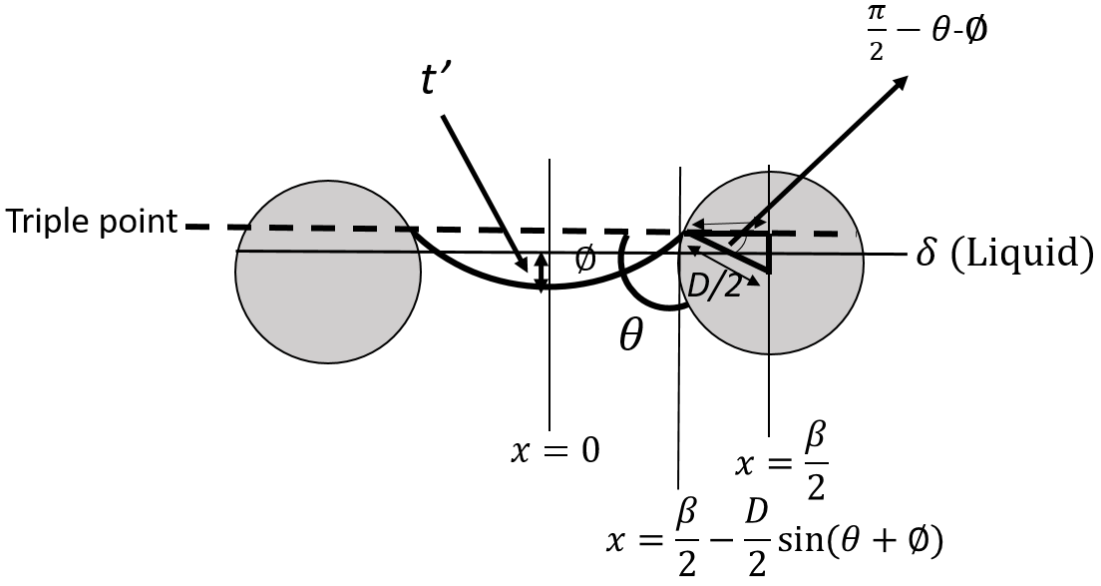

Figure 3.9 – Meniscus deflection for circular wires.

3.4 Conclusion

In this work, we have adapted perturbation theory to model the liquid-vapor flow in a porous medium. The key to our analysis is that we have considered pressure gradient of liquid and vapor to be equal and opposite i.e, $\frac{dp_v}{dx} = -\frac{dp_l}{dx}$ unlike the consideration of equal and opposite mass flow rate i.e, $-\dot{m}_v = \dot{m}_l$ in chapter 2. The reason for considering equal and opposite pressure gradients

is that we have taken an infinite domain to represent our problem hence, we cannot evaluate mass flow rate for the vapor phase.

We have performed our analysis by considering the deflected interface. To this end we have shown the schematic in figure 3.1 of section 3.2 which shows the liquid-vapor interface that is deflected from δ and is a function of x. This section shows the expression for the interface which is a circular arc given by (3.3).

In section 3.3 we use perturbation theory in our governing equations for liquid and vapor flow. Moreover, the matching and shear stress boundary conditions are maintained at $\eta(x)$ rather than δ. Figure 3.4 shows the velocity profile for the leading order solution. Figure 3.5 shows the composite solution after applying the perturbation theory and ignoring the higher-order terms of the smallness parameter. The difference between the composite velocity profile and the leading order velocity profile is less when x is given by (3.69) corresponding to the horizontal position where $\eta(x)$ is equal to δ and is shown in figure 3.5.

Finally in section 3.3.2, figure 3.6 shows the interface deflection and the velocity difference for different δ. Figure 3.7 shows the velocity difference with interface deflection at different z and $\delta = 0.0006$m. Figure 3.7 and 3.8 confirms that the velocity difference arises only when the vertical position approaches $z = \delta$ but at other vertical positions the velocity difference is small. Thus, we have reported the inconsistency appearing in chapter one and the significance of the assumption considered.

We have considered square wires instead of the circular wires to avoid the tedious work pertaining to circular wires while maintaining the volume conservation given in (3.6) when not only the $z-$coordinate of the triple point changes but also the $x-$coordinate as shown in figure 3.9. However, this analysis can also be performed for circular wires by removing the extra volume of the circular wires that comes into the picture while applying volume conservation. Figure 3.9 shows the interface deflection for circular wires.

Chapter 4

Summary and Conclusion

Core annular flow theory (CAF) can be adapted to model a two-phase flow. In Core annular flows, the core of a viscous liquid is surrounded by a layer of fluid with lower viscosity. As the layer of fluid with high viscosity does not make contact with the solid boundary, there is drag reduction. Core annular flow theory is used in lubricated flows for the transportation of bitumen forth in the oil companies (Joseph et al. 1995, Joseph et al. 1997, Gruncell et al. 2013).

The interest to depress drag led to the introduction of a superhydrophobic surface that retains the continuous air layer and separates the liquid layer with the solid layer. Numerous studies were performed to retain the air layer (Lee & Kim(2011), Panchanathan et al. (2018), Forsberg et al. (2011) and Forsberg et al. (2011) etcetera). Busse et al. (2013) provided the study about lubricated flows by the surface-attached gas layer. They also showed the velocity profiles and optimized thickness for the gas layer required to minimize the drag. The upper limits to drag reduction depends upon the width of the air layer. In core annular flows, the thickness of the air layer plays a significant role. If the air layer is too thin, then there is a modest reduction of overall shear stress. If the air layer is too thick, then the cross-sectional area for the flow of liquid is choked.

In this thesis, we have adopted the core annular flow (CAF) theory to model the adiabatic section of heat pipes. Unlike Busse et al. (2013) we aimed to maximize the flow of liquid, and thereby increase the heat flux. The necessary condition that is satisfied inside a heat pipe is the mass flow rate equation. This is because the heat pipe is a self-sufficient device, and no external pumping is required.

The operation and functioning of heat pipes, as well as previous studies, are discussed in the introductory section. Chapter 2 presents the model for the adiabatic section of wickless heat pipes in planar geometry, heat pipes with a wick in planar geometry which deals with few additional variables due to the presence of wick, thermosyphons which are again wickless heat pipes but in cylindrical geometry, and capillary driven heat pipes, which are wick based heat pipes again in cylindrical geometry. In our model, we have considered the antiparallel flow of liquid and

vapor. We have maintained an equal and opposite mass flow rate in liquid and vapor at steady-state conditions.

Section 2 of chapter 2 presents the model and the results for the planar geometry devoid of a wick. The velocity profiles are obtained by solving the governing equations with the help of boundary conditions. We have presented the expressions for the velocity profiles in terms of the fill ratio, viscosity ratio, and density ratio. Moreover, Figure 3 in Chapter 2 shows that the velocity of the vapor is larger than the velocity of the liquid. The large vapor velocity can be explained by the fact that the density of the vapor is a few orders of magnitude smaller than the density of the liquid, and to maintain equal and opposite mass flow rate conditions, the velocity of the vapor layer increases. In the case of a wickless heat pipe, the velocity profiles depend on viscosity ratios and density ratios. We have also presented velocity profiles representing the family of various viscosity ratios and density ratios in Figure 3 a. As the viscosity ratio increases, the liquid is dragged by the vapor and the velocity of liquid decreases to maintain mass flow rate condition. Similarly, as shown in Figure 3 b, as the density ratio increases, the velocity of liquid increases as well.

Section 3 of chapter 2 presents the results for the planar geometry of the adiabatic section of the heat pipe containing a wick. The presence of a wick supports the flow of liquid. Considering a wick or superhydrophobic surface were avoided by McHale et al. (2011) and Busse et al. (2013), as they considered a perfect plastron layer without referring to a superhydrophobic surface. A wick structure refers to the porous medium; therefore, we used the Brinkman equation for the flow of fluid inside the porous medium. We used the Brinkman equation rather than the Darcy equation because the Brinkman equation describes the dissipation of kinetic energy by viscous shear, like the Navier-Stokes equations, and is an extension of Darcy′s law. The Brinkman equation is well-suited for modeling fast flow in porous media. The Brinkman equation models the transitions between slow flow in porous media governed by Darcy′s law and fast flow in channels described by the Navier-Stokes equations. The Brinkman equation computes both velocity and pressure, but we are specifying pressure. The presence of a wick gave rise to two more boundary conditions due to the porous and free medium interface and the liquid-vapor interface inside the porous medium. The presence of a wick structure allowed us to represent the velocity profile for different porosities, viscosity ratios, and density ratios. We saw similar behavior in the velocity profiles for different viscosity ratios and different density ratios. In the heat pipe with a wick, we saw an inflection point in the vapor layer present inside the porous medium. Figure 6 b shows the velocity profiles with different porosity, and suggests that with an increase in porosity, the liquid layer's velocity increases as there is more room for the liquid to flow.

Section 3 of chapter 2 models a wickless heat pipe in cylindrical geometry. Conventional heat pipes usually have cylindrical shapes; therefore, we have presented the model for a thermosyphon, which is a gravity-assisted heat pipe. We have derived the expressions for velocity profiles. The

velocity profiles show similar behaviors as those in Section 2, and therefore we have not presented the figures. We have derived an expression for the pressure gradient ratio required to drive the flow in the adiabatic section. Section 4 of chapter 2 shows a capillary-driven heat pipe, the modeling of a heat pipe in a cylindrical geometry. The presence of the wick structure introduces a porous medium; therefore, our governing equation is the Brinkman equation in cylindrical coordinates. The solution to the Brinkman equation in cylindrical coordinates is in the form of Bessel's equation of the first kind. The velocity profiles show a similar trend as we saw in the planar geometry.

In the case of wickless heat pipes, we presented the parameters required to increase the mass flow rate inside a heat pipe. We provided the optimum liquid fill ratio to obtain the highest mass flow rate. In the case of a heat pipe with a wick, the liquid fill ratio, density ratio, and the viscosity ratio influence the maximum mass flow rate. To this end, we cannot increase the liquid fill ratio too agressively as it will choke the vapor core. Therefore, we need an optimum fill ratio. Figures 4 a and 16 a show the maximum mass flow rate and the optimum liquid fill ratio with various density ratios. As the density ratio increases, the optimum liquid fill ratio increases. The rise in the density ratio decreases the density of the liquid, and to maintain the equal and opposite mass flow rate, the thickness of the liquid layer increases.

Likewise, we have presented the maximum mass flow rates for wick-based heat pipes. In the wick-based heat pipe, the liquid-vapor interface is inside the porous medium. For a fixed density ratio and viscosity ratio, the maximum mass flow rates were non-monotone functions of the liquid fill ratio, as shown in figures 7 a, 8 a and 9 a of chapter 2. One main difference between the wickless heat pipe and the wick-based heat pipe is that maximized mass flow rates occur for a broad range of liquid layer thicknesses. This is because of the presence of porous medium which restricts the liquid flow and the liquid layer thickness increases. After the liquid layer has attained a threshold value the mass flow rate decreases drastically as more increase in liquid layer thickness increases the drag in the liquid and vapor. Wick-based heat pipes give us room to characterize the maximum mass flow rate in terms of wick geometry characteristics. Figure 7 b shows that with an increase in density ratio, the optimum liquid layer thickness increases. Figure 8 b shows that with an increase in the porous layer thickness, the optimum fill ratio increases, but is a non-monotone curve. When the porous medium increases, Δ/H increases, more and more of the vapor must flow through a porous medium. As a result the maximum mass flow rate is eventually associated with smaller $\left(\frac{\delta}{H}\right)_{\text{opt}}$. We have also shown the optimum liquid layer thickness for different porosities. Figure 9 b shows the optimum fill ratio with different porosities which is a non-monotone curve. The non-monotone behavior in figure 9 b occurs because the vapor layer present inside the porous medium gets enough room to flow. When $\varepsilon \to 1$, the liquid has enough room to flow just like the vapor, and therefore more space is available for the liquid to flow, and the maximum mass flow rate is achieved for a smaller liquid fill ratio.

For heat pipes devoid of a wick, the condition of equal and opposite mass flow rate allowed us to relate the pressure gradient ratio of vapor and liquid with the liquid fill ratio, density ratios, and viscosity ratios. We have presented the results showing the behavior of the pressure gradient ratio required to drive the flow of fluid inside a heat pipe. Figures 2 and 15 show the pressure gradient ratio plotted against the fill ratio and the viscosity ratio. We have provided expressions for the pressure gradient ratios and the plots showing the pressure gradient ratio with the liquid fill ratio and viscosity ratio. It can be seen in Figures 2 and 15 of chapter 2 that with an increase in the viscosity ratio, the magnitude of the pressure gradient ratio increases. Because as, the liquid becomes less viscous, we require a lower pressure gradient in the liquid phase to maintain the mass flow rate. Similarly, with an increase in the liquid fill ratio, the magnitude of the pressure gradient ratio decreases because the increase in the liquid fill ratio reduces the vapor area, and requires a higher pressure gradient inside the vapor to maintain the mass flow rate.

In the case of wick-based heat pipes, the pressure gradient ratio depends on the wick properties like porosity, permeability and also the thickness of the wick. In a wick-based heat pipe, the pressure gradients required to drive the flow are accommodated by capillarity. The pressure gradient ratio is characterized by the surface chemistry effects and the surface tension of the fluid. Section 2 c in chapter 2 shows the analysis of the pressure gradient ratio using the mass flow rate equation. Finally, we performed an analysis to find the minimum pressure gradient ratio required to support the capillary pumping of liquid from the condenser to the evaporator (e.g. equations (43) and (44)). The analysis in question employs the Young-Laplace equation at the scale of the wick microstructure, which takes into account the diameter of the wires and the spacing between the wires that comprise the (screen-type) wick. Equations (43) and (44), which define the limiting pressure gradient ratio as a function of the contact angle and the surface tension, are therefore applicable to both planar and cylindrical geometries. In either case, we found that increasing the surface tension or contact angle facilitates capillary pumping and thereby broadens the range of admissible viscosity ratios and liquid layer thicknesses (e.g. Figures 13 and 22). The analysis to evaluate the limit considers the surface chemistry effects. We have presented our results for a contact angle of 0°. Unlike the wickless heat pipes, the pressure gradient ratios obtained from the mass flow rate equation have a limit. Figures 12 and 21 show the surface plot for the pressure gradient ratio. The planar plot gives the limit for the pressure gradient ratio. The values of liquid fill ratio and viscosity ratios appearing below the planar plot are the feasible solutions and will drive the flow inside a heat pipe. We have also presented the expression for the ratio of pressure gradients and the limit to the pressure gradient ratio which, depends upon the surface chemistry effects and surface tension. In addition, we have shown the figures for the pressure gradient ratio corresponding to the optimum liquid layer analysis. Larger values of the contact angles accommodate the meniscus between the wires; therefore, an increase in contact angle broadens the solution space. The increase in surface

tension also increases the solution space because a capillary driven heat pipe is a surface tension driven flows.

The results obtained from our model are compared to an experimental investigation by Shafahi et al. (2008). The values for temperature, porosity, permeability, density, and viscosity used in chapter 2 were obtained from Shafahi et al. (2008). The pressure gradient ratio of vapor to liquid obtained in chapter 2 is verified from the ratio of pressure gradient of vapor to liquid obtained for the zero concentration of nano-particles in Shafahi et al. (2008).

There is, however, one discrepancy associated with our model: the liquid-vapor interface is assumed to be flat in-so-far as considering a shear-stress boundary condition and curved insofar as considering a capillary driven heat pipe. The discrepancy increases when the interface deflection increases. The discrepancy opened room for us to perform another analysis that shows the extent of the inconsistency and whether it is accurate to assume a flat liquid-vapor interface.

Chapter 3 analyses a deflected interface inside a porous medium. The discrepancy of using a flat interface versus a deflected interface has been explored in follow-up work to chapter 2. Chapter 3 uses the perturbation theory to model the fluid flow inside a porous medium with a deflected interface.

In chapter 3, we considered an infinite porous medium with a finite liquid layer and an infinite vapor layer, whereas chapter 2 considered a finite vapor layer. The analysis in chapter 3 maintains an equal and opposite pressure gradient in liquid and vapor. We could not maintain an equal and opposite mass flow rate in chapter 3 because the vapor layer extends infinitely. The analysis in chapter 3 uses square wires instead of circular wires. The horizontal and vertical position of the triple point changes with circular wires, whereas with square wires only the vertical position of the triple point changes. All the assumptions considered in chapter 3 are made with a view to simplifying the perturbation problem.

The analysis in question employs the Young-Laplace equation at the scale of the wick microstructure and therefore considers the diameter of, and spacing between, the wires that comprise the (screen-type) wick. We have presented the expression for the interface curvature depending on the horizontal position and a small number. The small number Φ is defined as the the ratio of the interface deflection to the thickness of the lower layer. Our interface is a circular function with the radius of curvature given by the Young-Laplace equation $\sigma/\Delta P$. The condition for a stable meniscus is different in chapter 3 as compared to chapter 2. chapter 2 considered surface chemistry effects, while in chapter 3, the presence of square wires eliminated any reference to the contact angle. Section 1 of chapter 3 mentions the condition for the meniscus stability in the case of a square wire. The interface deflection increases with the increase in pressure difference and decreases with an increase in surface tension. We have taken the values of all the variables from chapter 2, except for the liquid layer thickness which is 0.0006m, because the liquid layer thickness

of 0.0007m leads to some mathematical complications in the solution of the perturbation problem using Fourier transformation. Using the above parameters, we get an interface deflection of 5%. Figure 2 of chapter 3 represents the interface deflection. After increasing the pressure difference to a limit for a given set of values to the parameters, the meniscus is no longer in touch with the wires on the sides and it shifts upwards. Similarly, if we decrease the surface tension value to a certain limit the meniscus no longer touches the wires on both sides and it shifts upwards. Chapter 3 shows the pressure gradient value when the meniscus is no longer in touch with the square wires.

Section 3 of chapter 3 shows the governing equations for flow in a porous medium for liquid and vapor. The governing equation is the Brinkman equation, maintaining an equal and opposite pressure gradient for liquid and vapor. The governing equation is assumed to have a perturbation-based solution. We have considered only the first-order terms of the small parameter introduced for perturbation, ignoring all the higher-order terms of the small parameter. As usual, we satisfied a no-slip boundary condition at the lower wall and a far-field boundary condition for vapor. The shear-stress and matching boundary conditions are satisfied at the curved interface shown in Section 2, rather than at the liquid layer thickness, which is at the flat interface.

The governing equations are solved along with the boundary conditions by equating the small parameter's zeroth-order terms. Referencing to chapter 2, our interest lies at the liquid-vapor interface inside the porous medium. The interface boundary conditions are linearized using Taylor's series and truncating the higher-order terms of the small parameter, and we get the solution as if the interface boundary conditions were satisfied at the flat interface. The zeroth-order terms of the small parameter in the boundary conditions, along with the governing equations, are straightforward and share some similarities with the original problem shown in chapter 2. We have shown the velocity plots for the base solution.

To complete the solution for the perturbation problem, we need to evaluate the first-order solutions, which are given by equating the first-order terms of the small parameter from the governing equation and boundary conditions. The first order governing equations are given by the solution of the Helmholtz equation. The linearization of the interface boundary conditions shows that the first-order solutions depend on the horizontal position between the wires and the vertical position. We have presented the expressions for the constants appearing after solving the Helmholtz equation in terms of the known parameters and the base solution. We have demonstrated velocity profiles for the composite solution at different horizontal positions.

The base solution overlaps the composite solution in the x position where the interface curvature is equal to the flat interface. The equation of the horizontal coordinate x is presented in chapter 3, which depends upon the pressure difference, surface tension, and maximum deviation of the interface from the flat interface. We have shown the velocity profiles for the composite solution for different x and the base solution which is close the composite solution for the particular x position

where the interface curvature cuts the unperturbed interface. The velocity profiles at different x positions have some discontinuity at the interface. The discontinuity at different x positions increases as the interface deflection increases. From $x = 0$ to $x = L$, the discontinuity decreases until the position where the interface deflection becomes equal to the flat interface and then increases again until $x = L$.

Finally, we have characterized the velocity difference between the base solution and the composite solution. We performed the analysis of measuring the difference between the base solution and the composite solution to determine the effect of using the curved interface. The difference between the velocities is calculated at the interface and has been plotted for different interface deflections that can be accommodated in the adiabatic section and the pressure difference required has been adopted from Shafahi et al. (2010). Figure 6 in chapter 3 shows the interface deflection versus the velocity difference for various liquid layer thicknesses. The velocity difference is higher for the larger thickness of the liquid layer and gives a minimal interface deflection, whereas for the smaller liquid layer thickness, we get a small velocity difference for higher interface deflection.

The discontinuity at the interface occurs because of the way we have linearized our boundary conditions at the interface by ignoring all the higher-order terms of the small parameters. The inclusion of the higher-order terms of the small parameters at the interface will make our problem closer to the base solution.

One thing of note is that the velocity difference in Figure 6 is only shown at the interface. Having regard to Figure 5 of chapter 3, the discontinuity of the velocity can be seen at the interface. Therefore, the velocity difference is more significant at the interface. However, if we measure the velocity difference at different vertical positions there is no discontinuity. There is a negligible velocity difference between the base solution and the composite solution. To prove this statement, we have shown the surface plot in Figure 7 of chapter 3, which shows the velocity difference with different interface deflections at different vertical positions. Figure 7 suggests that there is a negligible velocity difference at all vertical positions, but that it increases when the vertical position approaches the interface. Similarly, Figure 8 shows a two-dimensional plot showing the velocity difference at different vertical positions. It can be concluded from the results obtained in chapter 3 that the results from chapter 2 have some value, when considering a flat interface rather than a curved interface.

The applicability of the perturbation problem to a finite vapor layer poses further complications. We use the Helmholtz equation for our first order governing equation, the solution of which involves summation for all positive integers. The presence of two-phase gives two governing equations of second order and is 2-dimensional. There are six constants involved, and to reduce complexity, an infinite domain imposes a far-field boundary condition, which reduces the constants involved. The presence of a finite vapor layer will save the constant. Another complication is using

a finite porous medium with the rest of the vapor in the free medium. The velocity of vapor in the free medium will be given by the Navier-Stokes equation. The perturbation problem can be applied to the heat pipe model presented in chapter 2, which will avoid the discrepancy of using a flat interface for the shear-stress boundary condition and a curved interface for the capillary pressure.

The problem considered in chapter 3 can be improved further by using circular wires instead of square wires to find an interface curvature that considers the surface chemistry effects. Also, to discover an expression for the curved interface, we will use the volume conservation of the liquid layer by excluding the extra volume of the wires that arises due to the change in the horizontal position of the triple point. Finally, we can use the same analysis of using perturbation theory by ignoring all the higher-order terms for a finite vapor layer, as we saw in chapter 2.

Some improvements that we can incorporate into our model are to assume a non-linear pressure variation in liquid and vapor phase along the adiabatic section rather than a linear pressure variation. Our original model also assumed c_μ and c_ρ as constant, but c_μ and c_ρ can vary with the temperature, and temperature varies along the length of the heat pipe.

As future work, a real heat pipe involves a condenser section and evaporator section. We can extend our study to understand the phase changes in these sections. For instance, we can consider drop-wise condensation and film-wise evaporation which increases the performance of the heat pipe. Including such details do not change the results obtained above for the adiabatic section. We can use an expanded CAF type model for a real heat pipe where two-phase internal flows occur in the adiabatic section, and phase changes take place in the evaporator and the condenser section. Our model has shown the flow inside the adiabatic section and we can decide our liquid fill ratio to achieve maximum heat flux. We can extend this analysis to see whether the obtained optimum fill ratio is sufficient so that the evaporator dry out limit is not reached.

References

[1] G Ooms, C Vuik, and P Poesio. Core-annular flow through a horizontal pipe: hydrodynamic counterbalancing of buoyancy force on core. *Phys. Fluids*, 19(9):092103, 2007.

[2] John Dove Isaac and James Buckner Speed. Method of piping fluids., May 10 1904. US Patent 759,374.

[3] Ronaldo Gonçalves dos Santos, Maria Isabel Brinceño, and Watson Loh. Laminar pipeline flow of heavy oil–in–water emulsions produced by continuous in-line emulsification. *Journal of Petroleum Science and Engineering*, 156:827–834, 2017.

[4] DD Joseph, R Bai, TY Liao, A Huang, and HH Hu. Parallel pipelining. 1995.

[5] DD Joseph, R Bai, KP Chen, and YY Renardy. Core-annular flows. *Annu. Rev. Fluid Mech.*, 29(1):65–90, 1997.

[6] B Gruncell, ND Sandham, and G McHale. Simulations of laminar flow past a superhydrophobic sphere with drag reduction and separation delay. *Phys. Fluids*, 25(4):043601, 2013.

[7] R Sean Sanders, Taehwan Ko, Runyuan Bai, and Daniel D Joseph. S yncrude canada ltd. produces approximately 250,000 barrels of. *The Canadian Journal of Chemical Engineering*, 82, 2004.

[8] A Busse, ND Sandham, G McHale, and MI Newton. Change in drag, apparent slip and optimum air layer thickness for laminar flow over an idealised superhydrophobic surface. *J. Fluid Mech.*, 727:488–508, 2013.

[9] G McHale, MR Flynn, and MI Newton. Plastron induced drag reduction and increased slip on a superhydrophobic sphere. *Soft Matt.*, 7(21):10100–10107, 2011.

[10] D Panchanathan, A Rajappan, KK Varanasi, and GH McKinley. Plastron regeneration on submerged superhydrophobic surfaces using in situ gas generation by chemical reaction. *ACS Appl. Mater. Inter.*, 10(39):33684–33692, 2018.

[11] Pontus Forsberg, Fredrik Nikolajeff, and Mikael Karlsson. Cassie–wenzel and wenzel–cassie transitions on immersed superhydrophobic surfaces under hydrostatic pressure. *Soft Matter*, 7(1):104–109, 2011.

[12] Hangjian Ling, Siddarth Srinivasan, Kevin Golovin, Gareth H McKinley, Anish Tuteja, and Joseph Katz. High-resolution velocity measurement in the inner part of turbulent boundary layers over super-hydrophobic surfaces. *Journal of Fluid Mechanics*, 801:670–703, 2016.

[13] Richard S Gaugler. Heat transfer device, June 6 1944. US Patent 2,350,348.

[14] Flavio Dobran. Heat pipe research and development in the americas. *Heat Recovery Systems and CHP*, 9(1):67–100, 1989.

[15] Bin-Juine Huang, Yi-Hung Chuang, and Po-En Yang. Low-cost manufacturing of loop heat pipe for commercial applications. *Applied Thermal Engineering*, 126:1091–1097, 2017.

[16] Thang Nguyen, M Mochizuki, K Mashiko, Y Saito, and I Sauciuc. Use of heat pipe/heat sink for thermal management of high performance cpus. In *Sixteenth Annual IEEE Semiconductor Thermal Measurement and Management Symposium (Cat. No. 00CH37068)*, pages 76–79. IEEE, 2000.

[17] Edna A Dancy and James H Vansant. Fabrication of ceramic heat pipes, April 4 1978. US Patent 4,082,863.

[18] Carl J Fries Jr. Induction heat sealing lap-seamed containers to non-metallic closures, May 7 1991. US Patent 5,013,878.

[19] James C Corman and Gunnar E Walmet. Heat transfer device, November 15 1977. US Patent 4,058,160.

[20] W Kinzy Jones, Yanqing Liu, and Mingcong Gao. Micro heat pipes in low temperature cofire ceramic (ltcc) substrates. *IEEE Transactions on components and packaging technologies*, 26(1):110–115, 2003.

[21] Mohamed Elnaggar. The effect of thickness and permeability of wick structure on l-shape heat pipe performance using different working fluids. *Frontiers in Heat Pipes (FHP)*, 3(4), 2013.

[22] PM Hui, X Zhang, AJ Markworth, and D Stroud. Thermal conductivity of graded composites: Numerical simulations and an effective medium approximation. *Journal of materials science*, 34(22):5497–5503, 1999.

[23] F Ochs, Wolfgang Heidemann, and Hans Müller-Steinhagen. Effective thermal conductivity of moistened insulation materials as a function of temperature. *International Journal of Heat and Mass Transfer*, 51(3-4):539–552, 2008.

[24] G McHale, MI Newton, and NJ Shirtcliffe. Immersed superhydrophobic surfaces: Gas exchange, slip and drag reduction properties. *Soft Matt.*, 6(4):714–719, 2010.

[25] Sjoerd Rienstra. Fundamentals and applications of perturbation methods in fluid dynamics.

[26] DG Crighton. Asymptotics–an indispensable complement to thought, computation and experiment in applied mathematical modelling. In *Proceedings of the Seventh European Conference on Mathematics in Industry, March 2-6, 1993, Montecatini*, pages 3–19, 1994.

[27] KN Shukla et al. Heat pipe for aerospace applications—an overview. *Journal of Electronics Cooling and Thermal Control*, 5(01):1, 2015.

[28] VG PastUkhov, YF Maidanik, CV Vershinin, and MA Korukov. Miniature loop heat pipes for electronics cooling. *Appl. Therm. Eng.*, 23(9):1125–1135, 2003.

[29] VE Hampel. Underground nuclear power station using self-regulating heat-pipe controlled reactors, 1989. US Patent 4,851,183.

[30] G Gan and SB Riffat. A numerical study of solar chimney for natural ventilation of buildings with heat recovery. *Appl. Therm. Eng.*, 18(12):1171–1187, 1998.

[31] J Qu, H Wu, and P Cheng. Effects of functional surface on performance of a micro heat pipe. *Int. Commun. Heat Mass*, 35(5):523–528, 2008.

[32] N Zhu and K Vafai. Vapor and liquid flow in an asymmetrical flat plate heat pipe: a three-dimensional analytical and numerical investigation. *International Journal of Heat and Mass Transfer*, 41(1):159–174, 1998.

[33] D Reay, R McGlen, and P Kew. *Heat pipes: theory, design and applications*. Butterworth-Heinemann, 2013.

[34] Z Bahman. Heat pipe design and technology, a practical approach, 2011.

[35] GP Peterson. Heat pipes–modeling, testing, and applications. *John Willey & Sons, Incorporation, United States of America*, 1994.

[36] A Faghri. Review and advances in heat pipe science and technology. *J. Heat Transf.*, 134(12):123001, 2012.

[37] JE Kemme. High-performance heat pipes. Technical report, Los Alamos Scientific Lab., N. Mex., 1968.

[38] L Durlofsky and JF Brady. Analysis of the brinkman equation as a model for flow in porous media. *Phys. Fluids*, 30(11):3329–3341, 1987.

[39] JC Slattery. Two-phase flow through porous media. *AIChE Journal*, 16(3):345–352, 1970.

[40] JA Ochoa-Tapia and S Whitaker. Momentum transfer at the boundary between a porous medium and a homogeneous fluid—i. theoretical development. *Int. J. Heat Mass Tran.*, 38(14):2635–2646, 1995.

[41] M Shafahi, V Bianco, K Vafai, and O Manca. An investigation of the thermal performance of cylindrical heat pipes using nanofluids. *Int. J. Heat Mass Tran.*, 53(1-3):376–383, 2010.

[42] D Khrustalev and A Faghri. Thermal analysis of a micro heat pipe. *J. Heat Transf.*, 116(1):189–198, 1994.

[43] J Zhang, SJ Watson, and H Wong. Fluid flow and heat transfer in a dual-wet micro heat pipe. *J. Fluid Mech.*, 589:1–31, 2007.

[44] Morris R Flynn and John WM Bush. Underwater breathing: the mechanics of plastron respiration. *Journal of Fluid Mechanics*, 608:275–296, 2008.

[45] GP Peterson. An introduction to heat pipes. modeling, testing, and applications. *Wiley Series in Thermal Management of Microelectronic and Electronic Systems, New York, Chichester: Wiley,| c1994*, 1994.

[46] N Zhu and K Vafai. Analysis of cylindrical heat pipes incorporating the effects of liquid–vapor coupling and non-darcian transport—a closed form solution. *International Journal of Heat and Mass Transfer*, 42(18):3405–3418, 1999.

[47] Kambiz Vafai and Chang L Tien. Boundary and inertia effects on flow and heat transfer in porous media. *International Journal of Heat and Mass Transfer*, 24(2):195–203, 1981.

[48] Susan Daniel, Manoj K Chaudhury, and John C Chen. Fast drop movements resulting from the phase change on a gradient surface. *Science*, 291(5504):633–636, 2001.

[49] Lixin Cheng and Dieter Mewes. *Advances in multiphase flow and heat transfer*, volume 3. Bentham Science Publishers, 2012.

[50] Oleg A Alduchov and Robert E Eskridge. Improved magnus form approximation of saturation vapor pressure. *Journal of applied meteorology*, 35(4):601–609, 1996.

[51] D Andrew Rees and Peder A Tyvand. The helmholtz equation for convection in two-dimensional porous cavities with conducting boundaries. *Journal of engineering mathematics*, 49(2):181–193, 2004.